Analysis of thermoplastic composites and conduction welded joints

Tijs, B.H.A.H.

DOI

10.4233/uuid:dd3bff55-b684-47cc-96f3-6ff109d345a0

Important note
To cite this publication, please use the final published version (if applicable).
Please check the document version above.

Analysis of Thermoplastic Composites and Conduction Welded Joints

Bas H.A.H. Tijs
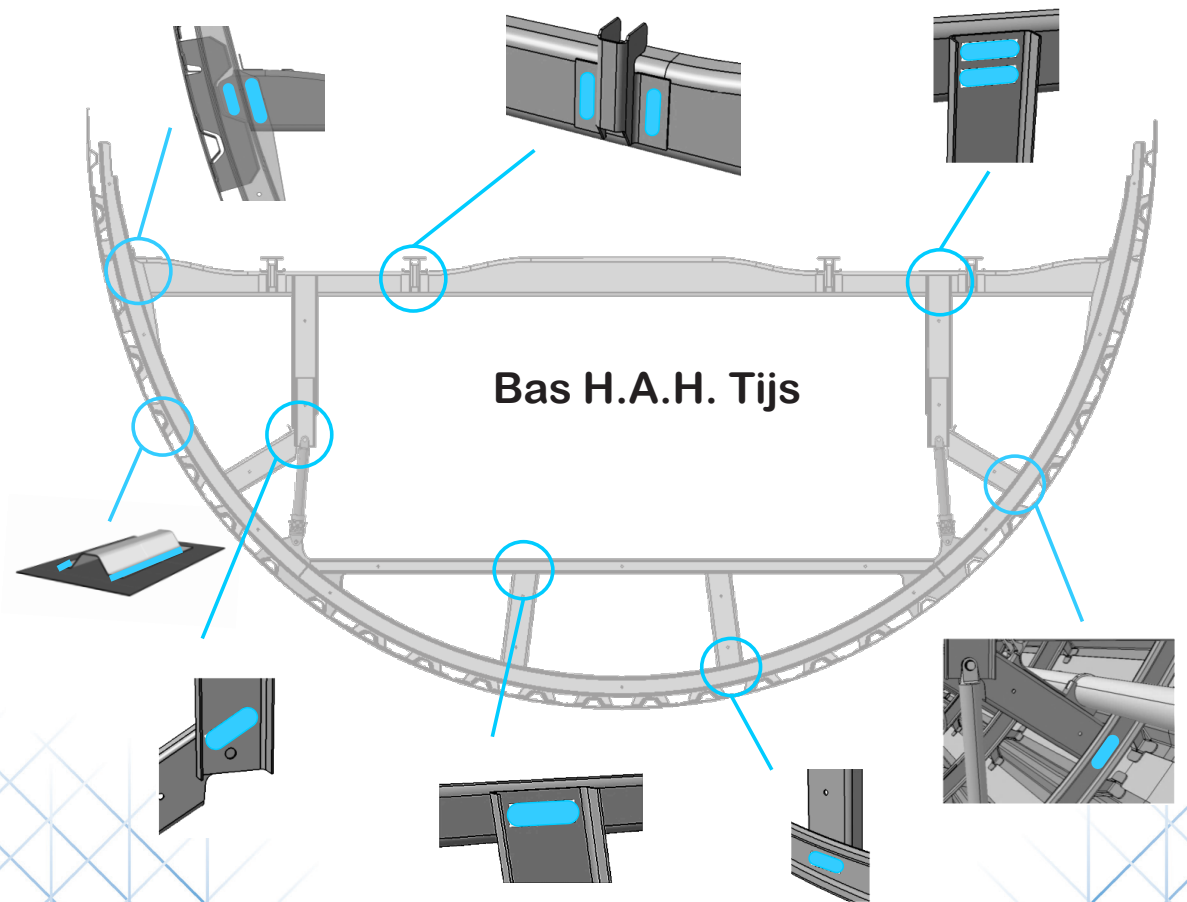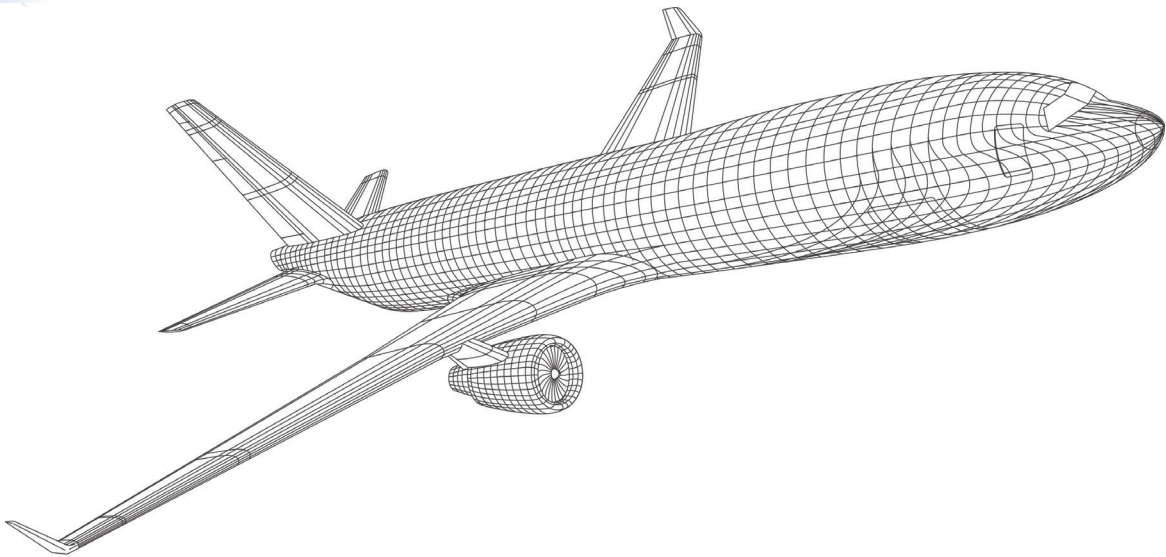
Analysis of Thermoplastic Composites and Conduction Welded Joints

Analysis of Thermoplastic Composites and Conduction Welded Joints

Dissertation

for the purpose of obtaining the degree of doctor
at Delft University of Technology
by the authority of the Rector Magnificus prof. dr. ir. T.H.J.J. van der Hagen
chair of the Board for Doctorates
to be defended publicly on
Monday 15 May 2023 at 12:30 o'clock

by

Bas Henricus Antonius Hermanus TIJS

Bachelor of Engineering in Aeronautical Engineering, the Netherlands
born in Zwolle, the Netherlands.

This dissertation has been approved by the promotors.

Composition of the doctoral committee:

Rector Magnificus,	chairperson
Prof. dr. C. Bisagni,	Delft Universtiy of Technology, promotor
Dr. A. Turon Travesa,	Universitat de Girona, Spain, promotor

Independent members:

Prof. dr. M.R. Wisnom,	University of Bristol
Prof. dr. R. Butler,	University of Bath
Prof. C.A. Dransfeld,	Delft University of Technology
Dr. ir. W.J.B. Grouve,	University of Twente
Dr. C.G. Dávila,	NASA Langley Research Center
Prof. dr. ir. R. Benedictus,	Delft University of Technology, reserve member

Contents

Summary

Thermoplastic composites enable new manufacturing techniques such as conduction welding to make the aviation industry more sustainable, while at the same time, provide great benefits to cost-efficient high-volume production. One of the benefits of welding is that it reduces the amount of mechanical fasteners required. Fastener-free joining also poses new challenges, because the performance of these highly loaded structural joints relies heavily on the performance of the thermoplastic polymer matrix. Furthermore, there is currently not much understanding of the mechanisms involved in thermoplastic welded joint failure, and the numerical and experimental methodologies, originally developed and validated on thermoset composites, have not yet been fully assessed for thermoplastic composites. On top of that, the process conditions to manufacture these new structures may have a significant influence on the mechanical performance of the material and can thus play an important role in the design of thermoplastic composite structures.

The objective of this research is to analyse matrix dominated failure of thermoplastic composites and conduction welded joints and to develop both experimental and numerical methodologies to support the design of thermoplastic composites structures. The research addresses important linkages between the three main pillars of *Manufacturing*, *Experimental* and *Numerical* analysis.

First, the ability of continuum damage models to accurately predict matrix failure and ply splitting is investigated, as these failure modes are considered important for welded joints. Two methodologies are implemented in a new continuum damage model based on different stress-strain measures. The first approach is based on small-strain increments, while the second approach account for large deformation kinematics. The methodology is evaluated by numerical benchmarks at three different levels: (1) single element; (2) unidirectional single ply open-hole specimen and (3) open-hole composite laminate coupon. It is demonstrated that the methodology to account for large deformation kinematics in the constitutive model is of high importance, especially when predicting matrix splitting failure modes. The methodology improves the general Virtual Testing capabilities for both thermoset and thermoplastic composites and provides the baseline for the high-fidelity analyses on the welded joints.

The new manufacturing processes and fastener-free assembly techniques employed for thermoplastic composites make the performance of the structure more reliant on the interlaminar behavior, while limited experimental data is available. Therefore, the interlaminar properties of autoclave consolidated AS4D/PEKK-FC thermoplastic composite are characterized and analyzed by means of Mode I, II and Mixed Mode I/II at 50:50 tests, while considering fiber bridging and R-curve effects. The test configurations are adjusted to account for the large fracture process zone ahead of the crack tip in order to achieve stable crack propagation and an appropriate data reduction method is selected. The experimental data is reduced using an inverse methodology combined with a new procedure to define the cohesive laws in tabular format directly into commercial finite element software based on

only the load-displacement curves. The shape of the cohesive laws provided new insights into the influence of fiber bridging interlaminar behavior and fractographic analysis of the interlaminar damage mechanisms confirmed a strong influence of fiber bridging combined with significant plastic deformation on the fracture surface.

After autoclave consolidation, the laminates are ready for conduction welding. With the availability of the mixed-mode interlaminar properties and the continuum damage model, the strength and failure behavior of the welded joints can be studied both numerically and experimentally. Therefore, a conduction welded single lap shear joint is designed, manufactured and tested. Two distinct modelling approaches are proposed for the analysis. First, a simplified model which only accounts for damage at the welded interface. Secondly, a high-fidelity ply-by-ply approach which accounts for the physical failure mechanisms at the lamina level. The high-fidelity modelling methodology is able to predict the experimental failure mode of the investigated welded joints with high accuracy demonstrating that the joint strength is highly influenced by the failure mechanisms not only of the welded interface but also of the surrounding plies. However, the autoclave interlaminar properties were not sufficient to predict the strength of the joints, and it was predicted that the most likely source of this mismatch is the change in the local material properties due to the welding process.

In order to address this, a methodology is developed to characterize and analyse thermoplastic composite conduction welded joints, while accounting for the influence of the manufacturing process. Test specimens are designed from welds of a half a meter long welding tool. Special attention is paid to the weldability of the laminates, as typical unidirectional characterization specimens are difficult to weld. Furthermore, a 0-degree interface is used to ensures that fracture only occurs at the welded interface. Characterization tests are performed by means of Double Cantilever Beam and End-Notched Flexure tests on two different specimen configurations using different welding recipes. The full weld width specimens provided insight in the manufacturing quality of the weld, however, the specimen cut from the center of the weld are the most representative to characterize the material property of the joint. The influence of the manufacturing process showed a significant influence on the Single Lap-Shear joints due to changes in weld size. This change in weld size is related to experimental results from tensile and during three-point-bending tests. Finally, the characterized material properties are used in numerical analyses to evaluate the use of the cohesive zone modeling approach to predict the strength of these welded joint.

In this research, the matrix dominated failure of thermoplastic composites and conduction welded joints have been studied in great details and several experimental and numerical methodologies were developed to support the design of thermoplastic composites structures. The methodologies provide new insights into the relation between the manufacturing process, the mechanical properties of thermoplastic composites and the quality and failure behavior of conduction welded joints.

Samenvatting

Thermoplast composieten maken nieuwe productietechnieken mogelijk, zoals conductielassen, om de luchtvaartindustrie duurzamer te maken en bieden tegelijkertijd grote voordelen voor kostenefficiënte productie in grote volumes. Een van de voordelen van lassen is dat er minder mechanische bevestigingsmiddelen nodig zijn. Verbindingen zonder bevestigingsmiddelen geven ook nieuwe uitdagingen, omdat de prestaties van deze zwaarbelaste structurele verbindingen sterk afhankelijk zijn van de prestaties van de polymeermatrix. Bovendien is momenteel de kennis met betrekking tot de faalmechanismen van thermoplastische lasverbindingen beperkt. De numerieke en experimentele methodologieën, oorspronkelijk ontwikkeld en gevalideerd op thermohardende composieten, zijn tevens nog niet volledig onderzocht voor thermoplast composieten. Bovendien kunnen de procesomstandigheden om deze nieuwe constructies te vervaardigen een aanzienlijke invloed hebben op de mechanische prestaties van het materiaal en kunnen ze dus een belangrijke rol spelen bij het ontwerp van thermoplast composietconstructies.

Het doel van dit onderzoek is het analyseren van matrixgedomineerd falen van thermoplast composieten en conductielassen en het ontwikkelen van zowel experimentele als numerieke methodologieën ter ondersteuning van het ontwerpproces van thermoplast composietconstructies. Het onderzoek richt zich op belangrijke verbanden tussen de drie belangrijkste pijlers van *Productie*, *Experimentele* en *Numerieke* analyses.

Ten eerste wordt het vermogen van continuüm-schademodellen onderzocht om matrixbezwijken en het splijten van lagen nauwkeurig te kunnen voorspellen, aangezien deze bezwijkvorm als belangrijk wordt beschouwd voor lasverbindingen. Twee aanpakken zijn geïmplementeerd in een nieuw continuüm schademodel. De eerste benadering is gebaseerd op incrementele kleine verhogingen van de rek, terwijl de tweede benadering rekening houdt met grote vervormingskinematica. De methodologie wordt geëvalueerd door numerieke benchmarks op drie verschillende niveaus: (1) enkelvoudig element; (2) unidirectionele enkele-laags proefstuk met gat en (3) composiet laminaat proefstuk met gat. Er is aangetoond dat de methodologie om rekening te houden met grote vervormingskinematica in het constitutieve model van groot belang is, vooral bij het voorspellen van faalwijzen voor matrixbezwijken en splijten. De methodologie verbetert de algemene virtuele testmogelijkheden voor zowel thermohardende als thermoplastische composieten en vormt de basis voor de gedetailleerde analyses op de gelaste verbindingen.

De nieuwe productietechnieken zonder bevestigingsmiddelen die worden gebruikt voor thermoplastische composieten, maken de prestaties van de constructie meer afhankelijk van het interlaminaire gedrag, terwijl experimentele data beperkt beschikbaar is. Daarom worden de interlaminaire eigenschappen van autoclaaf geconsolideerd AS4D/PEKK-FC thermoplast composiet gekarakteriseerd en geanalyseerd door middel van Mode I, II en Mixed Mode I/II (50:50) testen, rekening houdend met fiber-bridging en R-curve-effecten. De testconfiguraties zijn gemodificeerd om rekening te houden met de grote schadezone vóór de scheurtip om een stabiele scheurgroei te bereiken. Ook wordt er een geschikte

datareductiemethode geselecteerd. De experimentele data wordt gereduceerd met behulp van een inverse aanpak in combinatie met een nieuwe procedure om de cohesiewetten in tabelvorm rechtstreeks in commerciële eindige-elementensoftware te definiëren op basis van alleen de belasting-verplaatsingscurven. De vorm van de cohesiewetten verschafte nieuwe inzichten in de invloed van het interlaminaire gedrag en fractografische analyse van de interlaminaire schademechanismen bevestigde een sterke invloed van fiber-bridging in combinatie met significante plastische deformatie op het breukoppervlak.

Na consolidatie in de autoclaaf zijn de laminaten klaar voor conductielassen. Gebruik-makend van de mixed-mode interlaminaire eigenschappen en het continuüm-schademodel, kunnen de sterkte en het faalgedrag van de lasverbindingen zowel numeriek als experimenteel worden bestudeerd. Daarom wordt een door conductie gelaste enkelvoudige afschuifverbinding ontworpen, vervaardigd en getest. Voor de analyse worden twee verschillende modelleringsbenaderingen voorgesteld. Ten eerste een vereenvoudigd model dat alleen rekening houdt met schade aan de gelaste interface. Ten tweede een detail laag-voor-laag benadering die de fysieke faalmechanismen op lamina-niveau verklaart. De high-fidelity modelleringsmethodiek is in staat om de experimentele faalwijze van de onderzochte lasverbindingen met hoge nauwkeurigheid te voorspellen, wat aantoont dat de verbindingssterkte sterk wordt beïnvloed door de faalmechanismen, niet alleen van de gelaste interface maar ook van de omliggende lagen. De interlaminaire eigenschappen van de autoclaaf zijn echter niet voldoende om de sterkte van de verbindingen te voorspellen en er is voorspeld dat de meest waarschijnlijke oorzaak van deze mismatch de verandering in de lokale materiaaleigenschappen als gevolg van het lasproces is.

Om dit aan te pakken, is een methodologie ontwikkeld om thermoplast composiet conductie lasverbindingen te karakteriseren en te analyseren, rekening houdend met de invloed van het fabricageproces. Proefstukken zijn ontworpen uit lassen van een halve meter lang lasgereedschap. Er wordt speciale aandacht besteed aan de lasbaarheid van de laminaten, aangezien typische unidirectionele karakteriseringsproefstukken moeilijk te lassen zijn. Bovendien wordt een 0-graden vezelrichting op de las gebruikt om ervoor te zorgen dat breuk alleen optreedt in de las. Karakterisatietesten zijn uitgevoerd door middel van Double Cantilever Beam en End-Notched Flexure tests op twee verschillende proefstukconfiguraties met verschillende lasrecepten. De proefstukken met volledige lasbreedte gaven inzicht in de kwaliteit van de las, maar de proefstukken welke uit het midden van de las zijn gesneden, bleken het meest representatief om de materiaaleigenschappen van de verbinding te karakteriseren. De invloed van het fabricageproces heeft een significante invloed op de Single Lap-Shear-verbindingen als gevolg van veranderingen in de lasgrootte. Deze verandering in lasgrootte is gerelateerd aan experimentele resultaten van trek- en driepuntsbuigtesten. Ten slotte worden de gekarakteriseerde materiaaleigenschappen gebruikt in numerieke analyses om het gebruik van de cohesieve-zone-modelleringsaanpak te evalueren en de sterkte van deze lasverbindingen te voorspellen.

In dit onderzoek is het matrixgedomineerde bezwijken van thermoplast composieten en conductielasverbindingen tot in detail bestudeerd en zijn er verschillende experimentele en numerieke methodologieën ontwikkeld om het ontwerpproces van thermoplastische composietstructuren te ondersteunen. De methodieken geven nieuwe inzichten in de relatie tussen het fabricageproces, de kwaliteit, de mechanische eigenschappen van thermoplastische composieten en het faalgedrag van conductiegelaste verbindingen.

1

INTRODUCTION

As Europe plunges into handling the recent climate and energy crisis, the EU has begun to roll-out several programs with the goal to enhance sustainability, reduce fuel consumption and CO_2 emissions. This pushes the aviation sector to move towards more sustainable and affordable aircraft structures. It is therefore inevitable that changes have to be made in the way aircraft structures are designed and manufactured and one of the materials that can facilitate this transition is thermoplastic composite. Thermoplastic composites offer, among many other benefits, improved mechanical properties compared to thermoset composites, 'unlimited' shell life and also recyclability. Furthermore, new manufacturing techniques such as out-of-autoclave consolidation, co-consolidation and thermoplastic welding may greatly benefit high-volume cost-efficient manufacturing, while at the same time provide a more sustainable solution. This in combination with the recent growth in advanced modelling techniques and available computational power, may enable the aerospace industry to take full advantage of this transition to enhance sustainability and mitigate their carbon footprint.

1.1 THERMOPLASTIC FUSELAGE FOR NEXT GENERATION AIRCRAFT

As part of the EU's Clean Sky 2 initiative, the Multi-Functional Fuselage Demonstrator (MFFD) gives an impression of what the next-generation fuselage could be. With its 8.5 meter long thermoplastic composite fuselage section that is 4 meter in diameter, it is the largest known thermoplastic structure ever made in the world. This new design aims to challenges how aircraft are manufactured in order to not only improve the structure, but also greatly reduce manufacturing costs, while at the same time making the aerospace industry more sustainable. The research presented in this thesis is part of the technology development in the Clean Sky 2 STUNNING project (SmarT mUlti-fuNctioNal and INtegrated thermoplastic fuselaGe) that develops, manufactures and delivers the full scale multi-functional integrated thermoplastic fuselage shell, including cabin and cargo floor structure and main interior and system elements. Advanced multi-disciplinary design, manufacturing, and simulation methods are applied to improve cost, quality, robustness

and performance of the thermoplastic components. A significant weight reduction resulting from this integrated approach is foreseen. The consortium consists of Fokker/GKN Aerospace, Delft University of Technology, National Aerospace Laboratory NLR and Diehl. The Multi-Functional Fuselage Demonstrator which is being assembled at SAM|XL in the Netherlands is shown in Figure 1.1. There are many different manufacturing techniques
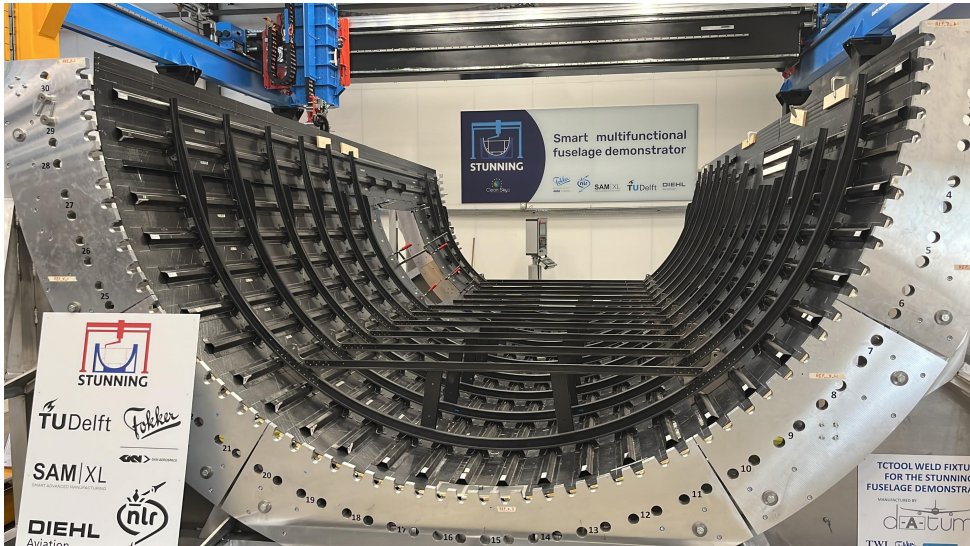
Figure 1.1: Multi-Functional Fuselage Demonstrator at SAM-XL the Netherlands.

available for thermoplastic composites structures [1], which are also considered for the STUNNING project. Two main categories of manufacturing techniques can be identified based on the area to be heated, that is to say bulk and local heating. The former group, which includes autoclave-, oven- and press-consolidation, involves applying heat to melt the entire part while maintaining pressure throughout the full process. Consequently, this manufacturing approach requires long processing times (1 to 2 hours), which can be brought down for smaller parts by applying out-of-autoclave techniques such as press-forming, press-consolidation and compression molding. The second group, generally applied as an assembly [2] or forming technique, is characterised by local heating and pressure. The consequence is that short processing times, in the order of seconds to minutes, can be achieved. The most established welding techniques [3] for continuous fibre reinforced thermoplastic composites are resistance [4], induction [5, 6] and ultrasonic welding [7]. Thermoplastic welding is applied to manufacture and assemble the MFFD to reduce both weight and costs by reducing the amount of mechanical fasteners required. On the MFFD it is aimed to weld over 2000 different locations. Examples of welded joint locations are shown in Figure 1.2 and consist of connections of the omega stiffeners to the skin, the frame-skin joints, assembly of the floor structures and attachments of the floor assembly to the frame/skin. The primary welding technology that is used is the new conduction welding technology.
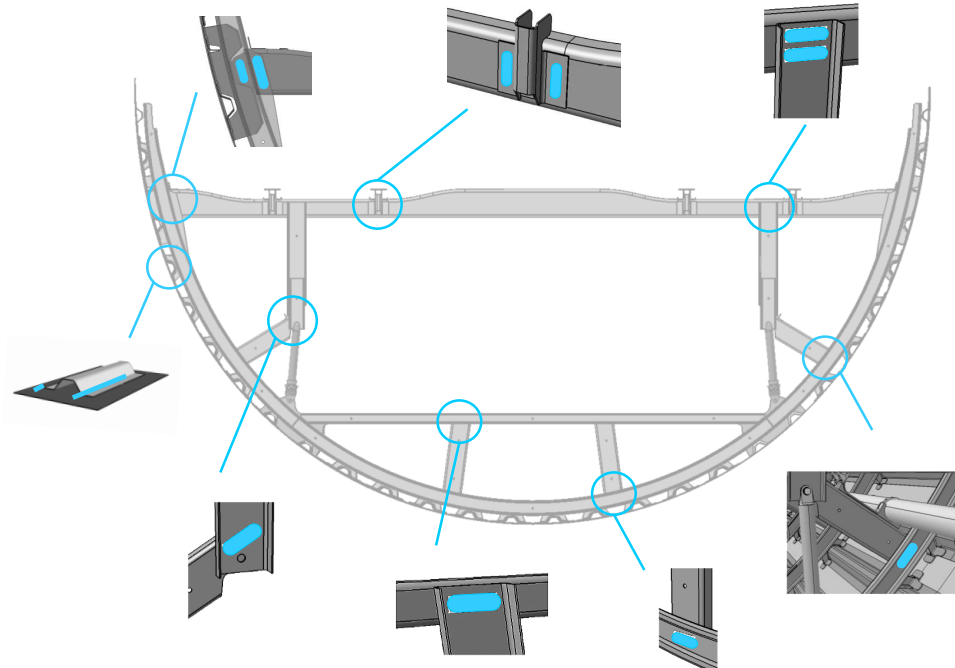
Figure 1.2: Conduction welding of the Multi-Functional Fuselage Demonstrator structure.

1.2 Conduction welding of thermoplastic composites

Conduction welding [8–10] is based on heating the surface of the thermoplastic composite part through an induction heated stamp with integrated heatsink as shown in Figure 1.3a. Pressure is applied by the tooling and is reacted by the anvil. This process generates a weld bath by means of heat conduction through the thickness and joins the two laminates at the welded interface. Conduction welding follows the same principle of applying heat and pressure as autoclave consolidation, but at a much shorter time span. The typical process cycle as shown in Figure 1.3b consists of a heat-up, consolidation and cooldown phase. The benefit of the conduction welding technique is that it does not require addition of welding specific materials such as energy directors or conductive strips. Furthermore, the technique is more suitable and scalable for welding of large parts and allows for absorbing of manufacturing tolerances like gaps and the process is independent of the length of the welding tool.

The MFFD floor assembly as shown in Figure 1.2 is welded by means of the welding setup presented in Figure 1.4. The setup consists of an (1) end-effector with the welding head, consisting of stamp and heatsink, and anvil, 2) generator to create the magnetic induction field as heating source, 3) chiller to cool the system, 4) pressure control system and 5) a robot system to position the end-effector. In this thesis, the setup presented in

1
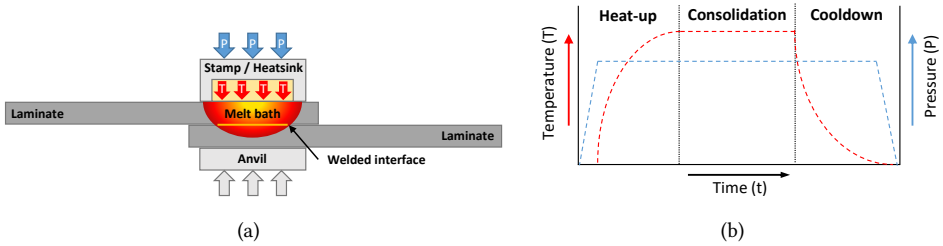
Figure 1.3: Conduction welding principle: a) Schematic; b) Typical manufacturing process cycle [11].

Figure 1.4 is used for the short welds of the single lap-shear specimens of Chapter 4 [12]. The work presented in Chapter 5 makes use of a similar setup, but by using a larger 0.5 meter welding tool [11].
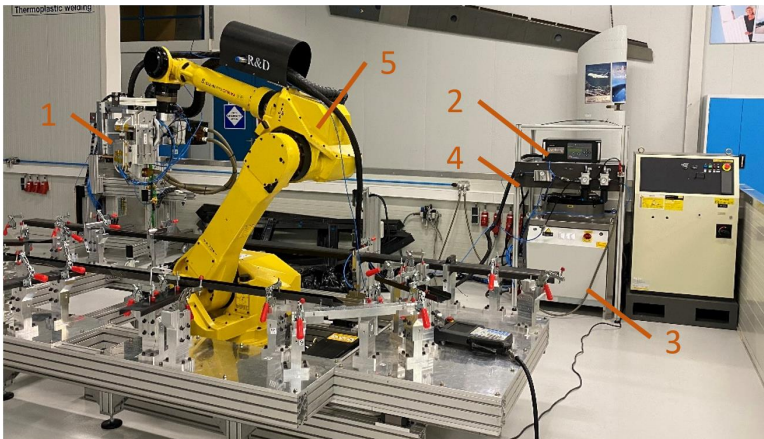
Figure 1.4: MFFD floor assembly welding setup: 1) End-effector; 2) Generator; 3) Chiller; 4) Pressure control system; 5) Robot system.

One of the main advantages of thermoplastic welding is that the amount of mechanical fasteners required are reduced. However, this also comes with new challenges as the strength of these highly loaded joints relies on the performance of the thermoplastic matrix. In comparison to autoclave consolidation, the material properties of the weld may be locally influenced by the welding manufacturing process. This makes it difficult to predict the strength of the welded joints without the availability of material data, experimental characterization techniques and advanced predictive tools. One of the advanced numerical methods to predict the strength of composites is Virtual Testing.

1

1.3 Virtual testing of composite materials

The Virtual Testing methodology applies a systematic strategy to predict the mechanical behaviour of composites up to failure using both numerical and experimental approaches in parallel [13]. This approach takes into account the physical material failure mechanisms, so the influence of each contributing failure modes on the performance of the part can be taken into account rigorously. The approach follows a bottom-up approach so that changes in material properties and failure behavior at the lower end of the testing pyramid can be easily adapted to provide new predictions at the structural level.

At the lower end of the testing pyramid as shown in Figure 1.5, numerical analyses take into account the physical failure mechanisms at the lamina level through a high-fidelity modelling approach. Higher up the testing pyramid, at the structural element, detail and (sub)component level, a more computationally efficient methods needs to be applied. At this level the emphasis is at global structural behaviour and failure of specific critical joints such as the skin-stiffener interface. This makes it important to understand both the mechanical properties and failure behavior of these joints. Therefore, use is made of a virtual building block approach to ensure the validity of the methodology at each scale [14, 15].
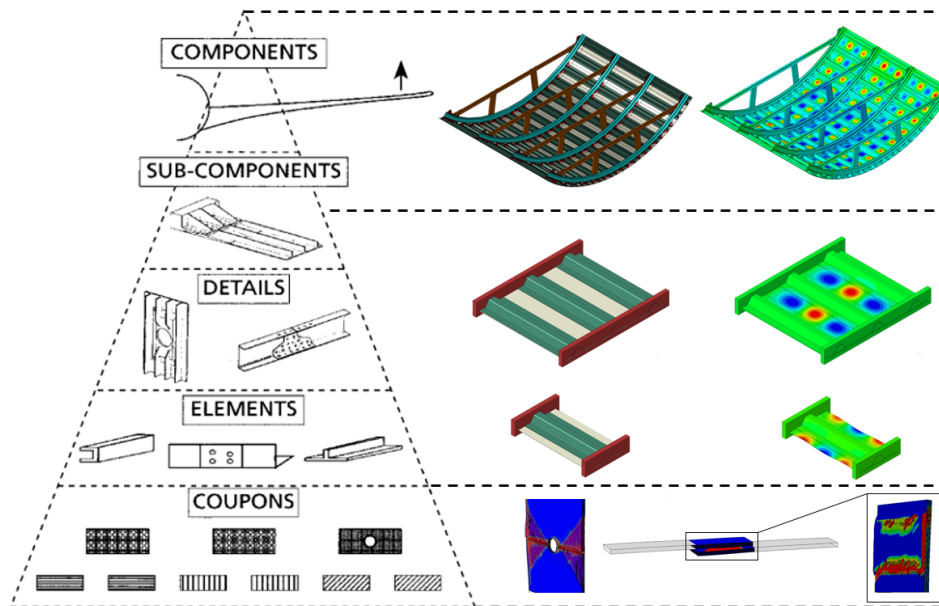
Building-block approach acc. to MIL-HDBK-17-1F (2002)

Figure 1.5: Virtual building block approach for thermoplastic composites [15].

The work in this thesis contributes to the development of both experimental and analysis methods for thermoplastic composites and conduction welded joints. Therefore, the focus of the research is on the lower levels of the testing pyramid that consists of characterization, coupon and joint testing and analyses. The new developments presented

in this thesis allow for the extension of the Virtual Testing methodology, which has been originally developed and validated on thermoset composites, for thermoplastic composites. The numerical framework that is in development [15] at Fokker/GKN Aerospace is implemented in a Virtual Coupon Testing lab [16–19] in the commercial finite element software package Abaqus and takes into account the physical mechanisms of damage at lamina level. The methodology relies on a ply-by-ply modelling approach that consists of mesh structuring, a cohesive-frictional penalty-based contact surface and advanced crack-band erosion techniques coupled with a sophisticated three-dimensional continuum damage model to accurately capture the appropriate failure modes. The approach is able to predict the progressive failure mechanisms with high accuracy with respect to the results obtained experimentally for plain, open-hole, low-velocity impact and compression-after-impact tests as shown in Figure 1.6 for thermoset composites [14]. Although many advances have been made for these numerical models, their application to thermoplastic composites and welded composite joints is rather limited. Especially predicting the matrix dominated failure modes of these welded joints may still pose a number of difficulties.
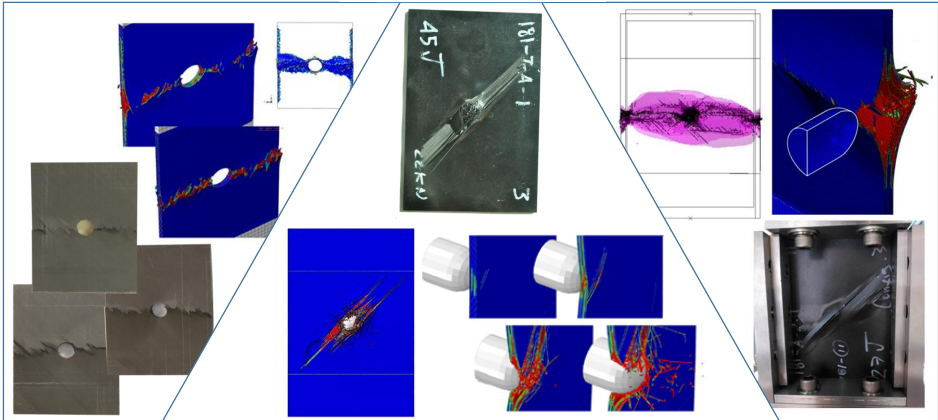
Figure 1.6: Virtual Coupon Testing, numerical versus experimental failure modes [14].

1.4 RESEARCH OBJECTIVES AND SCOPE

The objective of this research is to analyse matrix dominated failure of thermoplastic composites and conduction welded joints and to develop both experimental and numerical methodologies to support the design of thermoplastic composites structures. The research addresses important linkages between the three main pillars of *Manufacturing*, *Experimental* and *Numerical* analysis and special attention is paid to the influence of the manufacturing process on the mechanical behavior by evaluating both the autoclave and conduction welding manufacturing process. The relation of the individual chapters and their contribution to the research objective and scope is discussed next and shown in the schematic of Figure 1.7.

1

1.5 Dissertation outline and research approach

This thesis consists of four inter-linked chapters that contribute to addressing the overall research objective and scope. The chapters are directly reproduced from the scientific journal papers. Therefore, the readers can study the self-contained chapters independently. A result of this is that some essential information is repeated in each chapter. Another consequence is that the literature is reviewed in each chapter individually.

The chapter order is as follows:

Chapter 2 The importance of accounting for large deformation in continuum damage models in predicting matrix failure of composites

Chapter 3 Characterization and analysis of the interlaminar behavior of thermoplastic composites considering fiber bridging and R-curve effects

Chapter 4 Experimental and numerical evaluation of conduction welded thermoplastic composite joints

Chapter 5 Methodology for characterization and analysis of conduction welded thermoplastic composite joints while considering the influence of manufacturing

The schematic of Figure 1.7 provides an overview of the three main pillars of *Manufacturing*, *Experimental* and *Numerical* analysis and how each chapter contributes to the research objective and scope. The schematic shows how the methodologies of the individual pillars contribute towards design of thermoplastic composite structures (vertical flow), but at the same time it also provides insights into how each pillar is inter-linked (horizontal flow). This is briefly explained next.
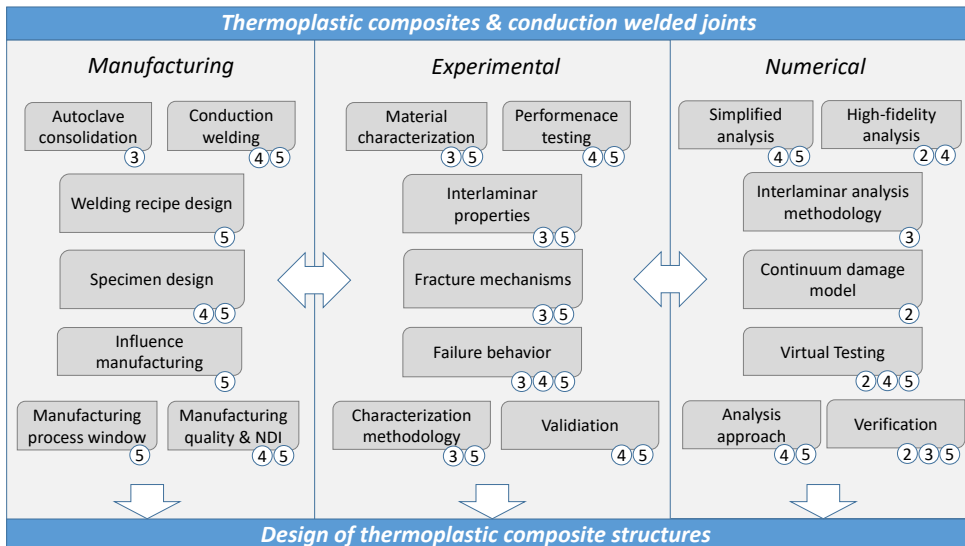
Figure 1.7: Schematic overview of the inter-linked chapters in relation to the research objectives and scope.

1

In *Chapter 2* a Continuum Damage Model (CDM) is developed which solves issues in the current state-of-art CDM's to predict matrix failure and ply splitting. This methodology improves the general Virtual Testing capabilities for both thermoset and thermoplastic composites and provides the baseline for the high-fidelity analyses in *Chapter 4*.

Due to the new fastener-free structural concepts and manufacturing techniques employed for thermoplastic composite structures, the performance of the thermoplastic polymer interface becomes more and more important. In *Chapter 3* the interlaminar behavior of autoclave consolidated thermoplastic composite material is characterized to provide input for the numerical analysis of *Chapter 4*. Special attention is paid to the validity of the testing methods and the more pronounced fiber bridging and R-curve effects of thermoplastic composites. Furthermore, the failure behavior and fracture mechanisms are studied in fine detail for comparison with the conduction welded joints in *Chapter 5*.

Chapter 4 consists of an experimental and numerical evaluation of conduction welded single lap shear joints. Both a simplified and high-fidelity analysis methodology is developed for welded joints and implemented in a framework for Virtual Testing. Both the experiments and analyses provide insights in the complex failure of the welded joints, but the interlaminar properties from the autoclave manufacturing process as measured in *Chapter 3* could not be directly related to strength of the joints. This work defined the need for a new methodology to determine the material properties of conduction welded joint in *Chapter 5* as it was found that the influence of manufacturing may play an important role.

The characterization of the welded joint material properties, as presented in *Chapter 5*, requires the design of specific specimens to account for the weldability of the coupons. The influence of the manufacturing process window in relation to the quality and performance of the welded joints is investigated through the design of different welding recipes. This window defines the relation of applied heat and pressure with the time during the manufacturing process. Characterization of the welded joints confirmed the findings in *Chapter 4* of the locally increased material properties which were also confirmed by changes in the fracture mechanisms in comparison to *Chapter 3*. Furthermore, the interlaminar analysis methodologies presented in *Chapter 3* provides new insights into the validity of the numerical analysis methodology and performance of the thermoplastic conduction welded joints for different manufacturing process conditions.

Finally, a broader perspective of the complete work is given in *Chapter 6* where the conclusions and recommendations are provided.

2

THE IMPORTANCE OF ACCOUNTING FOR LARGE DEFORMATION IN CONTINUUM DAMAGE MODELS IN PREDICTING MATRIX FAILURE OF COMPOSITES

The work presented in this chapter investigates the ability of continuum damage models to accurately predict matrix failure and ply splitting. Two continuum damage model approaches are implemented that use different stress-strain measures. The first approach is based on small-strain increments and the Cauchy stress, while the second approach account for large deformation kinematics through the use of the Green-Lagrange strain and the 2nd Piola-Kirchhoff stress. The investigation consists of numerical benchmarks at three different levels: (1) single element; (2) unidirectional single ply open-hole specimen and (3) open-hole composite laminate coupon. Finally, the numerically predicted failure modes are compared to experimental failure modes at the coupon level. It is shown that it is important to account for large deformation kinematics in the constitutive model, especially when predicting matrix splitting failure modes. It is also shown that continuum damage models that do not account for large deformation kinematics can easily be adapted to ensure that the damage modes and failure strength are predicted accurately.

2.1 Introduction

The aviation sector is moving towards more sustainable and affordable aircraft structures, which requires changes to be made in the way aircraft structures are designed and manufactured. An example is the development of a thermoplastic composite fuselage [9, 15] that makes use of new joining techniques such as thermoplastic welding. Although these new manufacturing techniques reduce the amount of mechanical fasteners required, they also make the strength of the structure more reliant on the matrix-dominated failure behavior of the thermoplastic material [12, 21]. With the recent advancements in the ability to accurately predict composite failure modes, there is now the opportunity to develop predictive tools to evaluate the strength and failure behavior of these new structural concepts and fastener-free joints. However, accurately predicting matrix dominated failure, in particular ply splitting cracks, still poses a number of difficulties.

Simulating the failure mechanisms in composites using finite element analysis [22–27] is generally done through modelling cracks using either discrete or smeared approaches [28]. Examples of discrete approaches include the extended finite element method (X-FEM) [29], the discrete cohesive crack approach [30], and the floating-node method [31]. These methods are capable to predict both the intra- and interlaminar damage mechanics with high accuracy, but generally at a high computational cost.

Maimí et al. [32] showed that cracks can also be represented in a more diffused manner by using a continuum damage mechanics (CDM) approach. In this case, crack propagation is represented by a softening law. Although softening results in a diffused crack unlike the real physical phenomenon at the micro-scale of the material, CDM provides an appealing framework to simulate the failure mechanisms at the meso-scale, as demonstrated by Lopes et al. [19] for various composite coupon tests in a virtual testing lab environment [16, 18].

From experimental observations of matrix-dominated damage in unnotched [33] and notched composite specimens [34–39], it is apparent that ply splits, and their interaction with delaminations [37] play an important role in the failure mechanics of composite materials. To address these difficulties, Lopes et al. [19] extended the CDM formulation of Maimí et al. [32] to three dimensions and combined it with several key modelling aspects to allow the appropriate kinematic simulation of composites. These key modelling aspects include (1) ply-by-ply modelling using fiber-aligned meshes and directional biasing; (2) nonlinear shear and mesh size regularization; and (3) an advanced element deletion scheme to guarantee solution robustness. Lopes et al. [19] also demonstrated that fiber-aligned meshes reduce the mesh-induced direction bias that is a source of mesh dependence in strain localization models. When fiber-aligned meshes are combined with large element aspect ratios, the mesh can direct matrix cracks to grow along the fiber direction, with the additional benefit of reducing computational cost [16]. However, it was found that rather large aspect ratios are required to prevent spurious failure modes and to achieve fully developed ply splits.

The difficulties of predicting ply splits with CDM models was also investigated by Leone [40], who developed a CDM methodology to represent the kinematics of matrix cracks in a deformable bulk material in accordance with the deformation gradient decomposition (DGD) methodology [40]. Leone [40] showed that CDM models, that do not account for large deformation kinematics, trigger spurious failure modes which make it difficult to predict ply splits. The DGD methodology, which does account for large deformation

kinematics, is able to overcome this issue. Unfortunately, the use of these advanced CDM models may also come at a cost, as they generally rely on several internal convergence loops, for example to (1) search for the correct through-thickness crack angle; (2) solve nonlinear shear equations; or (3) achieve convergence in equilibrium between crack and bulk material displacements. Furthermore, predicting the final failure modes at the coupon level when many elements are nearly fully damaged requires special attention to the robustness of the continuum damage model to prevent unintended termination of the analysis, as addressed by Lopes et al. [19].

Composites may also exhibit significant nonlinear behavior, especially in matrix-dominated loading conditions. The nonlinear response may result from a number of geometrical and material related mechanisms. This includes plasticity in the matrix, fiber-/matrix debonding, damage accumulation and reorientation of the fibers [41]. Lafarie-Frenot and Touchard [42] compared the in-plane shear behavior of thermoset versus thermoplastic composites and showed significant loss in shear stiffness and a nonlinear response for both materials. The thermoset composites reached shear strain values of approximately 5%, while the thermoplastic matrix showed a much more pronounce plastic behavior and failed at nearly 15% shear strain. The small degree of polymer deformation and the more brittle behavior of thermoset composites compared to thermoplastic composites can also be observed during interlaminar tests [43]. This is further confirmed by recent SEM micrographs of mode II interlaminar tests on thermoplastic composites presented by Tijs et al. [21], which feature significant polymer drawing out and extensive plastic deformation in the plane of the delamination.

The aim of this study is to investigate the influence of the different methodologies used in two recent continuum damage models [19, 40] to accurately predict ply splitting, and to propose an efficient methodology to improve CDM models for this specific failure mode. This focus is chosen to improve the methodology for future use in thermoplastic composites and conduction welded joints, as this material will experience much larger deformations within the matrix-dominated failure modes. As part of the investigation, a dedicated CDM model was developed to investigate different approaches while keeping the implementation based on a simple and efficient two-dimensional (2D) failure criteria. The investigation consists of numerical benchmarks at three different levels. The implication of using the different approaches are highlighted at each level and the results are compared to experimental data. In the next section, the CDM models used herein are briefly described, followed by the analysis and discussion of the CDM models at three different levels: (1) single element; (2) unidirectional (UD) single ply open-hole specimen; and (3) open-hole composite laminate coupon.

2.2 CDM Models

In this section, the different CDM models that are evaluated in this work are described. The first model, *CDM3D* [16, 19], was developed in collaboration between IMDEA Materials Institute and Fokker/GKN Aerospace. The second model, NASA *CompDam*, is based on DGD [44]. The response of these models is compared to two CDM models specifically designed for this study. The models include approaches from both the *CMD3D* and the *CompDam* models to study (1) the influence of using small strain increments (*CDM-SS*) and (2) accounting for large deformation (*CDM-LD*) kinematics. All other aspects of the CDM implementation are the same to ensure that the general response of the CDM models remain identical. A summary of the different models and their naming is defined as follows:

- *CDM3D*: 3D Continuum Damage Model [16, 19]
- *CompDam*: NASA CompDam DGD [44]
- *CDM-SS*: CDM approach based on Small Strain increments
- *CDM-LD*: CDM approach accounting for Large Deformation kinematics

CDM3D and *CDM-SS* are approaches that work well in situations where local deformations are not large, but they do not account for large deformation kinematics, while *CompDam* and *CDM-LD* are developed for geometrically nonlinear analysis. In addition to the aforementioned models, the Abaqus built-in Hashin model is also compared at the single element level. However, this model is not evaluated further as the response is similar to the other CDM models. All analyses were performed in Abaqus/Explicit [45].

2.2.1 CDM3D Model

The CDM3D model takes into account the three-dimensional (3D) stress state through the physically-based 3D failure criteria proposed by Catalanotti et al. [46]. The implementation is described in full detail by Lopes et al. [19] and is originally based on the work of Maimí et al. [47] that guarantees the correct energy dissipation for each fracture mode in a composite material. The laminate compliance tensor, $[H(d_M)]$, is affected by the damage variables in each orthotropic direction $d_M (M = 1\pm, 2\pm, 3\pm, 4, 5, 6)$, as shown in Figure 2.1, and is associated with the damage evolution laws for each failure mode. Each damage evolution

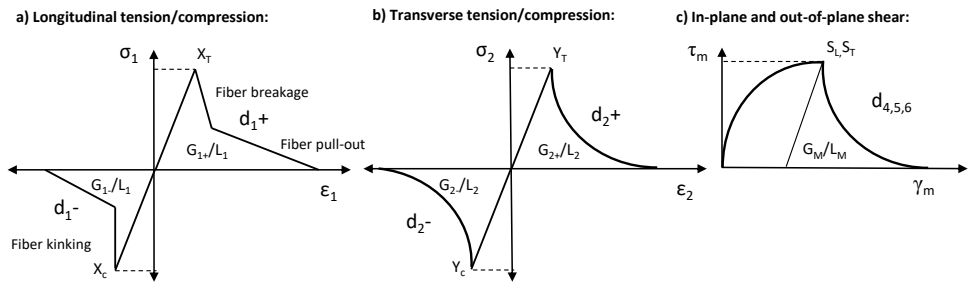Figure 2.1: CDM3D damage laws: a) longitudinal tension/compression, b) transverse tension/compression, c) in-plane and out-of-plane shear.

law is defined by the strength $(X_t, X_c, Y_t, Y_c, S_L, S_T)$, fracture toughness (G_M), and element direction $(L = 1, 2, 3)$ of the corresponding failure mode, respectively in fiber longitudinal tension/compression (Figure 2.1a), matrix transverse tension/compression (Figure 2.1b),

and matrix shear (Figure 2.1c). Out-of-plane tension ($M = 3_+$) is disabled and accounted for by the interlaminar model. The shear components follow elasto-plastic behavior defined by nonlinear relationships based on explicit forms of the Ramberg-Osgood law. Fiber failure is implemented using a superposition of cohesive laws to represent the different fiber failure modes such as fiber breakage, pull-out and kinking as proposed by Dávila et al. [48].

The corresponding compliance tensor with damage follows the Abaqus/Explicit convention and is expressed as:

$$[H(d_M)] = \begin{bmatrix} \frac{1}{(1-d_1)E_1} & -\frac{v_{12}}{E_1} & -\frac{v_{12}}{E_1} & 0 & 0 & 0 \\ -\frac{v_{12}}{E_1} & \frac{1}{(1-d_2)E_2} & -\frac{v_{23}}{E_2} & 0 & 0 & 0 \\ -\frac{v_{12}}{E_1} & -\frac{v_{23}}{E_2} & \frac{1}{(1-d_3)E_3} & 0 & 0 & 0 \\ 0 & 0 & 0 & \frac{1}{(1-d_6)G_{12}} & 0 & 0 \\ 0 & 0 & 0 & 0 & \frac{1}{(1-d_4)G_{23}} & 0 \\ 0 & 0 & 0 & 0 & 0 & \frac{1}{(1-d_5)G_{13}} \end{bmatrix} \tag{2.1}$$

An advantage of this approach is that the damage behavior of each orthotropic direction can be individually defined, but it also requires correct coupling of damage variables that may influence softening in a specific direction depending on the crack orientation. Related to this study, it is important to consider that the stress-strain measure in this model follows the CDM approach based on small strain increments.

2.2.2 COMPDAM MODEL

The CompDam model [44] was developed to accurately represent the kinematics of composite damage, and in particular for the simulation of matrix cracks formed under tension, compression, and shear loading conditions. The kinematics of a matrix crack are represented by treating them as a cohesive crack embedded in a deformable bulk material, and the relative contributions of the crack opening and bulk deformation are determined in accordance with the DGD methodology. The method uses additive decomposition of the deformation gradient tensor into 'bulk material' and 'crack' components as compared in Figure 2.2 to a continuum during shear deformation. In the DGD methodology, the cohesive displacement-jump vector, $\boldsymbol{\delta}$, represents the deformation on an embedded cohesive crack. Matrix damage is accounted for in the embedded cohesive crack, while fiber damage is modelled using strain-softening, as shown in Figure 2.1(a). Fiber damage is, as in *CDM3D*, based on superposition of cohesive laws. The shear components follow elasto-plastic behavior defined by nonlinear relationships based on the Ramberg-Osgood law, however, unlike *CDM3D*, this has to be solved using the Newton-Raphson method. The DGD methodology returns a single damage variable (d_2) for the softening behavior, which is coupled with the 3-direction depending on the crack orientation because the model can distinguish between a matrix crack and delamination. An advantage of the DGD approach is that the damage of the continuum can be directly related to the orientation of the crack and mixed-mode conditions can be accurately derived from the crack opening displacement-jump. A disadvantage is that the methodology requires internal convergence loops to solve the displacement jumps, which may affect computational efficiency and solution robustness. Related to this study, it is important to consider that the stress-strain

measure in this model accounts for large displacement in geometrically nonlinear problems in Abaqus/Explicit.
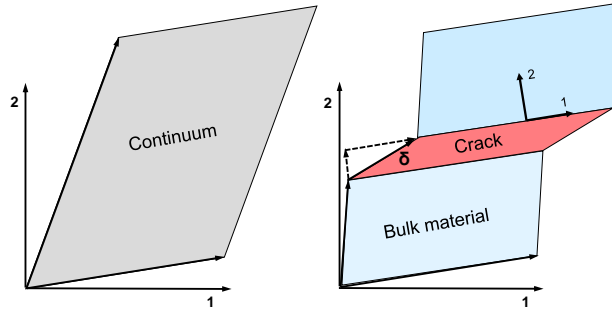
Figure 2.2: CompDam DGD decomposition of crack and bulk material in a continuum element.

2.2.3 CDM-SS and CDM-LD Models

The intralaminar CDM models in this study were implemented through a user-defined "VUMAT" subroutine using a numerically explicit integration scheme and are based on the Puck 2D failure criterion [49–51]. The failure criteria provides a closed-form solution for the fracture plane angle. Since an iterative procedure to determine the fracture plane angle is not required, this methodology is computationally efficient. The theory classifies lamina failure by Fiber Fracture (FF) and Inter-Fiber-Fracture (IFF), also referred to as fiber and matrix failure, respectively. Fiber failure in tension and compression follows a simple maximum stress formulation, while matrix failure is described by three failure modes. Failure due to matrix tension and/or in-plane shear is referred to as Mode A and results in a fracture plane angle equal to zero. The fracture angle remains at zero degree during moderate combined loading in shear and compression, identified as Mode B. As compressive loads increase, the fracture plane angle increases up to 54 degree in pure compression. This final fracture mode is identified as Mode C. The implemented version as detailed in Appendix 2.A of the 2D Puck failure criteria follows the VDI-guideline VDI2014, Part 3 [52], which includes weakening of the matrix strength due to high fiber stresses [51].

After the onset of damage, strain-softening laws are used to damage the ply for each in-plane failure mode $(d_{1\pm}, d_{2\pm}, d_6)$ as shown in Figure 2.1. Softening in the fiber direction is implemented through the trilinear softening law of the CompDam implementation [44]. For matrix failure, the equations for exponential softening from Maimí et al. [47] are used to ensure that the computed dissipated energy is independent of mesh refinement. The maximum element size for each failure mode is calculated according to the crack band model [53], where the characteristic element length is calculated for a material-aligned meshing strategy following the modeling approach defined in [16]. The damage and internal parameters are also used to allow for closure of transverse cracks under load reversal. Depending on the sign of the normal stress, a damage mode can be either activated or disabled. It is assumed that a tensile matrix crack (Mode A) can be closed in compression

(Mode B), while shear cracks and cracks with fracture angles higher than 0° (Mode C) can not be closed. Shear damage (d_6) is coupled by both fiber and matrix failure [47] in damaging the stiffness matrix. Frictional effects are not considered in the model.

Shear nonlinearity in the 1-2 plane is modelled using the Ramberg-Osgood equation based on the CompDam implementation [44], where the parameters are obtained from fitting experimental in-plane shear tests. The response is assumed to be plastic until the onset of damage, after which the element is damaged following an exponential softening law that is regularized according to the mode II fracture toughness. Nonlinear behavior in other directions is not considered. Finally, an element deletion strategy is implemented in order to avoid excessive element distortion which may significantly influence the runtime of the analysis or even crash it. These highly distorted elements generally exhibit sudden changes in volume that can be detected through the determinant of the deformation gradient det($\mathbf{F}$) [54]. The criteria for element deletion is adopted from [16], and is set to be more strict during very large deformations. For fiber failure, the elements are deleted once the damage variable becomes nearly one ($d_{1\pm} \geq 0.99999$). Furthermore, the elements are also deleted if any of the strains becomes larger than one ($|\epsilon_i| \geq 1.0 (i = 1, 2)$; $\gamma_i| \geq 1.0 (i = 12)$). Finally, the elements are also deleted if large volume changes occur (det($\mathbf{F}$) ≤ 0.4 or det($\mathbf{F}$) ≥ 4.0). This strategy ensures that elements are only deleted if they are highly deformed or damaged and no longer carry any loads, as early deletion or limiting damage variables might influence the final failure modes.

The main difference between the two models presented in this study is related to the definition of the stress-strain measures and how the material axis rotates during geometrically linear and nonlinear analyses. During geometrically nonlinear analyses (NLGEOM=YES) the strain increment given by Abaqus/Explicit follows a co-rotational coordinate system where the material axis is rotated with the element, while for geometrically linear analyses this is not the case. An example of the material axis rotation during simple shear deformation for both cases is given in Figure 2.3.
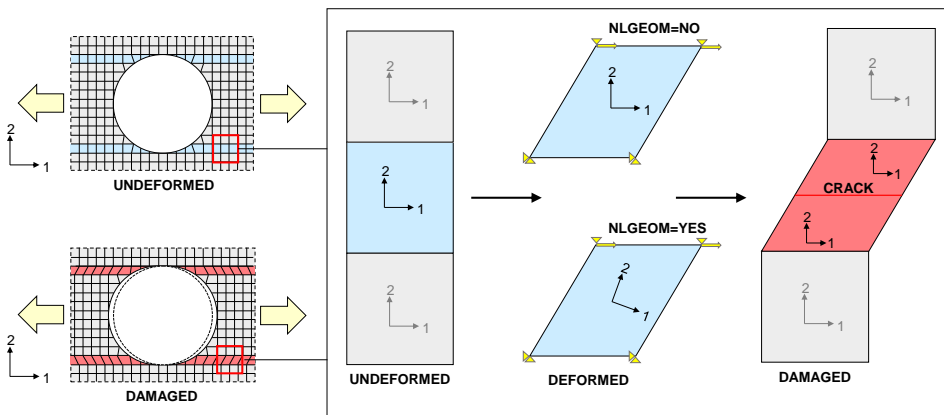
Figure 2.3: Element deformation of Continuum Damage Model during ply splitting and default local coordinate system in Abaqus/Explicit.

The desired element deformation and crack orientation during the damaged state is also given. If the strain is derived following the material rotation in the deformed situation during geometrically nonlinear analyses, then the damaged compliance tensor, as described in equation (2.1), would also follow this rotation and may cause issues with incorrectly defined orientation of the softening directions. The incorrectly defined matrix crack orientation due to material axis rotation may cause load transfer across matrix cracks, where the strain and/or rotations due to softening and material nonlinearity may become large enough to invalidate the assumptions inherent to small strain theory. This can then trigger spurious secondary failure mechanisms such as fiber failure [40]. Both the approach of the *CDM3D* model and a simplified version of the large deformation approach of *CompDam* are implemented in the CDM in order to investigate if only accounting for large displacements and rotation on the element deformation would be sufficient to predict ply splitting. Both implementations are briefly explained next.

CDM-SS: CDM approach based on Small Strain Increments
In CDM models [47], the presence of a crack is often accounted for by damaging the stiffness tensor, $\mathbf{C}$. The damaged stiffness tensor, $\mathbf{C^d}$, is used to calculate the stress, $\boldsymbol{\sigma}$, from the current strain, $\boldsymbol{\epsilon}$, without explicitly modeling the crack. The total strain, $\boldsymbol{\epsilon}$, is calculated by adding the strain increment, $\Delta\boldsymbol{\epsilon}$, given by Abaqus/Explicit to the total strain from the previous step for each time increment ($\boldsymbol{\epsilon} = \boldsymbol{\epsilon}_{prev} + \Delta\boldsymbol{\epsilon}$).

$$\boldsymbol{\sigma} = \mathbf{C^d} : \boldsymbol{\epsilon} \tag{2.2}$$

An alternative approach that yields the same result as using small strain increments is based on the logarithmic strain and Cauchy stress. The logarithmic strain tensor, $\mathbf{E}_{log}$, can be calculated from the stretch and is defined as [55]

$$\mathbf{E}_{log} = \mathbf{P} \cdot ln\mathbf{\Lambda} \cdot \mathbf{P}^T \tag{2.3}$$

where $\mathbf{P}$ and $\mathbf{\Lambda}$ are, respectively, the matrices of the eigenvectors and eigenvalues of the stretch, $\mathbf{U}$. The stress, $\boldsymbol{\sigma}$, is then calculated using Hooke's law and $\mathbf{C^d}$.

In this approach, the damaged stiffness tensor follows the material rotation in the deformed situation as the stress-strain measure is derived for the current configuration and nodal positions. The CDM model with this implementation is referred to as *CDM-SS* and is compared to *CDM3D* in this study.

CDM-LD: Approach accounting for Large Deformation Kinematics
The large deformation approach [56] is based on a Lagrangian kinematic measure where the constitutive equations can be defined within a orthonormal material frame. The Green-Lagrange strain, $\mathbf{E}_{GL}$, is determined from the deformation gradient tensor, $\mathbf{F}$:

$$\mathbf{E}_{GL} = \frac{1}{2} \left(\mathbf{F}^\top \cdot \mathbf{F} - \mathbf{I} \right) \tag{2.4}$$

where $\mathbf{I}$ is the identity tensor. The 2nd Piola-Kirchhoff stress, $\mathbf{S}$, can be determined from $\mathbf{E}_{GL}$ and $\mathbf{C}^d$:

$$\mathbf{S} = \mathbf{C}^d : \mathbf{E}_{GL} \tag{2.5}$$

S can be mapped to the current configuration by

$$\boldsymbol{\tau} = \mathbf{F} \cdot \mathbf{S} \cdot \mathbf{F}^T \text{ and } \boldsymbol{\sigma} = \frac{1}{J} \boldsymbol{\tau} \text{ with } J = \det(\mathbf{F}) \tag{2.6}$$

where $\boldsymbol{\tau}$ is the Kirchhoff stress. The stresses need to be rotated back to the co-rotational basis of Abaqus through the use of a rotation matrix, $\mathbf{R}$.

$$\boldsymbol{\sigma}_{abq} = \mathbf{R} \cdot \boldsymbol{\sigma} \cdot \mathbf{R}^T \tag{2.7}$$

In this approach, the stress-strain measure used for the calculation of damage is derived based on the reference configuration. The CDM model with this implementation is referred to here as *CDM-LD* and is compared to *CompDam*.

2.3 Numerical Analysis and Discussion

The different methodologies described in Section 2.2 are applied to geometrically nonlinear problems involving large shear deformation, and the effect of each methodology is analyzed in this section. The models are evaluated at three different levels as shown in Figure 2.4: (1) Single element simple shear; (2) Splitting of an open-hole UD ply; and (3) Open-hole tension of a composite laminate coupon. The benchmarks are chosen so that the influence of the differences in methodology can be highlighted at each level under loading conditions that are representative for ply splitting. Both the single element and open-hole UD ply benchmark are loaded in fiber direction (material axis 1) as shown in Figure 2.3.   The
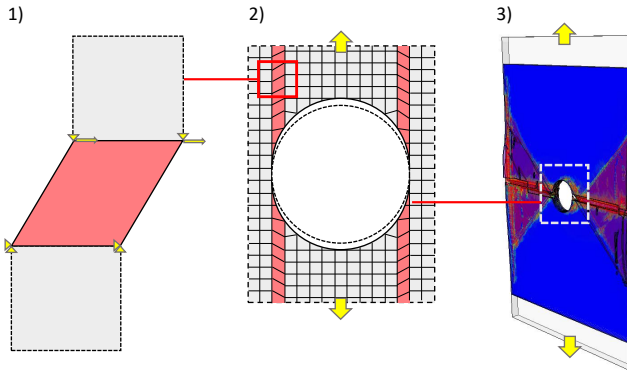
Figure 2.4: Benchmarks at three different levels: (1) Single element simple shear; (2) Splitting of an open-hole UD ply and (3) Open-hole tension of a composite laminate coupon

benchmark at the single element and UD ply level follow the modeling approach described in [40]. The high-fidelity modeling of the open-hole coupon takes into account both inter- and intralaminar damage, where ply-by-ply modeling is employed. The interlaminar behavior is modelled through the general contact algorithm available in Abaqus/Explicit [45], which accounts for the kinematics of surface contact, cohesive separations and friction [16, 19]. For some of the studies presented in this section, the influence of linear shear (*LS*) versus nonlinear shear (*NLS*) is investigated.

2.3.1 Material Properties

The material properties for AS4/8552 and IM7/8552 used in this study are given in Table 2.1. Only the properties relevant for the benchmarks are shown, while the full set is provided in [16, 44].

Table 2.1: Material properties of AS4/8552 [16] and IM7/8552 [44].

Property	Description	AS4/8552	IM7/8552	Unit
E_{11}	Young's modulus, longitudinal tensile direction	137100	171420	MPa
E_{22}	Young's modulus, transverse tensile direction	9456	9401	MPa
G_{12}	Shear modulus	4992	5290	MPa
ν_{12}	Poisson ratio, 1-2	0.314	0.32	-
ν_{23}	Poisson ratio, 2-3	0.487	0.52	-
Y_T	Mode I matrix strength	74.2	80.0	MPa
S_L	Mode II matrix strength	97.53	92.3	MPa
X_T	Fiber tensile strength	2106.4	2326.2	MPa
G_{Ic}	Mode I interlaminar fracture toughness	0.3	0.3	kJ/m^2
G_{IIc}	Mode II interlaminar fracture toughness	0.78	0.788	kJ/m^2
η	Benzeggagh-Kenane coefficient	1.45	1.634	-
G_{XT}	Longitudinal tensile fracture toughness	125	133.3	kJ/m^2

2.3.2 Single Element Simple Shear

An eight-node C3D8R solid single element is loaded in simple shear as shown in Figure 2.3. The size of the element is 0.1 mm in each direction and the AS4/8552 material properties are given in Table 2.1. The fiber direction is aligned with the 1-direction. The bottom 4 nodes are constrained in all directions, while the top nodes are constrained in 2 and 3-direction. The element is loaded at the top nodes in 1-direction by an applied displacement of 0.1 mm.

The softening of the single element is studied by summing the reaction forces in 1-direction of the top nodes. The shear stress and strain provided by Abaqus is not reported here because they are provided in the rotated material direction. If the user is not aware of this material axis rotation, the softening behavior appears to be as expected in material direction stress/strain, however not in terms of stress based on the reaction forces. The expected response is linear-elastic before the onset of damage (d_m = 0) followed by linear softening until the reaction force reaches zero (d_m = 1).

The results of the single element analysis is shown in Figure 2.5. The Abaqus built-in Hashin material model is used first. The influence of the material axis rotation as illustrated in Figure 2.3 on the reaction forces in 1-direction during a geometrically nonlinear problem (NLGEOM=YES) is compared to the results of a linear analysis (NLGEOM=NO). Both models show identical response during the linear-elastic part and onset of damage is predicted at the same point. However, the softening response shows very different results. During the softening of the geometrically nonlinear analysis, the reaction force starts picking up load in the 1-direction due to the rotation of the material axis and incorrectly defined crack plane. Furthermore, the incorrectly defined material coordinate system also results in the development of spurious stresses. For example, the stress in fiber direction rapidly increases and results in the onset of compressive fiber damage (d_f onset) at large shear strains.

2
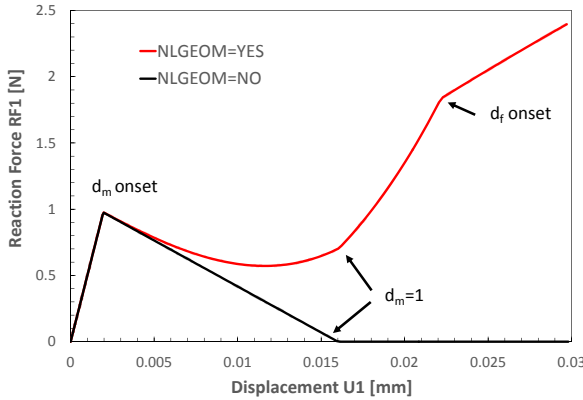
Figure 2.5: Single element reaction force (RF1), simple shear loading, Abaqus build-in Hashin material model.

The single element model is further studied using the different approaches and the results are compared against *CDM3D* and *CompDam* in Figure 2.6 during a geometrical nonlinear analysis (NLGEOM=YES). It is shown that *CDM3D* and *CDM-SS*, which do not account for material axis rotation, show the same softening response as the Hashin model (Figure 2.5) with a slight difference in the onset of fiber failure due to the difference in failure criteria. However, the softening response of *CompDam* and *CDM-LD* is correct. The only difference between the models is the implementation of the softening law, which is linear in *CompDam* and exponential in the other models.
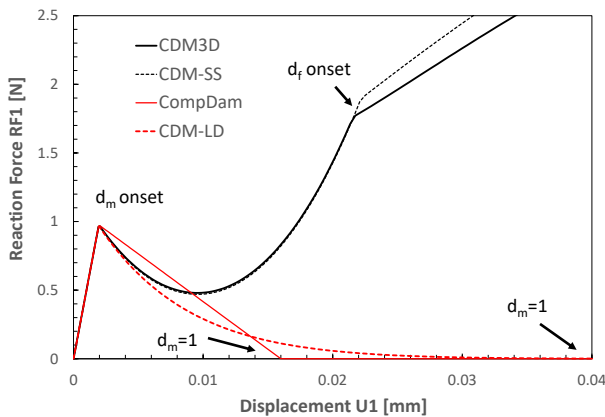
Figure 2.6: Single element simple shear loading, comparing the reaction force (RF1) of the different models during geometrical nonlinear analysis (NLGEOM=YES).

The development of spurious stresses, and ultimately compressive fiber failure (d_f) at large shear strains is also predicted by the models that do not account for material axis rotation (*CDM3D* and *CDM-SS*). Furthermore, a compressive force increases during shear loading as shown in Figure 2.7, while the transverse force resulting from shear damage predicted by *CompDam* and *CDM-LD* is negligible. It should be noted that when using *CDM-LD* or *CompDam* in a geometrically linear analysis with NLGEOM=NO, the stresses are over-rotated, which causes a similarly incorrect load-transfer across the element.
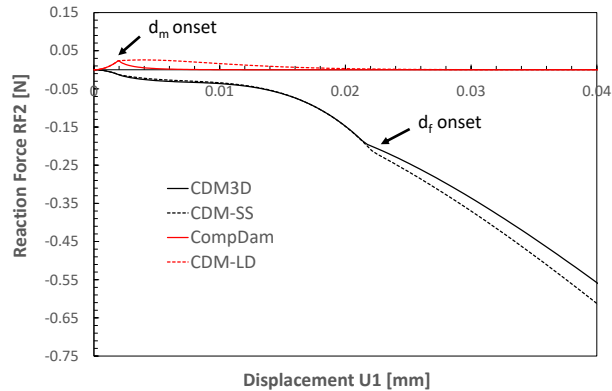
Figure 2.7: Single element simple shear loading, comparing the reaction force (RF2) of the different models during geometrical nonlinear analysis (NLGEOM=YES).

2.3.3 UNIDIRECTIONAL SINGLE PLY OPEN-HOLE TENSION SPECIMEN

The second evaluation of CDM models in the present study concerns their ability to predict fiber splits in a UD single ply open-hole specimen following the benchmark in [44]. This benchmark is chosen because it shows how fiber splitting influences the stress-concentration around the hole and failure mode of the UD single ply open-hole specimen [35]. The prediction of fiber splitting is difficult because of the large shear deformation that occurs near the hole after onset of matrix damage as shown in Figure 2.3. The UD open-hole model is shown in Figure 2.8 and is 50.8–mm long, 12.7–mm wide with a hole of 3.175 mm in diameter. Only a single ply is modelled, meaning the thickness of the specimen is 0.183 mm. The modeling strategy follows the approach defined in [16] with a fiber aligned mesh. The expected failure mode of the UD open-hole specimen is a net-section fiber failure of the remaining ligaments after the stress-concentration of the hole has been reduced by fiber splitting. The fibers are aligned with the loading direction and a fiber-aligned structural mesh is used. The elements are 0.127 mm in the transverse direction and have an aspect ratio of 3 in the longitudinal direction, resulting in an element length of 0.38 mm. The element size is chosen such that they meet the requirements for mesh regularization without experiencing snap-back behavior during softening [16]. The IM7/8552 material properties used in this study are given in Table 2.1.
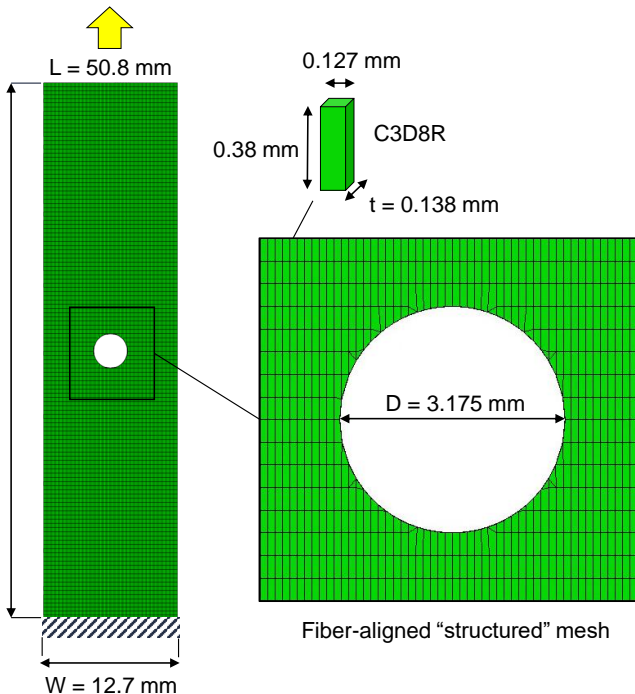
Figure 2.8: Unidirectional single ply open-hole tension model, following dimensions from [40].

The theoretical UD net-section strength of the open-hole specimen without stress concentration is $X_T \cdot (W - D) \cdot t_{ply}$ = 4054 N. The prediction of the load-displacement curve, during a geometrical nonlinear (NLGEOM=YES) analysis, for both the *CDM3D* and *CompDam* model is shown in Figure 2.9. The prediction of the initial stiffness and onset of fiber splitting (1) is very similar between the models. The *CDM3D* model, which does not account for material rotation, is unable to reduce the stress concentration at the hole. As soon as the shear deformation within the splits becomes large enough to trigger spurious failure modes the load-displacement curve drops (2) and the *CDM3D* specimen fails (3). In contrast, the *CompDam* model exhibits fully developed fiber splits from end to end (2) which greatly reduces the stress concentration such that the central region carries no load (4). As expected, final failure of the specimen (5) is governed by fiber failure in the remaining ligaments. The colors in Figure 2.9 (1), (2), (3) and (5) represent element damage (blue = undamaged, red = fully damaged), while the colors in (4) indicate the amount of stress carried by the ligaments related to the UD net-section strength.
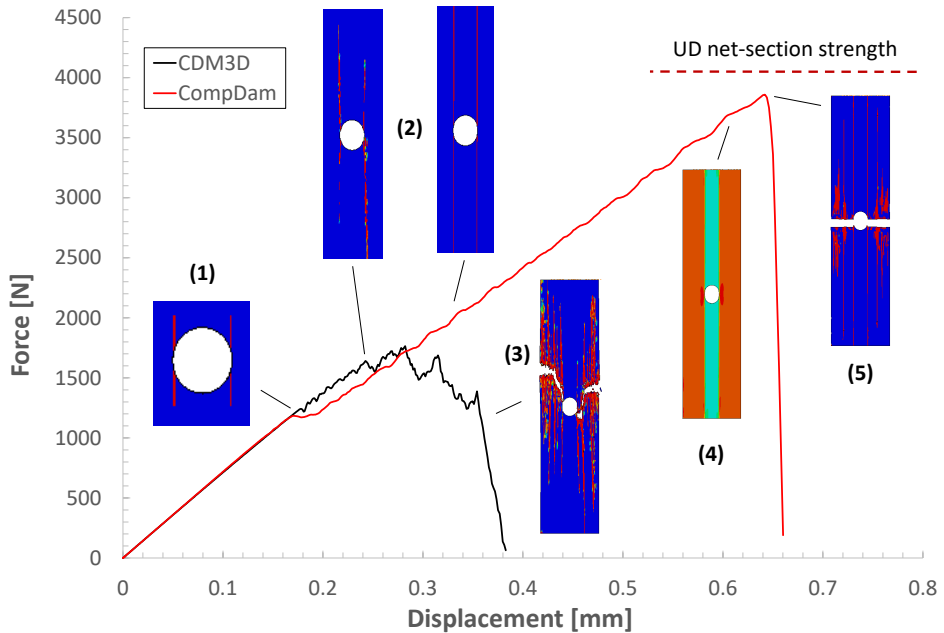
Figure 2.9: Load-displacement curves of the UD open-hole ply split benchmark with comparison of difference in failure modes between *CDM3D* and *CompDam* model.

The benchmark is repeated with *CDM-SS* and *CDM-LD* to investigate how the difference in methodology affects the prediction of fiber splits and final failure of the UD open-hole specimen. In addition, the effect of shear non-linearity is investigated. The load-displacement predictions are shown in Figure 2.10 and the corresponding failure modes are presented in Figure 2.11.

The initial linear-elastic response of the load-displacement curve is identical for both models up to the onset of matrix failure and fiber splitting. For the *CDM-SS* model (which does not account for material rotation), the inclusion of nonlinear shear in the analysis slows the development of the splits (1) and promotes the development of spurious failure modes causing early failure of the specimen (2). For *CDM-LD*, there is no significant impact of material nonlinearity on final specimen strength (3) and ply splitting is accurately captured.
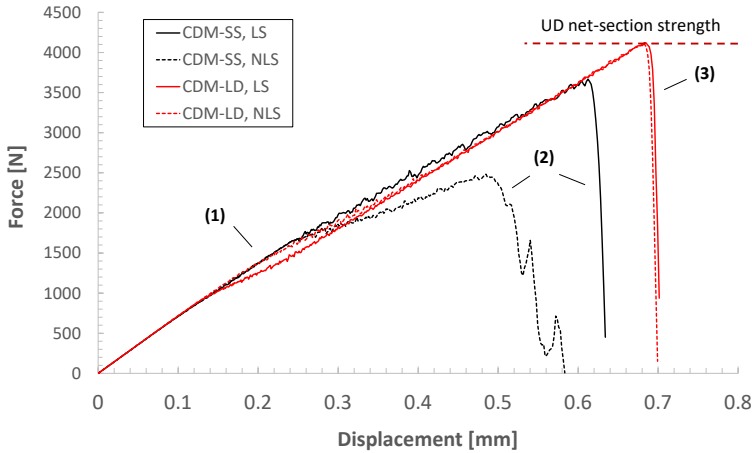
Figure 2.10: Prediction of UD open-hole ply splitting, linear versus nonlinear shear using the two different approaches. The failure modes at three points are compared in Figure 2.11.
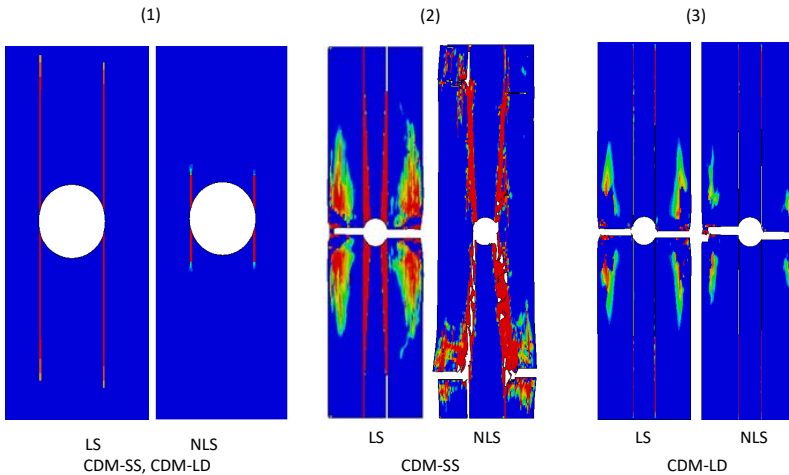
Figure 2.11: Comparison of the UD open-hole failure modes from Figure 2.10: (1) initiation of ply splitting; (2) *CDM-SS*, LS vs NLS; (3) *CDM-LD*, LS vs NLS.

During the analysis, failure onset during shear loading is defined at 5% shear strain, which is a typical value for thermoset composites [42]. The introduction of nonlinear shear in the analysis showed a significant effect on the strength prediction and failure mechanics. Therefore, it becomes apparent that the effect of these spurious failure modes may play an important role in the final failure modes at laminate level and could be especially important for materials such as thermoplastic composites, which allow for even higher deformations within the local failure modes.

2.3.4 Open-Hole Tension Laminate

The previous section clearly demonstrates that, to predict fiber splitting on unidirectional plies, it is necessary to account for large deformation kinematics. In this section, the effect of the modeling approaches is evaluated in the case of a multi-directional laminate typical of applications in the aerospace industry. The open-hole tension specimen of the hard laminate presented in [16] is chosen for this study and is referred to as [50/40/10], which stands for the percentage of 0-, ± 45- and 90-degree plies. Fiber failure is modelled differently between the models and the (3D vs 2D) failure criteria. Also, the shape of the cohesive law for fiber failure has a pronounced effect on the coupon strength at laminate level, which is not part of the current study. Therefore, only matrix damage and delamination is compared between the models and no load-displacement curves are shown. The finite element model of the open-hole tension laminate is shown in Figure 2.8 and is 38.1 mm wide, 65 mm long and has a hole with a diameter of 6.35 mm. The laminate consists of 20 plies ($[0/45/0/90/0/-45/0/45/0/-45]_s$). The modeling strategy follows the approach defined in [16, 19] and each ply consists of a fiber aligned mesh. The interlaminar behavior is
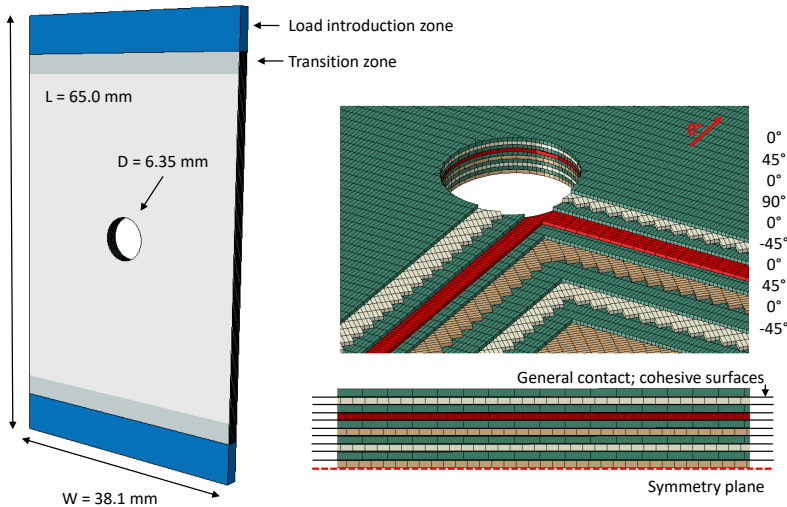
Figure 2.12: Finite element model of the open-hole tension laminate specimen.

modelled through the general contact algorithm available in ABAQUS/Explicit [45] to solve the issues of the non-coincident fiber aligned mesh and takes care of the kinematics of surface contact, cohesive and frictional behavior. Interlaminar damage (delamination) is

described in terms of tractions and displacements by the cohesive zone model. The model reduces the stiffness of the cohesive surface thus decreasing the traction while dissipating the fracture energy corresponding to the specific mixed-mode opening mode. Mixed-mode interaction follows the Benzeggagh-Kenane criterion [57]. The quadratic nominal stress failure criteria is used for damage initiation and based on the interlaminar strength values for each damage mode. The corresponding material properties are given in Table 2.1. A value of 200000 N/mm^3 is used for the mode I penalty stiffness and the shear penalty stiffness follows Turon's equation [58]. Frictional effects are considered to be ply interface angle dependent and follows the approach and values from [16, 19]. Symmetry through the thickness is used to reduce the computational cost. The material properties of each ply take into the account their in-situ strength. The load is introduced into the coupon through a 'load introduction zone' with linear-elastic properties and a 'transition zone' with increased fracture toughness in order to mitigate the influence of the boundary conditions and edge.

The prediction of the failure mode of the [50/40/10] open-hole tension test by using the CDM approaches (1: *CDM3D*, 2: *CDM-SS*) is shown in Figure 2.13. As expected, the final failure of the open-hole tension test is dominated by fiber failure due to the large number of 0-degree plies. Both models predict a clean net-section failure with limited matrix damage and delaminations.
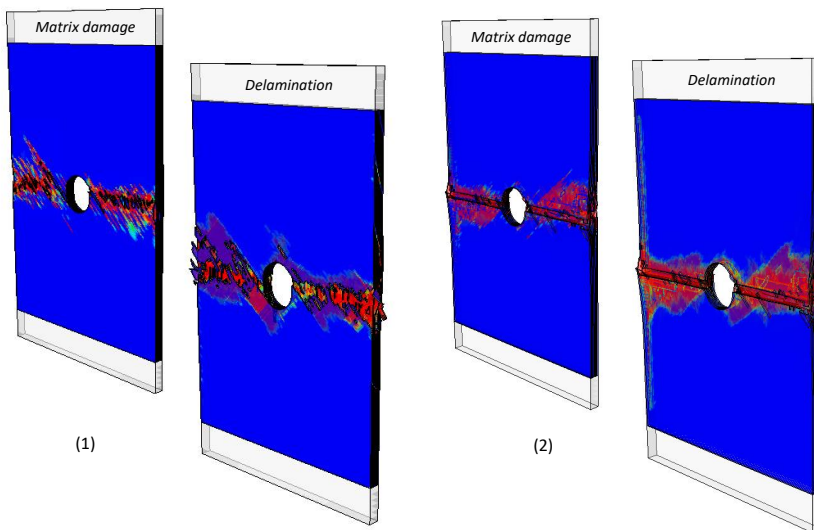
Figure 2.13: Failure mode of [50/40/10] open-hole tension analysis: (1) *CDM3D*; (2) *CDM-SS*.

The predictions of the failure mode of the open-hole specimen by the *CompDam* and *CDM-LD* model is shown in Figure 2.14. Although final failure of the coupon is still dominated by fiber failure, the development of internal matrix damage, fiber splits and their interaction with delaminations is very different compared to Figure 2.13. The large difference in predicted failure modes demonstrates that accounting for large deformations appears to also be important at the laminate level as ply splitting will highly influence the development of delaminations.
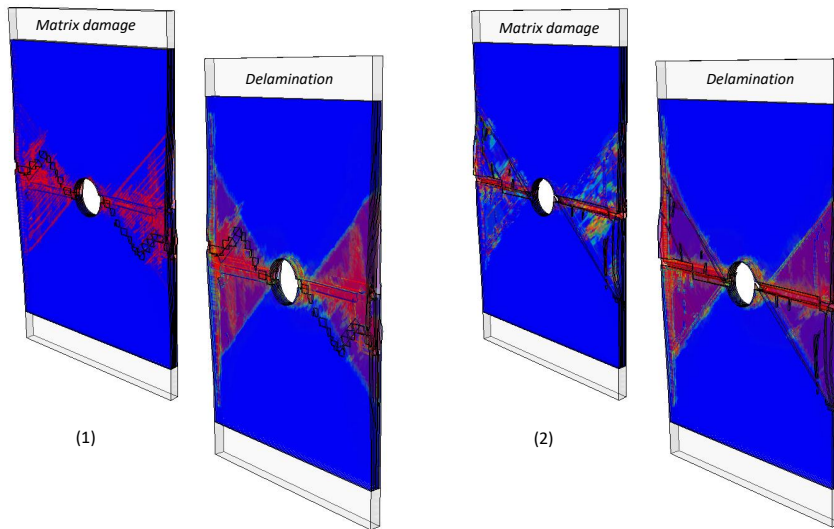
Figure 2.14: Failure mode of [50/40/10] open-hole tension analysis: (1) *CompDam*; (2) *CDM-LD*.

A closer look at the failure mode reveals similar issues as identified by the previous described test cases. Within the matrix cracks and ply splits there are signs of spurious failure modes, which triggers incorrect failure of elements in their surrounding. A sign of compressive fiber failure using the *CDM3D* model (1) is shown in Figure 2.15, while *CDM-LD* shows large shear deformation at the local scale within the fully developed matrix splits (2). The presence of high shear strains within the splits demonstrates that it is important to account for large deformation kinetics in the constitutive model, even in the case of thermoset materials that typically fail around 5% shear deformation.
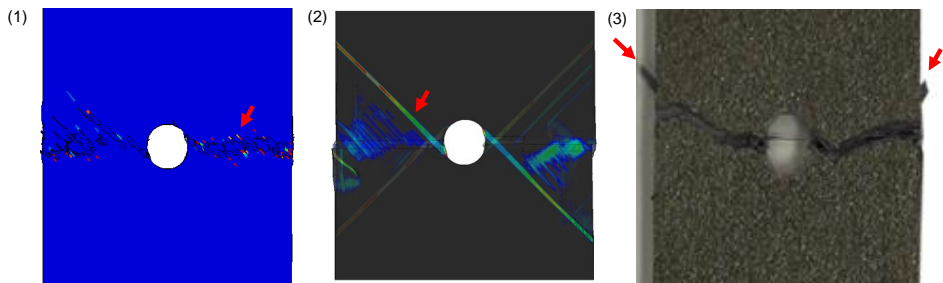
Figure 2.15: Detailed look at failure mode of [50/40/10] open-hole tension analysis: (1) *CDM3D*, compressive fiber failure within matrix splits; (2) *CDM-LD*, large shear deformation (5-50%) at the local scale within fully developed matrix splits; (3) Indication of ply splits in published experimental failure mode open-hole, adapted from [16]

The development of matrix cracks, ply splits and their interaction is shown in Figure 2.16. Matrix damage starts to develop near the edges of the hole on each ply in the direction of the fiber (1). Fiber damage initiates along the net section of the hole and delamination starts to interact with the ply splits near the hole following the 45-degree plies (2). The fibers near the hole become fully damaged and some elements are removed. A strong interaction between the ply splits and delamination is observed (3) until they reach the edges of the coupon (4). Similar internal failure modes can be observed in the experimental results and in the literature [37, 38, 59]. The failure mode of a [50/40/10] open-hole tension laminate is shown in Figure 2.17-3 and the directions of ply splits are marked. The experimental data shown in [16] shows a net-section failure mode, but the coupon is not fully separated. However, after full separation of a specimen from the same testing campaign, it can be concluded that internal failure modes similar to those predicted by the *CompDam* and *CDM-LD* model are present in the experimental data and that ply splits and delaminations follow the 45-degree plies.
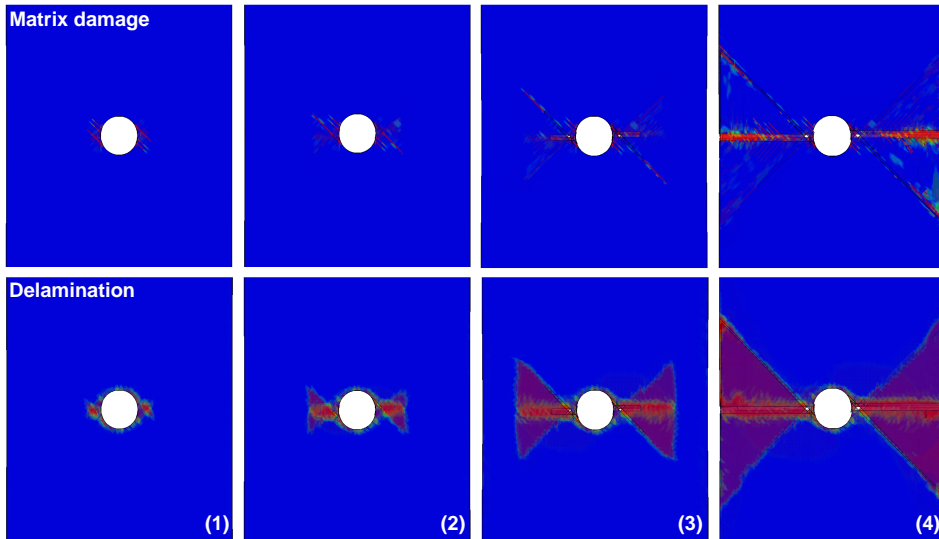
Figure 2.16: Development of matrix damage, ply splits and interaction with delamination using *CDM-LD* model: (1) initiation of damage near hole edge; (2) Start of fiber damage and ply splits; (3) Propagation of ply splits and interaction with delamination; (4) Final failure mode.
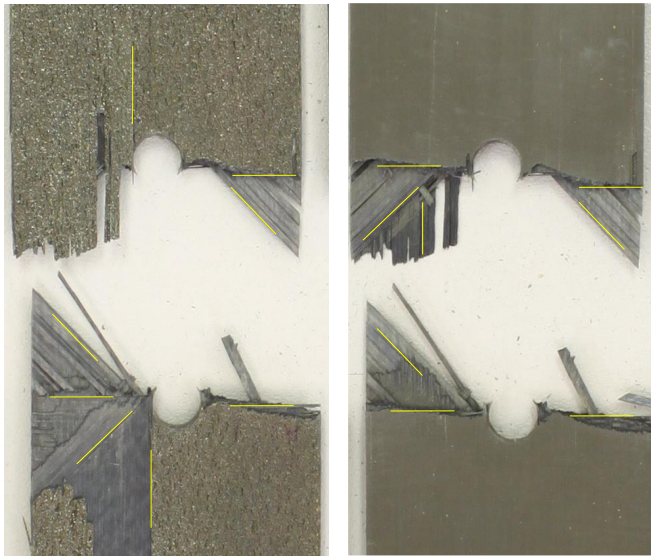
Figure 2.17: Experimental failure mode of open-hole laminate after full separation of the fully failed laminates, ply split directions marked in yellow.

2.4 Conclusion

The importance of accounting for large deformation in predictions of matrix failure of composites is demonstrated in this paper. The constitutive behavior of two recently developed continuum damage models is investigated. Two continuum damage model approaches are implemented that use different stress-strain measures. The first approach *CDM-SS* is based on small-strain increments and the Cauchy stress, while the second approach *CDM-LD* accounts for large deformation kinematics through the use of the Green-Lagrange strain and the 2nd Piola-Kirchhoff stress. The ability of the CDM models to predict matrix failure and ply splitting is evaluated by benchmarks at the single element, ply and coupon level. It is found that approaches based on small strain increments and logarithmic strains run into difficulties during large shear deformation as spurious stresses trigger incorrect failure modes. The incorrectly defined matrix crack orientation due to material axis rotation may cause load transfer across matrix cracks, where the strain and/or rotations due to softening and material nonlinearity may become large enough to invalidate the assumptions inherent to small strain theory. Analysis of the open-hole laminate also confirms a CDM approach based on small-strain increments and the Cauchy stress is insufficient to predict correct failure mechanisms. For example, fiber compression failure is triggered locally and limited interactions of the fiber splits with delamination are observed. The present analysis also shows that the inaccurate failure mechanisms are corrected by expressing the constitutive equations based on a Lagrangian kinematic measure, as implemented in the *CompDam* and *CDM-LD* models. Accounting for large deformation kinematics results in the prediction of fully developed ply splits, and allows for strong interaction with delaminations, resulting in a significant improvement in the prediction of the open-hole coupon internal failure mechanisms as shown by comparison to the experimental failure mode. From the insights gained in this study, it is recommended to base CDM models on a Lagrangian kinematic measure to improve their ability to predict ply splitting. Furthermore, the improvements in the numerical methodology may also help to analyse the matrix-dominated failure modes of thermoplastic composites welded joints as it is expected that their increased toughness and nonlinear behavior will promote larger deformations in the local failure mechanisms.

2.A CDM implementation 2D Puck failure criteria

The 2D Puck failure theory classifies lamina failure by Fiber Fracture (FF) and Inter-Fiber-Fracture (IFF), also referred to as fiber and matrix failure, respectively. Fiber failure represents failure in tension or compression due to loads parallel to the fiber axis (σ_1), while matrix failure is caused by transverse (σ_2) as well as shear loads (τ_{12}) and the interaction between them. The main idea of the Puck's theory, which is based on Mohr's fracture theory, is that the fracture limit of a material is determined by the stresses on the fracture plane. The predicted failure mode, follows from the plane with the least resistance. The Puck failure criteria is described by a stress exposure f_E which is defined as the ratio between the applied and failure stress vector. The R terms in the Puck failure criteria are strength parameters that describe the resistance of the action plane due to stress in the same direction. Many of these parameters can be mapped to the standard lamina stress allowables as given in Table 2.1: $R_\parallel^t = X_t$, $R_\parallel^c = X_t$, $R_\perp^t = Y_t$, $R_\perp^c = Y_c$, $R_{\perp\parallel} = S_{21}$. The 2D Puck failure theory, based on the mapped stress allowables, is defined as follows. The stress exposure for fiber failure $f_{E,FF}$ in tension and compression follows a simple maximum stress formulation:

If $\sigma_1 > 0$:

$$f_{E,FF} = \frac{\sigma_1}{X_t} \tag{2.8}$$

If $\sigma_1 < 0$:

$$f_{E,FF} = \frac{(-\sigma_1)}{X_c} \tag{2.9}$$

The failure envelope for matrix failure is shown in Figure 2.A.1 and consists of three different fracture modes. Failure due to matrix tension and/or in-plane shear is referred to as Mode A and results in a fracture plane angle θ equal to zero. The fracture angle remains at zero degree during moderate combined loading in shear and compression, identified as Mode B in in Figure 2.A.1. As compressive loads increase, the fracture plane angle increases up to 54 degree in pure compression. This final fracture mode is identified as Mode C.

The matrix failure envelop can be constructed in closed-form, however this requires the use material specific inclination (p) parameters. The recommended [51] parameters for CFRP/Epoxy are $p_{\perp\parallel}^{(+)} = 0.35$, $p_{\perp\parallel}^{(-)} = 0.3$, $p_{\perp\perp}^{(+)} = 0.275$. The transverse-transverse inclination parameter $p_{\perp\perp}^{(-)}$ is in the range of 0.25-0.30 but can also be obtained from

$$p_{\perp\perp}^{(-)} = p_{\perp\parallel}^{(-)} \frac{R_{\perp\perp}^A}{S_{21}} \tag{2.10}$$

where the fracture resistance $R_{\perp\perp}^A$ is defined as:

$$R_{\perp\perp}^A = \frac{S_{21}}{2p_{\perp\parallel}^{(-)}} \left(\sqrt{1 + 2p_{\perp\parallel}^{(-)} \frac{Y_c}{S_{21}}} - 1 \right) \tag{2.11}$$

The shear stress at the turning point of the fracture curve, τ_{21c}, is defined as:

$$\tau_{21c} = S_{21} \sqrt{1 + 2p_{\perp\perp}^{(-)}} \tag{2.12}$$
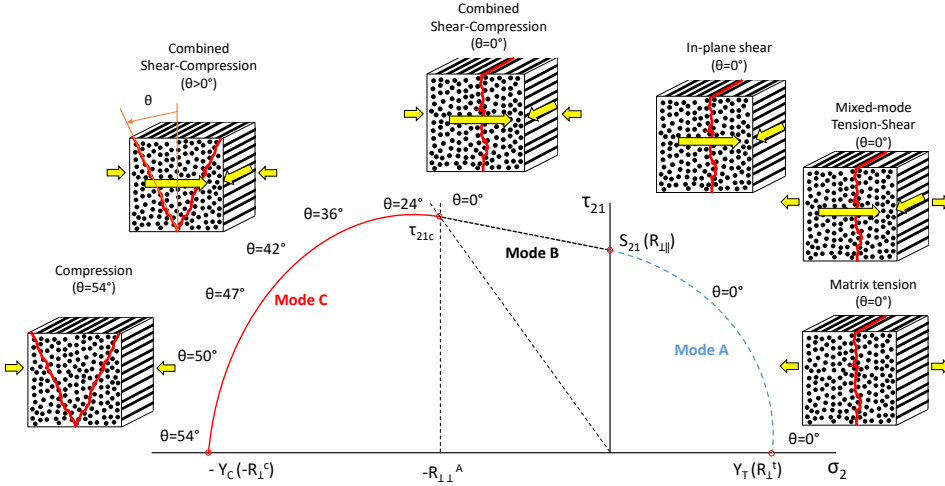
Figure 2.A.1: Puck failure criteria matrix failure modes, adapted from [51]

The stress exposure for matrix failure, $f_{E,IFF}$, for each fracture mode in is defined as:

Mode A: For $\sigma_2 \geq 0$:

$$f_{E,IFF} = \sqrt{\left(\frac{\tau_{12}}{S_{21}}\right)^2 + \left(1 - p_{\perp\parallel}^{(+)}\frac{Y_t}{S_{21}}\right)^2 \left(\frac{\sigma_2}{Y_t}\right)^2} + p_{\perp\parallel}^{(+)}\frac{\sigma_2}{S_{21}} \tag{2.13}$$

Mode B: For $\sigma_2 < 0$ and $0 \leq \left|\frac{\sigma_2}{\tau_{21}}\right| \leq \frac{R_{\perp\perp}^A}{|\tau_{21c}|}$:

$$f_{E,IFF} = \frac{1}{S_{21}}\left(\sqrt{\tau_{21}^2 + \left(p_{\perp\parallel}^{(-)}\sigma_2\right)^2} + p_{\perp\parallel}^{(-)}\sigma_2\right) \tag{2.14}$$

Mode C: For $\sigma_2 < 0$ and $0 \leq \left|\frac{\tau_{21}}{\sigma_2}\right| \leq \frac{|\tau_{21c}|}{R_{\perp\perp}^A}$:

$$f_{E,IFF} = \frac{Y_c}{(-\sigma_2)}\left(\left(\frac{\tau_{21}}{2\left(1 + p_{\perp\perp}^{(-)}\right)S_{21}}\right)^2 + \left(\frac{\sigma_2}{Y_c}\right)^2\right) \tag{2.15}$$

According to Mohr's hypothesis, the stress σ_1 does not have any influence on matrix failure as the action plane of σ_1 is perpendicular to the plane which is acted on by the stresses important for matrix failure. However, it is necessary to include a σ_1 in the matrix failure equations to weaken the matrix strength due to high fiber stresses [49, 51]. The reduction in matrix strength due to this effect is shown in Figure 2.A.2, where factors s and m control the amount of weakening due to fiber stresses. These factors can be fit on experimental data, where a value of $m = 1$ and $s = 0$ implies no effect of the parallel-to-fiber
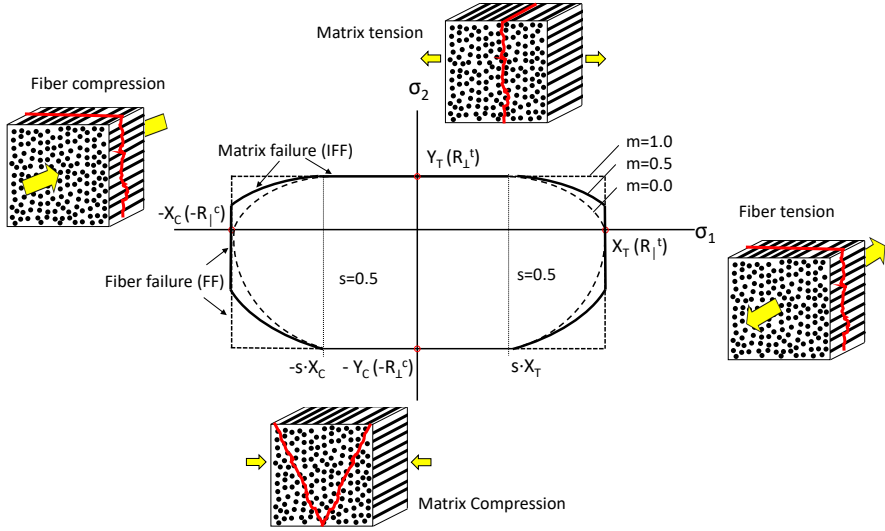
Figure 2.A.2: Influence of high fiber stress on matrix failure, adapted from [51]

stress on the matrix strength. The recommended [51] values of $m = 0.5$ and $s = 0.5$ are used in this study.

The final corrected matrix stress exposure, denoted as f_{E1}, can be calculated from the stress exposure without the influence f_{E0} and the weakening factor η_{w1} if $\frac{1}{s} \geq c \geq m$ following

$$f_{E1} = \frac{f_{E0}}{\eta_{w1}} \tag{2.16}$$

where

$$\eta_{w1} = \frac{c\left(a\sqrt{c^2\left(a^2 - s^2\right) + 1} + s\right)}{(ca)^2 + 1} \tag{2.17}$$

and c is a function of the fiber fracture stress exposure $f_{E,FF}$

$$c = \frac{f_{E0}}{f_{E,FF}}; a = \frac{1 - s}{\sqrt{1 - m^2}}; s = 0.5; m = 0.5 \tag{2.18}$$

After the onset of damage, damaging each ply is modelled by means of strain-softening laws. This is done through introducing a single scalar damage variable for each different physical failure mode ($d_{1\pm}, d_{2\pm}, d_6$) following the approach defined by [47]. The subscript 1 denotes failure in the fiber direction, and 2 denoted matrix failure. Distinction is made between tensile (+) and compressive (−) failure for the fiber and matrix failure modes to allow for differences in fracture toughness in each mode. Fiber failure ($d_{1\pm}$) is not influenced by matrix failure, thus the longitudinal stiffness is not reduced as a function of matrix

failure. However, shear damage (d_6) is coupled by both fiber and matrix failure [47] in damaging the stiffness matrix.

Softening laws are to ensure the physically correct dissipation of fracture energy for each failure mode. The exponential softening for matrix failure is expressed in equation 2.19.

$$d_M = 1 - \frac{1}{r_M} \exp\{A_M[1 - r_m]\}(M = 2\pm, 6) \tag{2.19}$$

where $r_M(M = 1\pm, 2\pm, 6)$ are model internal variables know as the elastic domain thresholds, which are initially 1.0 before the onset of damage and increase with effective stresses when failure initiates. The A-parameter in equation (2.19) is calculated to ensure that the computed dissipated energy is independent of mesh refinement [47]. The matrix damage variables are related to the Puck matrix failure modes follow the same validity as equation 2.13 to 2.15 :

Mode A: For $\sigma_2 \geq 0$:
$$d_2 = max(d_{2+}, d_{2-}) \tag{2.20}$$

Mode B: For $\sigma_2 < 0$ and $0 \leq |\frac{\sigma_2}{\tau_{21}}| \leq \frac{R_{\perp\perp}^A}{|\tau_{21c}|}$:
$$d_2 = d_{2-} \tag{2.21}$$

Mode C: For $\sigma_2 < 0$ and $0 \leq |\frac{\tau_{21}}{\sigma_2}| \leq \frac{|\tau_{21c}|}{R_{\perp\perp}^A}$:
$$d_2 = d_{2-} \tag{2.22}$$

Shear damage in each mode is directly related to matrix failure:
$$d_6 = d_2 \tag{2.23}$$

The damage and internal parameters are also used to allow for closure of transverse cracks under load reversal. Depending on the sign of the normal stress, a damage mode can be either activated or disabled. It is assumed that a tensile matrix crack (Mode A, Figure 2.A.1) can be closed in compression (Mode B, Figure 2.A.1), while shear cracks and cracks with fracture angles higher than 0° (Mode C, Figure 2.A.1) can not be closed. Frictional effects are not considered in the model.

Softening in fiber direction requires taking into account both fiber pull-out and bridging in order to predict size-effects for open-hole [60] and is implemented through a trilinear softening law following the CompDam implementation [44]. However, this is not described here as this study focuses on matrix dominated failure. The shear nonlinearity in the 1-2 plane is modelled using the Ramberg-Osgood equation based on the CompDam implementation [44]:

$$\gamma_{12} = \frac{\tau_{12} + \alpha_{pl} sign(\tau_{12})|\tau_{12}|^{\eta_{pl}}}{G_{12}} \tag{2.24}$$

where α_{pl} and η_{pl} can be obtained from fitting experimental in-plane shear tests. The response is assumed to be plastic until the onset of damage, after which the element is

damaged following an exponential softening law that is regularized according to the mode II fracture toughness. Nonlinear behavior in other directions are not considered.

The maximum element size for each failure mode is calculated according to the crack band model [53], where the characteristic element length is calculated for a material-aligned meshing strategy following the modeling approach defined in [16].

Finally, an element deletion strategy is implemented in order to avoid excessive element distortion which may significantly influence the run-times of the analysis or even crash it. These highly distorted elements generally show a sudden changes in volume which can be detected through the determinant of the deformation gradient $\det(\mathbf{F})$ [54]. The criteria for element deletion is adopted from [16], and is set to be more strict during very large deformations. For fiber failure, the elements are deleted once the damage variable becomes one. Summarizing, elements are deleted if they meet the following requirements:

$$
\begin{aligned}
d_{1\pm} &\geq 0.99999 \\
|\epsilon_i| &\geq 1.0 \, (i = 1, 2) \\
|\gamma_i| &\geq 1.0 \, (i = 12) \\
\det(\mathbf{F}) &\leq 0.4 \text{ or } \det(\mathbf{F}) \geq 4.0
\end{aligned}
\tag{2.25}
$$

3

Characterization and analysis of the interlaminar behavior of thermoplastic composites considering fiber bridging and R-curve effects

Thermoplastic composites can enable the development of new manufacturing techniques to make the aviation industry more sustainable while at the same time greatly benefit cost-efficient and high-volume production. One of the thermoplastic composite materials that can enable this transition is AS4/PEKK-FC. In this work, the interlaminar properties of AS4/PEKK-FC thermoplastic composite are characterized and analyzed by means of Mode I, II and Mixed Mode I/II at 50:50 tests, while considering fiber bridging and R-curve effects. In order to achieve stable crack propagation the test configurations are adjusted to account for the large fracture process zone ahead of the crack tip and an appropriate data reduction method is selected. The experimental data is reduced using an inverse methodology to extract cohesive laws based on only the load-displacement curves. Additionally, the use of this methodology provides new insights into the validity of two different mode II tests and the influence of fiber bridging on the mixed-mode interlaminar behavior. The interlaminar damage mechanisms are investigated by means of scanning electron microscopy. The resulting cohesive laws are implemented in commercial finite element software in tabular form, without the need for user-subroutines. All experimental test configurations are analyzed using a single material card and it is shown that fiber bridging and R-curve effects are well captured.

3.1 Introduction

There is a strong push in the aviation sector to move towards more sustainable and affordable aircraft structures. In order to meet these new requirements, it is inevitable that changes have to be made in the way aircraft structures are designed and manufactured. One of the materials that can facilitate this transition, is thermoplastic composite. Among many other benefits, the material offers improved mechanical properties, 'unlimited' shell life and also recyclability. Furthermore, thermoplastic composites also enable the use of new assembly techniques such as autoclave co-consolidation, out-of-autoclave and welding [9] which can greatly benefit cost-efficient and high-volume manufacturing. These new assembly techniques take advantage of the improved interlaminar mechanical properties compared to thermoset composites and can greatly reduce the amount of mechanical fasteners required. One of the most recent advancements that leverages this new technology, is the development of the next generation of thermoplastic composite aircraft fuselage [15]. This new fuselage design considers, among other materials, the fast-crystalizing Poly(Ether-Ketone-Ketone) thermoplastic polymer, also referred to as PEKK-FC [61]. In contrast to thermoplastic composites which have been studied in the past [43, 62–66], PEKK-FC composites offer faster processing times due to the increased rate of crystallization and can thus make a significant impact in how aircraft structures are designed and manufactured [67]. What makes PEKK unique among the other high performance polymers in the PAEK family, is the ability to synthesize isomeric copolymers to lower the melting temperature well below polymer degradation and significantly widen the melt processing window [68]. However, there is currently not much experimental understanding of the failure mechanisms of this material and the availability of accurate experimental data and validated testing or analysis techniques is rather limited [12, 61, 69–71]. Additionally, achieving predictable crack growth under both static and cyclic loading conditions is of high importance in aircraft design. It is expected that the superior mechanical performance of thermoplastic composites compared to thermoset composites may be attributed to effects such as plasticity and fiber-bridging. These effects are known [72, 73] to increase the size of the fracture process zone ahead of the crack-tip [74]. This large zone of damaged material makes it difficult to identify the exact position of the crack-tip, and thus makes the use of traditional experimental data reduction methods, which rely on accurately monitoring the crack-tip, rather difficult [75]. Furthermore, in the End Notched Flexure (ENF) and Mixed-Mode Bending (MMB) test, where only limited room for crack propagation is available, the large fracture process zone may reach the load-introduction point before stable crack growth can be achieved [74].

The use of cohesive zone models has become a popular methodology to accurately simulate delamination growth in composites [76]. This model describes the failure during delamination in terms of tractions and displacements of crack opening. The model reduces the stiffness of the cohesive zone once damage is initiated, thus decreasing the traction while respecting the amount of fracture energy that is dissipated. The shape of this softening behavior can be described by a cohesive law, which can have many different forms (e.g. linear, exponential, bilinear, trapezoidal, parabolic and multilinear) [77, 78], depending on the material behaviour. This can for example be achieved by superposition of cohesive elements [48] in order to capture specific failure modes such as fiber bridging [79, 80] or the influence of different ply interface angles [81]. However, this may not be so straight forward

for mixed-mode cohesive laws [82] and accurately following the load-displacement curve remains difficult if there is a strong R-curve effect that requires an accurate description of the cohesive law [79].

The aim of this work is to characterize and analyze the interlaminar behavior of thermoplastic composites during quasi-static loading, while considering fiber bridging and R-curve effects. This covers the whole process from experimental characterization, fractographic investigation, data reduction, numerical implementation and verification by numerical analysis in a commercial finite element software.

3.2 Methodology

An overview of the methodology is shown in Figure 3.2.1. First, the interlaminar fracture toughness is characterized in Mode I, II and Mixed Mode I/II at 50:50 on the Double Cantilever Beam (DCB) [83], End-Notched Flexure (ENF) [84], Calibrated End Loaded Split (CELS) [85] and Mixed-Mode Bending 50% (MMB50) [86] test configurations. The ENF and MMB50 test configurations are designed to achieve stable crack propagation, while accounting for the large fracture process zone of the thermoplastic material. Therefore, the validity of the mode II test method is investigated on both the ENF and CELS test and resulting interlaminar properties are compared.

The presence of the fracture process zone also influences the data reduction and analysis methodology. Consequently, both the traditional (Figure 3.2.1a) and a proposed methodology (Figure 3.2.1b) for experimental data reduction are considered. The traditional data reduction methods are based on the analytical Linear Elastic Fracture Mechanics (LEFM) solutions and require accurate measurement or estimation of the crack length. This results in an R-curve, which plots the calculated fracture toughness (G_c) against the crack length. The R-curve is however not a material property and depends on the test configuration, which means that the R-curve can not directly be used in finite element analysis. Therefore, typically only the initiation or propagation fracture toughness is used. This makes the analysis conservative for large cracks when initiation values are used and unconservative and inaccurate for small crack propagation when propagation values are used.
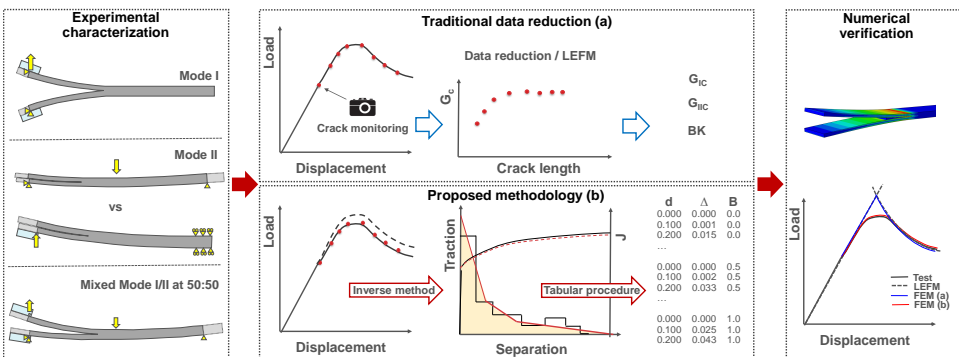
Figure 3.2.1: Overview of the methodology.

The proposed methodology (Figure 3.2.1b) makes use of an inverse data reduction method based on only the load-displacement curve [87, 88]. This method extracts a step-wise representation of the cohesive law, which needs to be processed before it can be reliably used in finite element software. This is achieved through the use of a new procedure, which can ensure an accurate description of the shape of the cohesive law in tabular format. The benefit is that the full R-curve effect can be accounted for and user-subroutines are no longer required. The data reduction technique also provides new insights into how fiber bridging affects the mixed-mode interlaminar behavior of thermoplastic composites. Finally, numerical analyses are performed for all test configurations to verify the derived interlaminar properties and analysis methodology.

3.2.1 Material properties

The thermoplastic composite used in this work is the Solvay APC(PEKK-FC) thermoplastic polymer prepreg [61]. The prepreg is reinforced with the continuous unidirectional AS4D fiber with a nominal ply thickness of 0.14 mm. The laminates are manufactured by means of autoclave consolidation, where a process cycle is used that is representative for large aeronautical parts. This means a constant phase of at least 45 minutes and a cooldown speed in the order of 5 °C/min. The full set of material properties are provided in [12] and the relevant properties that are used in the data reduction and analyses of this paper are summarized in Table 3.2.1. All values are valid at room temperature ambient conditions. The Young's modulus is given in both tensile and compressive direction. The values of the Matrix 0.2% and 0.5% offset shear strength are estimated by the nonlinear shear parameters and equations provided in [12].

Table 3.2.1: AS4D/PEKK-FC thermoplastic composite properties [12]

Property	Description	Value	Unit
E_{1t}	Young's modulus, longitudinal tensile direction	138300	MPa
E_{1c}	Young's modulus, longitudinal compressive direction	128000	MPa
E_{2t}	Young's modulus, transverse tensile direction	10400	MPa
E_{2c}	Young's modulus, transverse compressive direction	11500	MPa
$G_{12}=G_{13}$	Shear modulus	5190	MPa
v_{12}	Poisson ratio, 1-2 direction	0.316	-
v_{23}	Poisson ratio, 2-3 direction	0.487	-
Y_T	Matrix tensile strength	87	MPa
$S_{L_{0.2\%}}$	Matrix 0.2% offset shear strength (estimated)	50	MPa
$S_{L_{0.5\%}}$	Matrix 0.5% offset shear strength (estimated)	60	MPa
$S_{L_{5\%}}$	Matrix 5% offset shear strength	90	MPa

3.2.2 Specimen design

The specimen design is the same for all interlaminar tests and the specimens are machined from a single AS4D/PEKK-FC laminate that consists of 30 unidirectional 0-degree plies. The specimens are designed to be 25 mm wide and 225 mm long. The benefit of this specimen design with increased length is, that during the start of the test campaign, both the mode I and II fracture toughness can be tested on a single specimen. This can be helpful for characterization of materials of which the fracture properties are not yet known. Without

good estimations of the fracture properties, it may be difficult to set the correct initial crack length or span during these tests to achieve stable crack propagation. Furthermore, it also allows for some flexibility in testing higher toughness materials that may require a large span or clamping length during mode II and mixed-mode testing. However, for the actual propagation tests, it is recommended to only perform a small pre-crack to ensure that the crack front remains straight and without a fully developed fracture process zone. Due to the high processing temperature (377 °C, [61]) of thermoplastic composites, a 12.5 μm thick UPILEX foil is used as insert to start the crack. The length of this insert is 60 mm. The UPILEX foil is pre-treated with Frekote 700NC release agent to prevent contamination and allows for easy removal prior to testing. The benefit of this approach is that a single insert with a very small thickness can be used, thus guaranteeing a sharp as possible initial crack tip.

3.2.3 Mode I - Double Cantilever Beam test

The Double Cantilever Beam (DCB) test is performed to characterize the pure mode I fracture toughness at both the Delft University of Technology (TU Delft) and AMADE testing facilities of the University of Girona (UdG). The DCB tests at TU Delft follow the ASTM test standard [83] and loading blocks are bonded to load the specimens. In total, five tests are performed with an initial crack length of a_0 = 40 mm. The test configuration of the DCB test is shown in Figure 3.2.2a and the experimental setup at UdG is shown in Figure 3.2.2b. The DCB tests at UdG follow the ISO 15024 test standard [89] and the side-clamp beam [90] hinges are used to load the specimens, where the initial crack length is a_0 = 48 mm. As illustrated in Figure 3.2.2a, the load-application point on the loading-blocks effectively reduces the crack length from the insert size of 60 mm to a_0. In additions to the five propagation test at TU Delft, several pre-cracks and three propagation tests are performed at UdG. The crack length during these additional propagation tests is closely monitored using the system as shown in Figure 3.2.2b. A high resolution camera is used to monitor the crack length. Due to the limited field of view during close-up, a servo controlled system is used to follow the crack tip. The specimens are tested on a tensile testing machine, at a displacement rate of 1 mm/min. Rotation is measured by means of inclinometers. However, this data has not been used in the analysis and is not required for the proposed methodology. This also applies for all the other test configurations shown in this paper.

The Corrected Beam Theory (CBT) is used for the experimental data reduction method following the ISO 15024 test standard [89]. Following this method, the critical mode I energy rate G_{IC} is:

$$G_{IC} = \frac{3P\delta}{2b(a+\Delta)}\left(\frac{F}{N}\right) \tag{3.1}$$

where P and δ are the load and displacement, a is the total crack length during crack propagation and b is the specimen width. Furthermore, correction factors are used in the method, where F corrects for large displacement, N corrects for stiffening of the specimen by the loading blocks and Δ is a correction factor for crack tip rotation and deflection [89].

The experimental results are also compared to the analytical LEFM solution. For the Young's modulus E_{11} and E_{22}, the average of tension and compression from Table 3.2.1 is

Figure 3.2.2: DCB test setup at UdG AMADE lab: a) DCB test configuration and geometrical parameters; b) Test setup with camera and control system for crack monitoring.

used. The analytical solution uses the equations for the compliance C and the G_{Ic} [91], which can be re-rewritten to calculate the force P and displacement δ:

$$P = \sqrt{\frac{G_{Ic}b^2h^3E_{11}}{12(a+\chi h)^2}} \tag{3.2}$$

$$\delta = \frac{8P(a+\chi h)^3}{bh^3E_{11}} \tag{3.3}$$

The crack tip correction χ is derived in Eq. (3.4) as

$$\chi = \sqrt{\frac{E_{11}}{11G_{13}}\left\{3 - 2\left(\frac{\Gamma}{1+\Gamma}\right)^2\right\}} \tag{3.4}$$

where Γ is the transverse modulus correction parameter defined as

$$\Gamma = 1.18\frac{\sqrt{E_{11}E_{22}}}{G_{13}} \tag{3.5}$$

In the elastic domain the load is used as input and Eq. 3.3 to calculate the corresponding displacement for a given initial crack length a_0. During propagation the crack length a is gradually increased, for a known G_{Ic}, to calculate both the force and the displacement.

3.2.4 Mode II - End-Notched Flexure test

The End-Notched Flexure (ENF) test [92], consists of a three point bending setup of a specimen that is cracked on one of its ends. Nowadays this test is adapted to characterize the mode II interlaminar fracture toughness. The test is standardized in ASTM D7905 / D7905M [84] and is commonly used due to its simplicity. Figure 3.2.3a shows the ENF test configuration. The test setup at TU Delft including the camera to monitor the crack tip is shown in Figure 3.2.3b. Tests are performed in order to determine the test configuration that would provide stable crack propagation in mode II. The initial tests were performed using a span of $2L$ = 100 mm following the test standard. This made it difficult to achieve

stable crack propagation due to the large fracture process zone. To solve this, the test configuration is adjusted to $2L = 130$ mm. The different results and settings to mitigate the large fracture process zone are further discussed in section 3.3.2.
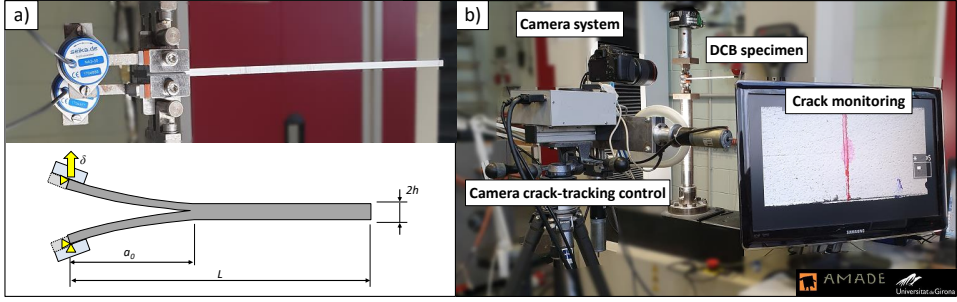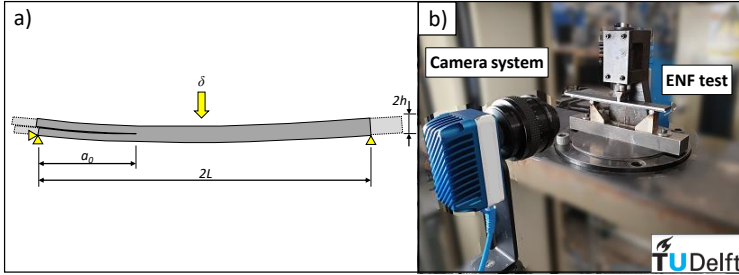

Figure 3.2.3: ENF test setup at TU Delft lab: a) ENF test configuration and geometrical parameters; b) Test setup with camera system for crack monitoring.

Most data reduction methods [84] depend on accurate measurements of the crack length during propagation. It is however difficult to measure this due to the development of a large fracture process zone ahead of the crack tip. The Compliance-Based Beam Method (CBBM) proposed by de Moura [75] can be used to avoid this. The measured initial compliance C_{0c} and initial crack length a_0 are used to obtain an apparent longitudinal modulus E_{1a}

$$E_{1a} = \frac{3a_0^3 + 2L^3}{8bh^3 C_{0c}} \tag{3.6}$$

Using the apparent modulus following [75] leads to

$$a_e = \left[\frac{C_c}{C_{0c}} a_0^3 + \left(\frac{C_c}{C_{0c}} - 1 \right) \frac{2L^3}{3} \right]^{\frac{1}{3}} \tag{3.7}$$

where C_c is the measured compliance. Further combining the equations from [75] results in the mode II fracture toughness G_{IIC}

$$G_{IIC} = \frac{9P^2 C_{0c}}{2b(3a_0^3 + 2L^3)} \left[\frac{C_c}{C_{0C}} a_0^3 + \left(\frac{C_c}{C_{0C}} - 1 \right) \frac{2L^3}{3} \right]^{\frac{2}{3}} \tag{3.8}$$

The experimental results are also compared to the analytical solution. In this case, the measured compliance is not available so a solution based on linear elastic fracture mechanics is followed. For this solution, the ENF load-displacement curve is divided into three parts. The load P is used as input for the first and third part and is gradually increased, while during crack propagation the crack length a is used as input to calculate both the load and the displacement. The crack length is corrected following [93], where χ is calculated from Eq. 3.4.
The load-displacement during the linear part is calculated by Eq. 3.9 and 3.10 using $a = a_0$. The second part during crack propagation if $a < L$:

$$P = \frac{\sqrt{G_{IIc}16b^2h^3E_{11}}}{9(a+0.42\chi h)^2} \tag{3.9}$$

$$\delta = P\frac{3(a+0.42\chi h)^3 + 2L^3}{8bh^3E_{11}} \tag{3.10}$$

and the third part where the crack has reached the load introduction if $a >= L$:

$$\delta = \frac{P}{2E_{11}bh^3}\left(2L^3 - \frac{(\frac{16}{3}G_{IIc}E_{11}b^2h^3)^{\frac{3}{2}}}{4\sqrt{3}P^3}\right) \tag{3.11}$$

3.2.5 Mode II - Calibrated End Loaded Split

The ENF test showed some difficulties due to the large fracture process zone of the thermoplastic material, therefore the material is also characterized using the Calibrated End Loaded Split (CELS) test method so that the results can be compared. The CELS specimen with the corresponding geometrical parameters is shown in Figure 3.2.4a and the test setup at the UdG lab is shown in Figure 3.2.4b. The CELS test is performed in a test rig specifically designed according to the ISO 15114:2014 [85] test standard. A loading block is bonded at the cracked end of the beam and an upward displacement is applied at the edge of the loading block. The other end of the beam is clamped, however this clamping is not fully constrained and allows for some sliding. The effect of the clamping system has to be calibrated so that an effective increase in beam length can be determined, as if the beam would be fully clamped. For this calibration procedure, the specimen is clamped and tested at several positions: $50, 60, 70, 80, 90$ and 100 mm. The crack propagation test is performed at a clamp length of 100 mm with an initial crack length of 56 mm. The crack length during propagation is measured using the same camera system as shown in Figure 3.2.2b.
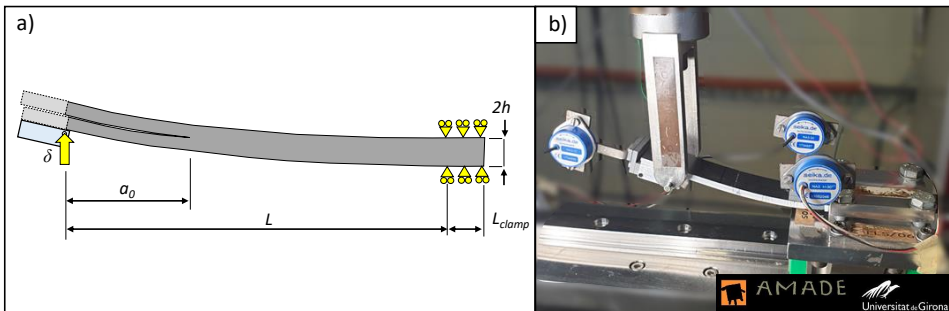

Figure 3.2.4: CELS test setup at UdG AMADE lab: a) CELS test configuration and geometrical parameters; b) Test fixture and specimen.

The experimental results are evaluated using the procedure according to the test method [85], where the compliance of the CELS specimen is given by:

$$C = \frac{\delta}{P} = \frac{3(a_e)^3 + (L + \Delta_{clamp})^3}{2bh^3 E_b} \tag{3.12}$$

where L, b and h are the span length, the width of the specimen and half of the specimen thickness, respectively. E_b is the apparent bending modulus and a_e is the effective calculated crack length. The Δ_{clamp} was introduced by Hashemi [91] to account for rotation and deflection at the clamp point. The parameters Δ_{clamp} and E_b are measured according to the compliance calibration described in the test standard [85]. The G_{IIC} fracture toughness is determined from

$$G_{IIC} = \frac{9P^2 a_e^2}{4b^2 h^3 E_b} \tag{3.13}$$

where the apparent crack length a_e is derived from equation (3.12) as

$$a_e = \left(\frac{1}{3} \left\{ 2bCh^3 E_b - (L + \Delta_{clamp})^3 \right\} \right)^{\frac{1}{3}} \tag{3.14}$$

The experimental results are also compared to the analytical solution. The equations that are used to predict the CELS test are based on the CBT solution where the crack length is corrected ($a = a + 0.42\chi h$) [93] and the beam length L is increased by the clamp correction factor Δ_{clamp}. This can also be estimated by $2\chi h$ (assuming $\chi_0 = \chi$) [93], however it was found that this underestimates the clamp correction by approximately 5 mm, which highly influences the analytical prediction. The displacement in the elastic part can be derived by gradually increasing the load and by using a_0 in Eq. 3.16. The load and displacement during propagation are calculated by increasing the crack length for a known G_{IIc} following:

$$P = \sqrt{\frac{G_{IIc} 4b^2 h^3 E_{11}}{9(a + 0.42\chi h)^2}} \tag{3.15}$$

$$\delta = \frac{P(3(a + 0.42\chi h)^3 + (L + \Delta_{clamp})^3)}{2bh^3 E_{11}} \tag{3.16}$$

3.2.6 Mixed-Mode Bending 50%

The Mixed-Mode Bending (MMB) test [65] is used to characterize the fracture toughness under mixed-mode loading conditions. This test has been standardized in the ASTM D6671/D6671M-19 [86]. The MMB specimen with the corresponding geometrical parameters is shown in figure 3.2.5a and the test setup at the UdG AMADE lab is shown in 3.2.5b. The same camera system as shown in Figure 3.2.2b is used to monitor the crack propagation. The mode mixity in this work is fixed to a ratio of 50% and only a single mode mixity is tested. The specimen has a pre-crack of length a_0 = 40 mm, which is pre-cracked for a few millimeter in mode I by means of the DCB test. Loading blocks are bonded to the specimen in order to clamp the bottom lever and load the upper lever as shown in figure 3.2.5. The span of the MMB50 test is set to $2L$ = 130 mm to prevent interaction of the center load introduction point with the fracture process zone as observed during the mode II ENF test. The length of the lever arm, c, is set to 54.4 mm. The force due to the weight of the rig (P_g) is 9.129 N and the center of gravity (c_g) for the 50% mixed-mode test is at 12.95 mm. The modulus, width and thickness of the metal calibration specimens are E_{cal} = 200 GPa,

b_{cal} = 25.4 mm and t_{cal} = 6.21 mm respectively. Following the test standard [86], this can then be used to calculate the system compliance and the bending stiffness of the laminate E_{1f}.
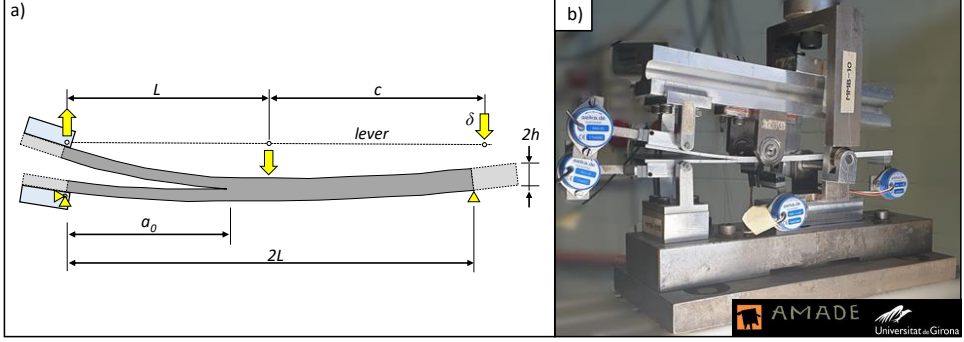
Figure 3.2.5: Mixed-mode bending 50% setup at UdG AMADE lab: a) MMB50 test configuration and geometrical parameters; b) MMB test fixture and specimen.

The mixed-mode fracture toughness is calculated by accounting for the weight of the test rig through Eq. (3.17) and (3.18), but the influence is found to be neglectable (1-2%) for the 50% mixed-mode test.

$$G_I = \frac{12[P(3c-L)+P_g(3c_g-L)]^2}{16b^2h^3L^2E_{1f}}(a+\chi h)^2 \tag{3.17}$$

$$G_{II} = \frac{9[P(c+L)+P_g(c_g+L)]^2}{16b^2h^3L^2E_{1f}}(a+0.42\chi h)^2 \tag{3.18}$$

The experimental load-displacement curves are also compared to the analytical solution. The load-displacement curve for mixed-mode bending can be predicted following the LEFM equations from [58] that follow the ASTM standard [86]. The load is obtained as:

$$P = \sqrt{\frac{G_c}{\frac{4(3c-L)^2(a+\chi h)^2+3(c+L)^2(a+0.42\chi h)^2}{64bL^2\frac{E_{11}bh^3}{12}}}} \tag{3.19}$$

The corresponding displacement is given as:

$$\delta = P\frac{4(3c-L)^2(a+\chi h)^3+(c+L)^2[3(a+0.42\chi h)^3+2L^3]}{96bL^2\frac{E_{11}bh^3}{12}} \tag{3.20}$$

The elastic relation before crack propagation is obtained by replacing the crack length a with the initial crack length a_0 in the previous equations.

3.2.7 Methodology for derivation of cohesive laws

The traditional data reduction methods, as described in the previous sections, rely on accurate measurement or estimation of the crack length and do not provide sufficient information to account for fiber bridging or R-curve effects in the numerical analysis. These effects can be accounted for through the cohesive law. From literature it is known that different damage mechanisms can be represented by a different shape of the cohesive law. Three examples of typical shapes for cohesive laws are shown in Figure 3.2.6. Figure 3.2.6a shows linear softening with is typically used by default when only the fracture toughness of the material is known. The trapezoidal shape as shown in Figure 3.2.6b can be used to represent the influence of plasticity as demonstrated by Tvergaard and Hutchinson [94], where the total energy can be divided into multiple parts (G_1, G_2) to represent both plasticity and damage. Instead, different damage mechanisms may also be represented by superposition of linear cohesive laws to account for R-curve effects as shown in Figure 3.2.6c based on the approach of Dávila et al. [48]. Dávila et al. [48] used this bilinear shape to distinguish between fiber pull-out and breakage during translaminar failure [95], while a bilinear shape with a longer tail has been used to represent fiber bridging [79]. However, these simplified cohesive laws are generally not accurate enough to follow the full R-curve effect and corresponding nonlinearity observed in the load-displacement curve [79]. The proposed methodology, as shown in Figure 3.2.1, can include the full R-curve
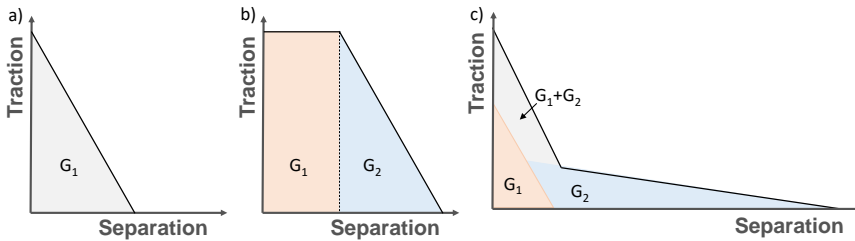
Figure 3.2.6: Different shapes of cohesive laws used in numerical analysis to represent different damage mechanisms: a) linear, b) trapezoidal; c) bilinear.

effect and makes use of the inverse method presented by Abdel Monsef et al. [87, 88] to determine the experimental J-curve and cohesive law. The inverse method minimizes the error between the experimental and the numerical load-displacement curves by adjusting the cohesive law parameters. Figure 3.2.7 schematically shows the procedure to extract the cohesive law where the experimental load-displacement curve is the input and the output is an experimental J-curve and multilinear cohesive law "staircase type", also referred to as the experimental cohesive law in this paper. It should be noted that the method predicts only the shape of the cohesive law. This information may be used to reason that a specific damage mechanisms is responsible, study variation in cohesive laws between multiple tests, or gain insight in how the shape may change for different configurations or environmental conditions, as the methodology does not require visual tracking of the crack tip [96].
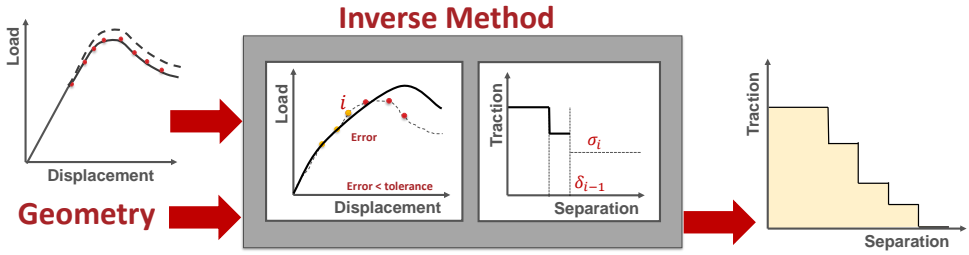
Figure 3.2.7: Inverse methodology for derivation of cohesive laws, overview of methodology from [87, 88].

3.2.8 PROCEDURE FOR USER-DEFINED TABULAR COHESIVE LAWS

The next step in the proposed methodology (Figure 3.2.1b) is to process the experimental cohesive law for use in the numerical analysis, referred to as the numerical cohesive law. The cohesive law has to be defined by the initial elastic response of the cohesive element, the damage initiation criteria and the damage evolution. A typical traction-separation law with linear softening is shown in Figure 3.2.8a. The initial elastic response of the element is related to the initial slope of the traction-separation curve, which can be related to the Young's modulus of the material when a finite thickness is used, for example for adhesives. For the analysis of delaminations, which are modelled as a zero-thickness interface, this property is referred to as the penalty stiffness (K in Figure 3.2.8a). The damage initiation is
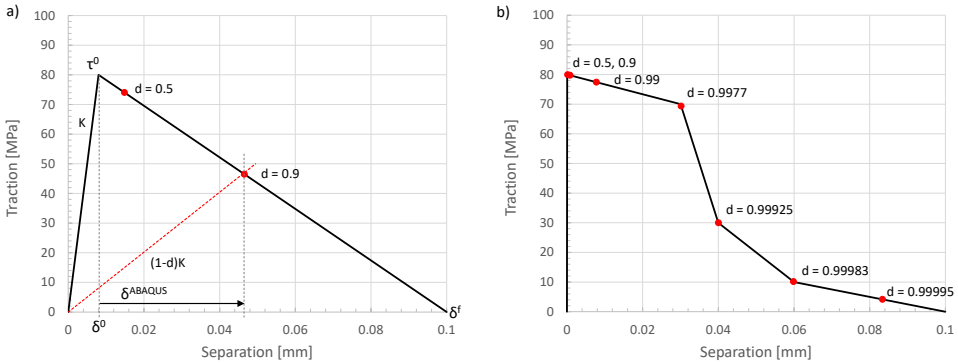
Figure 3.2.8: Comparisons of two cohesive laws: (a) low penalty stiffness cohesive law with linear softening; (b) high penalty stiffness user-defined cohesive law.

defined as the peak traction for each loading mode by using a failure criterion, for example the max-stress criterion (MAXS). Damage evolution is provided in tabular format and requires the relation of the separation after damage initiation to the damage variable and the loading mode. The damage variable, d, is defined as the reduction of the effective traction due to damage as

$$d = 1 - \frac{\tau}{K \cdot \delta} \tag{3.21}$$

where τ is the traction at a material point, K is the initial elastic stiffness and δ is the total separation defined as $\delta = \delta^0 + \delta^{ABAQUS}$, as illustrated in Figure 3.2.8a. δ^0 is the separation at onset of damage and δ^{ABAQUS} the input displacement for the tabular format in Abaqus. The loading mode, B, is defined as the ratio between pure mode I (defined as 0) and pure mode II (defined as 1), and has to be defined for each cohesive law that results from the mixed-mode tests.

It is however difficult to achieve an accurate solution for detailed cohesive laws when using a high penalty stiffness or when a sudden change in the shape of the cohesive law are introduced. When a low penalty stiffness is used, the damage variable gradually increases until full separation is achieved as shown in Figure 3.2.8a. However, when using a high-penalty stiffness, as shown in Figure 3.2.8b, there is rapid increase in the damage variable for small separation until the element is nearly fully damaged ($d = 0.99$). This is followed by a rapid increase in displacement until the element is fully damaged, which means high accuracy is required in both damage and displacement. If sudden changes or complex shapes are introduced in the cohesive law, it becomes even more difficult to manually define accurate input data. When using a high penalty stiffness, for example
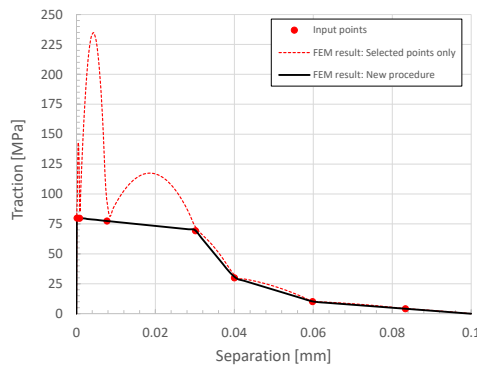
Figure 3.2.9: Single element FEM result to verify tabular cohesive law.

$K = 10^6$ N/mm^3, which is typically used for simulation of delaminations, another difficulty arises. It appears that Abaqus uses a higher-order interpolation function for cohesive laws in tabular format, which may cause spurious oscillations if insufficient data points are defined. A simulation of a single cohesive element that highlights this issue is shown in Figure 3.2.9 on the same cohesive law as presented in Figure 3.2.8b. When using only the selected points in the tabular cohesive law, defined as "Input points" in Figure 3.2.9, spurious behavior is observed. In order to solve this, a procedure is developed that will guarantee an accurate description of the tabular cohesive law.

The flow diagram of this procedure is shown in Figure 3.2.10. The input for the methodology is the shape of the cohesive law which should contain each line segment. The experimental cohesive law first needs to be simplified or cleaned to ensure the J-curve and damage variable monotonically increase. This means that typically only small adjustments are required to directly use the shape of the experimental cohesive law. However, it was found that a more smooth shape helps convergence as it reduces sudden changes in stiffness. During this calibration process it is important to ensure a close correlation with the experimental J-curve, to guarantee that the same amount of energy is dissipated at each segment of opening displacement. In order to adjust the desired accuracy of
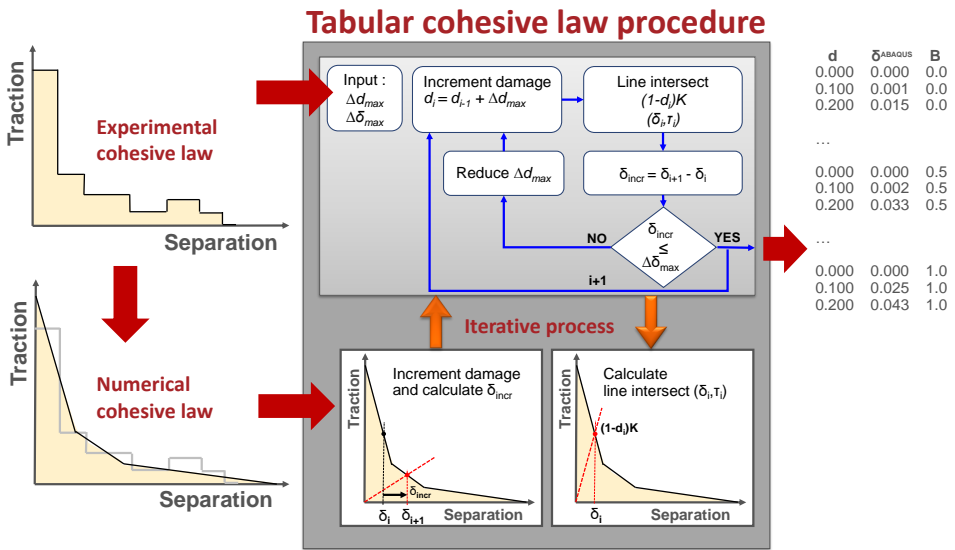
Figure 3.2.10: Procedure for user-defined tabular cohesive law

the tabular procedure, a constraint to the maximum increase in damage variable $\triangle d_{max}$ and displacement $\triangle \delta_{max}$ is introduced. The damage variable is gradually increased from 0 to 1 by using the maximum damage variable as a step size, and will thus influence the table size. The resulting penalty stiffness is then calculated from Eq. (3.21) and is used to calculate the line-segment intersection of the cohesive law. The displacement at onset of damage ($\delta^0 = \tau^0/K$) is then subtracted for the displacement at the increment (δ_i) of the line-segment intersection in order to calculate the delta displacement. This increase in displacement (δ_{incr}) is checked against the constraint. If this criteria is not met, the increase in damage variable is reduced and the procedure is repeated until the criteria is met. This value is then saved in tabular format and the damage is further increased. This is repeated for each cohesive law and loading mode. The FEM result to verify the procedure on the high-penalty stiffness cohesive law is shown in Figure 3.2.9 by comparing the input points to the resulting cohesive law. This demonstrates that the cohesive behavior can be accurately simulated using the tabular approach.

3.3 Experimental results

The experimental results for each test are presented and evaluated using the two data reduction approaches. The load-displacement curves are compared to the analytical solution for each test and the R-curves are presented. Furthermore, the experimental J-curves and cohesive laws are processed for the numerical analysis and compared against the experimental curves.

3.3.1 Mode I - Double Cantilever Beam

All the mode I experimental results including pre-cracking are shown in Figure 3.3.1. As can be observed in the figure, DCB with different initial crack lengths are performed and also several pre-crack tests are performed. One typical test is selected for data reduction in the next section. The relation of this specific test to the other tests is then further investigated and discussed. The load-displacement curve of the selected test is compared
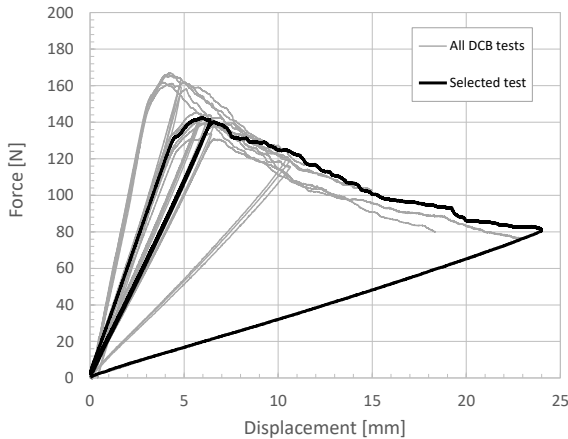
Figure 3.3.1: DCB test results, selected test for initial evaluation highlighted.

to the analytical solution in Figure 3.3.2a and the corresponding R-curve is shown in Figure 3.3.2b. The load-displacement curve consists of a pre-crack and a propagation part, which were tested separately and they are compared to the analytical solution using a_0 = 48 mm and G_{Ic} = 1.12 kJ/m^2. The first marker on the curve indicates the 'NL point' (first deviation from linear portion of curve) and all other points represent visible observations of crack growth and are indicated as 'PROP'. The same points are plotted in the R-curve with their corresponding calculated fracture toughness from the data reduction method. The initiation fracture toughness is approximately 0.7 kJ/m^2 and the propagation fracture toughness 1.12 kJ/m^2. The resulting experimental J-curve and cohesive law that are determined using the inverse method are shown in Figure 3.3.3a and b, respectively. For reference, the processed numerical J-curve and cohesive law which will be used as input for the numerical analysis are also given.
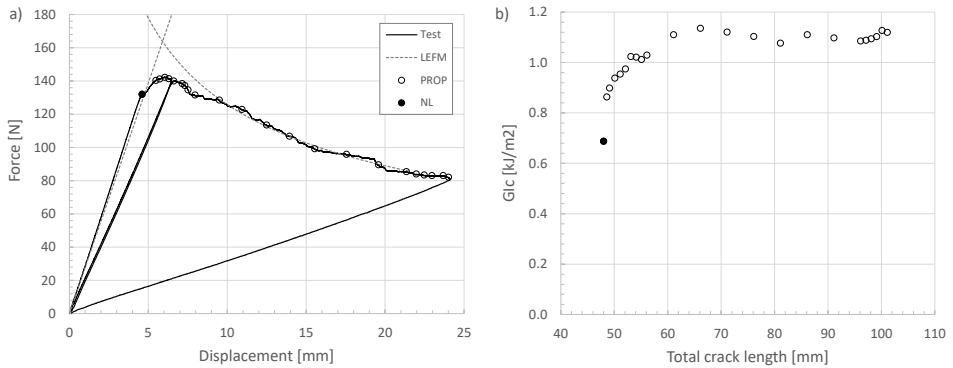
Figure 3.3.2: DCB test result: a) Load-displacement vs analytical solution (LEFM), nonlinear (NL) and crack propagation points (PROP); b) R-curve with propagation points.
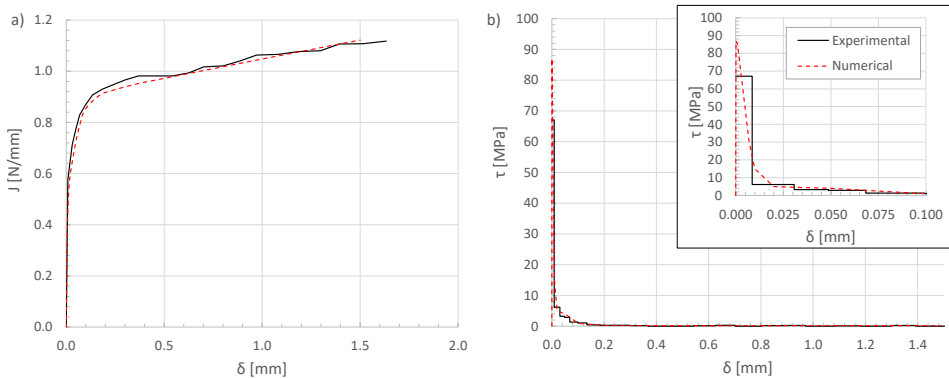
Figure 3.3.3: DCB data reduction, experimental and numerical curves: a) J-curve; b) Cohesive law.

When taking a closer look at Figure 3.3.3a it is found that the experimental results show a plateau in the J-curve and an increase in fracture toughness at a crack opening larger than 0.5 mm. In the cohesive law of Figure 3.3.3b, this effect is visible as the long tail, while most of the energy dissipates at the start of the cohesive law. This effect can also be observed experimentally as shown in Figure 3.3.4a. The experiment shows large scale fiber bridging and many broken fibers on the fracture surface. The fracture surface is also investigated by means of Scanning Electron Microscopy (SEM) at UdG. This is shown in Figure 3.3.4b with a magnification of 300x, and shows pull-out of large fiber bundles on the fracture surface. A close-up using 1000x magnification in Figure 3.3.4c of a fiber bundle highlights extensive polymer drawing out in the plane normal to the fiber direction and a large presence of polymer material on the fibers.

The influence of fiber bridging is investigated further by comparing several DCB tests. This comparison is shown in Figure 3.3.5a and all tests show a consistent initiation fracture toughness of approximately 0.7 kJ/m^2, independent of initial crack length. However, the second test (Figure 3.3.5a, DCB 2) achieves a propagation fracture toughness of approximately
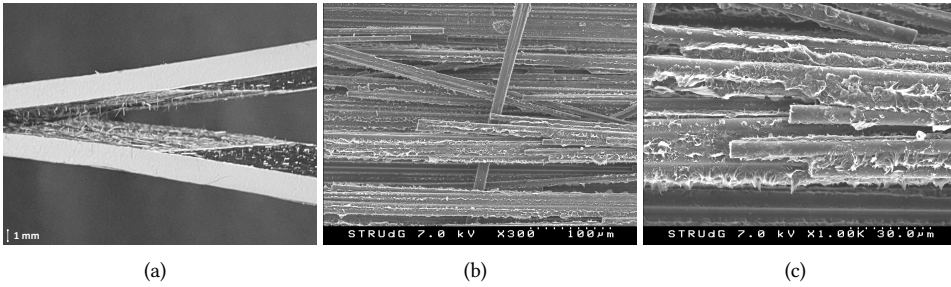
Figure 3.3.4: Experimental evidence of fiber bridging: a) Fiber bridging and broken fibers during DCB test; b) SEM fracture surface showing pull-out of large fiber bundles; c) SEM close-up on fiber bundle.

0.95 kJ/m^2, which may suggest a smaller influence of fiber bridging. This is confirmed by comparing the experimental J-curves and cohesive laws. This comparison is shown in Figure 3.3.5b, where the scale of the experimental cohesive law is adjusted to zoom in on the tail. It is shown that, as the opening displacement increases, the propagation fracture toughness of the first test increases to approximately 1.12 kJ/m^2 (I). This increase in energy can also be observed in the experimental cohesive law, which makes it apparent that energy is being dissipated due to fiber bridging (II). However, this is not the case for the second test, which reaches a plateau in the J-curve and no dissipation of fracture energy is observed in the tail of the cohesive law (III).
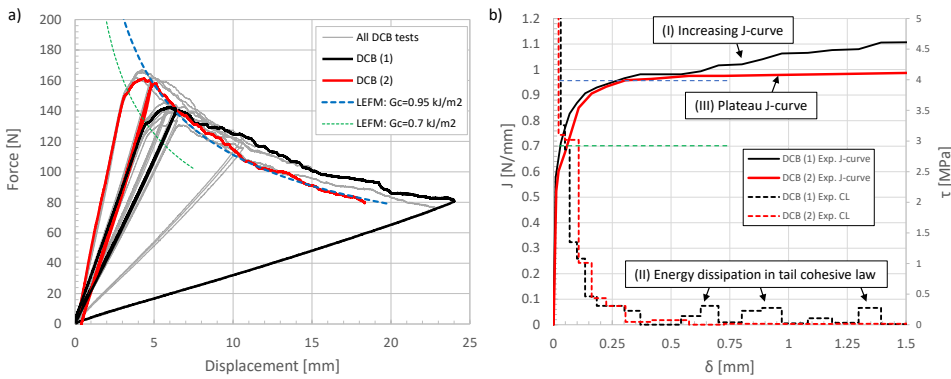
Figure 3.3.5: Fiber bridging influence on Mode I: a) DCB tests with two selected results and comparison against analytical solution of Gc = 0.7 kJ/m^2 and 0.95 kJ/m^2; b) Corresponding J-curve and cohesive law for both tests with identification of initiation and fiber bridging Gc.

The plateau in the J-curve of Figure 3.3.5b suggests that scatter in the propagation fracture toughness may be mostly influenced by the amount of fiber bridging, and that fiber bridging may not play an important role for small cracks (< 0.5 mm opening displacement). The proposed methodology could be used to further investigate scatter in the interlaminar properties and establish a lower, mean and upper-bound J-curve. The J-curve can then be used to treat variation in different parts of the cohesive law separately. This insight

may be used to support studies on uncertainty quantification related to variability of the interlaminar behavior. It should also be noted that discarding the pre-crack part of the load-displacement curve and using only the propagation value in the numerical analysis would be unconservative for small cracks.

3.3.2 MODE II - END-NOTCHED FLEXURE

The interlaminar properties for mode II are characterized by means of the End-Notched Flexure (ENF) test. The result of three ENF tests are shown in Figure 3.3.6 and are compared against the analytical solution. The first (1) two tests are performed following the test standard with a span of 100 mm and initial crack length of a_0 = 40 mm. Very little stable crack propagation is measured because of the large fracture process zone that interacts with the load introduction point. Significant shear deformation is observed over a large area. However, the exact size is difficult to determine which support the choice of using an effective crack length during the data reduction instead. Interaction with the load introduction point is also well predicted by the third part of the analytical solution of the ENF test in Equation (3.11). In order to mitigate this issue, the test setup is adjusted (2) to a_0 = 45 mm and span of $2L$ = 130 mm. The specimens are pre-cracked in mode I prior to testing. For both configurations a good correlation with the analytical solution is found.
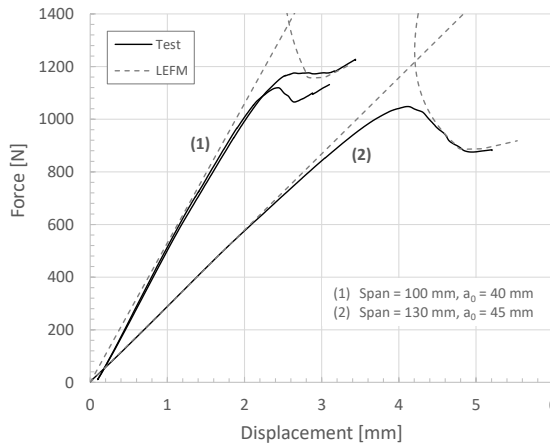
Figure 3.3.6: ENF experimental results versus analytical solution.

This highlights that it is difficult to achieve stable crack propagation with the ENF tests for materials that develop a large fracture process zone such as thermoplastic composites. In literature, a value of $a/L > 0.7$ is typically suggested [43] to achieve stable crack propagation. While testing at a small a/L ratio results in unstable crack growth [97]. The downside to a too large a/L is that it reduces the available room to develop the fracture process zone before achieving stable crack propagation ($L - a$). During the first test in Figure 3.3.6, the configuration was a/L = 0.8 and $L - a$ = 10 mm which is found to be insufficient. The configuration of the second test was a/L = 0.7 and $L - a$ = 20 mm and worked well, thus achieving a full development of the fracture process zone. The lower bound related to

unstable crack propagation is not investigated, but it is likely that configurations in the range of 0.65 < a/L < 0.75 would provide good results for this material system.

The load-displacement of the ENF test is compared in Figure 3.3.7a against the analytical solution (a_0 = 45 mm and $span$ = 130 mm) for G_{IIc} = 2.35 kJ/m². The initiation fracture toughness appears to be rather low and similar to the mode I initiation value. This is shown in the R-curve of Figure 3.3.7b for both the DBT [75] and CBBM data reduction method from equation (3.8).

Figure 3.3.7: ENF test result: a) Load-displacement vs analytical (LEFM), nonlinear (NL) and crack propagation points (PROP); b) R-curve with propagation points for both the DBT and CBBM data reduction method.
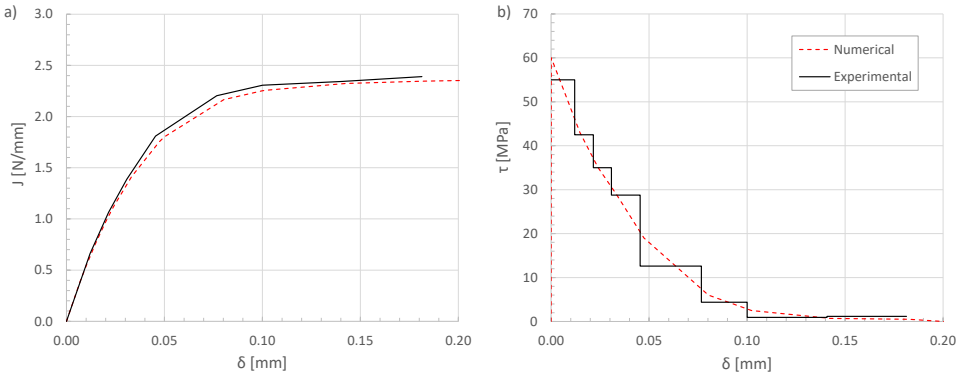
Figure 3.3.8: ENF data reduction, experimental and numerical curves: a) J-curve; b) Cohesive law.

The calculated crack length from the CBBM method results in a different crack length compared to what is visually observed. However, the propagation fracture toughness is nearly identical, with the benefit that no visual observation of crack propagation is required when using the effective crack length method. The resulting experimental J-curve and cohesive law are shown in Figure 3.3.8a and b, respectively. For reference, the processed numerical J-curve and cohesive law which are then used as input for the numerical analysis are also given.

3.3.3 Mode II - Calibrated End Loaded Split

The interlaminar properties for mode II are also characterized by means of the Calibrated End Loaded Split (CELS) test. Experimental results for the three CELS tests are shown in Figure 3.3.10a. The tests are performed at a clamp length of 100 mm. The load-displacement of one CELS test is highlighted in Figure 3.3.10a and compared against the analytical LEFM solution. From the calibration, a clamp correction of 13.64 mm and a bending modulus of 134 GPa is calculated. The compliance, C, of the individual tests at different clamp lengths is plotted in Figure 3.3.9 using $C^{1/3}$ to calculate Δ_{clamp} at the intercept of the regression line.
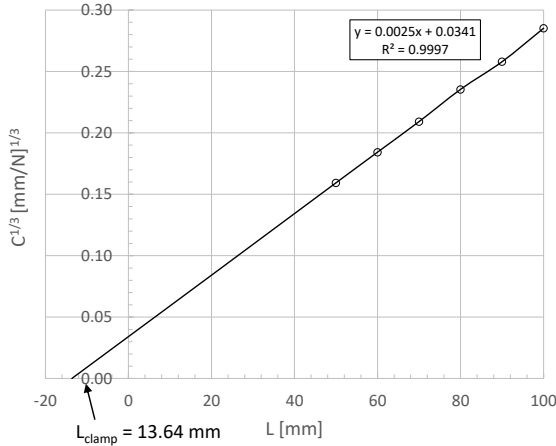
Figure 3.3.9: CELS test calibration results and calculated clamp correction L_{clamp}

The R-curve using both the visual and effective crack length is shown in Figure 3.3.10b. The effective crack length method results in a significantly higher crack length and fracture toughness compared to using the visual crack length in equation 3.13. The propagation fracture toughness of the effective crack data reduction method shows a good correlation with the LEFM solution from equation 3.15 and 3.16, and accounts for both the crack tip and clamp correction.

The resulting experimental J-curve and cohesive law are shown in Figure 3.3.11a and b, respectively. The calculated fracture toughness based on the effective crack length shows a good match with LEFM (G_{IIc} = 2.35 kJ/m^2). The experimental J-curve and cohesive law are determined using a total length including clamp correction of $L + \Delta_{clamp}$ = 113.6 mm in the inverse method. It is observed that at an opening displacement of 0.15 mm the J-curve reaches a plateau around J = 2.35 N/mm and the cohesive law approaches zero. After some more crack opening the energy further increases. This effect is also visible on the load-displacement and R-curve and is consistent with the data reduction method based on the effective crack length in terms of fracture energy. For reference, the processed numerical J-curve and cohesive law from the ENF test (Figure 3.3.8) are also given and it shows that they are nearly identical. This demonstrates that the J-curve is independent of the test configuration and consistent behavior between the two tests is found, even though the tests are performed at different test facilities.
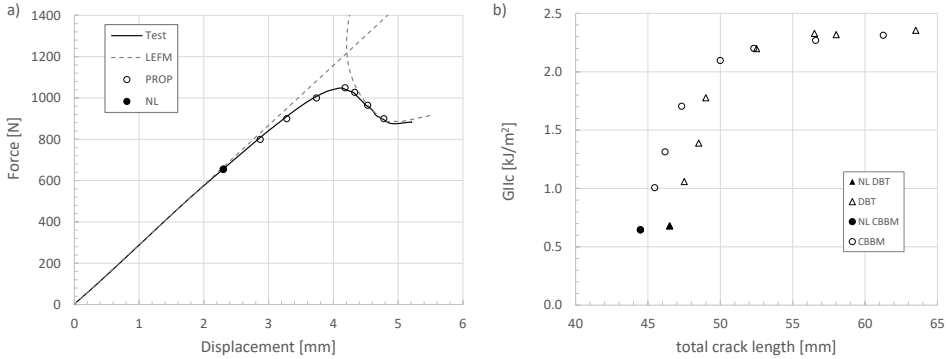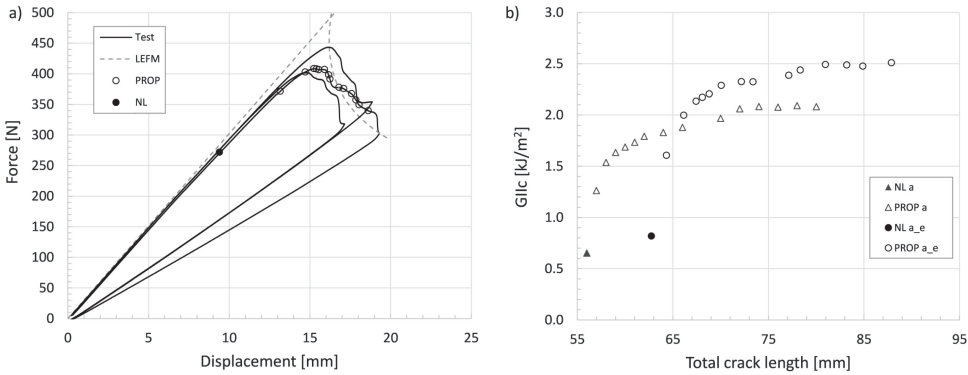
Figure 3.3.10: CELS test result: a) Load-displacement vs analytical (LEFM), nonlinear (NL) crack propagation points (PROP); b) R-curve with propagation points using visual (PROP a) and effective crack length (PROP a_e) with clamp correction.
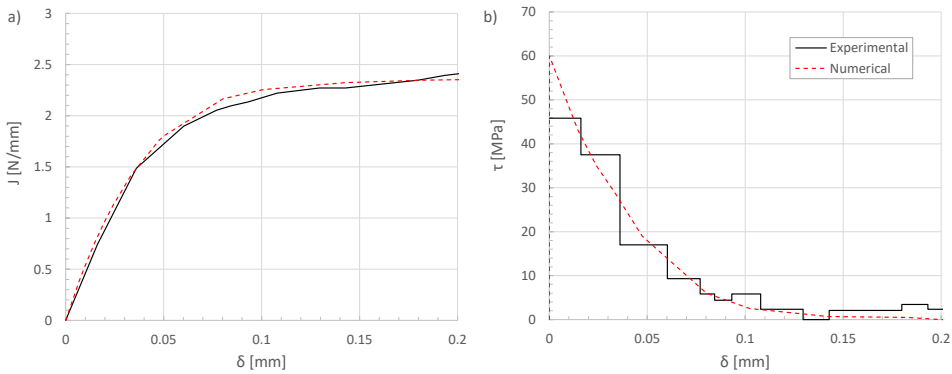
Figure 3.3.11: CELS data reduction, experimental and numerical curves: a) J-curve; b) Cohesive law.

3.3.4 Mixed-mode bending 50%

The interlaminar properties for mixed-mode behavior are characterized by means of the Mixed-Mode Bending (MMB) test. The load-displacement curves of three MMB tests at 50% mode I-II are shown in Figure 3.3.12a. The load-displacement curve of one of the MMB50 tests is compared against the analytical LEFM solution using a initial crack length of $a_0 = 40$ mm, $G_{Ic} = 1.12$ kJ/m^2, $G_{IIc} = 2.35$ kJ/m^2 and a BK-coefficient [57] of 2.9, which results in a mixed-mode fracture toughness of 1.27 kJ/m^2. This comparison is shown in Figure 3.3.12a, which matches well with the R-curve presented in Figure 3.3.12b. It is observed in the R-curve that after some crack propagation, the calculated fracture toughness reduces, which may be caused by interaction of the fracture process zone with the load-introduction or changes in mode-mixity during crack propagation.
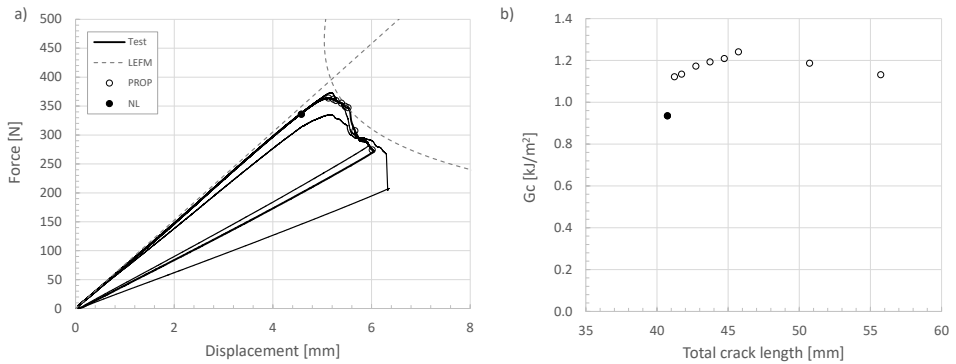
Figure 3.3.12: Mixed-mode bending 50% test result: a) Load-displacement vs analytical (LEFM), nonlinear (NL) crack propagation points (PROP); b) R-curve with propagation points.

3.3.5 Fractographic investigation

A fractographic investigation using SEM is performed to provide insight into the interlaminar damage mechanisms during Mode I, Mixed Mode I/II at 50:50 and Mode II loading conditions. The SEM micrographs at different magnifications for each loading mode are presented in Figure 3.3.13. Experimental evidence of fiber bridging by means of SEM micrographs is already presented in Figure 3.3.4. The Mode I fracture surface of a matrix rich location is shown in Figure 3.3.13a and b. Extensive polymer drawing out in the plane normal to the fiber direction is observed. At several locations this occurred in circular patterns and signs of plastic deformation are present. The circular pattern in the fracture surface, and signs of patterns in the fiber beds, may suggest a relation of the matrix-dominated failure mode with the crystallization kinetics of the thermoplastic polymer matrix as they appear to be similar is size [98]. During loading in Mixed Mode I/II at 50:50 the presence of plastic deformation is even more pronounced and occurs at an angle to the fiber direction as shown in Figure 3.3.13c and d. The change in angle is further confirmed by the CELS Mode II fracture surface as shown in Figure 3.3.13e and f, which features polymer drawing out and extensive plastic deformation in the plane of the delamination. The SEM micrographs confirm the absence of fiber bridging in Mixed Mode I/II at 50:50 and Mode II loading conditions. These observations are in line with Carlsson et al. [43] who compared the fracture surface in mode I and II of epoxy matrix and PEEK thermoplastic matrix composites, and found very brittle behavior showing bare fibers and a small degree of polymer deformation for the epoxy matrix composites in mode I, and extensive hackling in mode II. The presence of plastic deformation in both his and the present work confirms that energy dissipation due to plastic deformation plays an important role in the interlaminar fracture behavior.
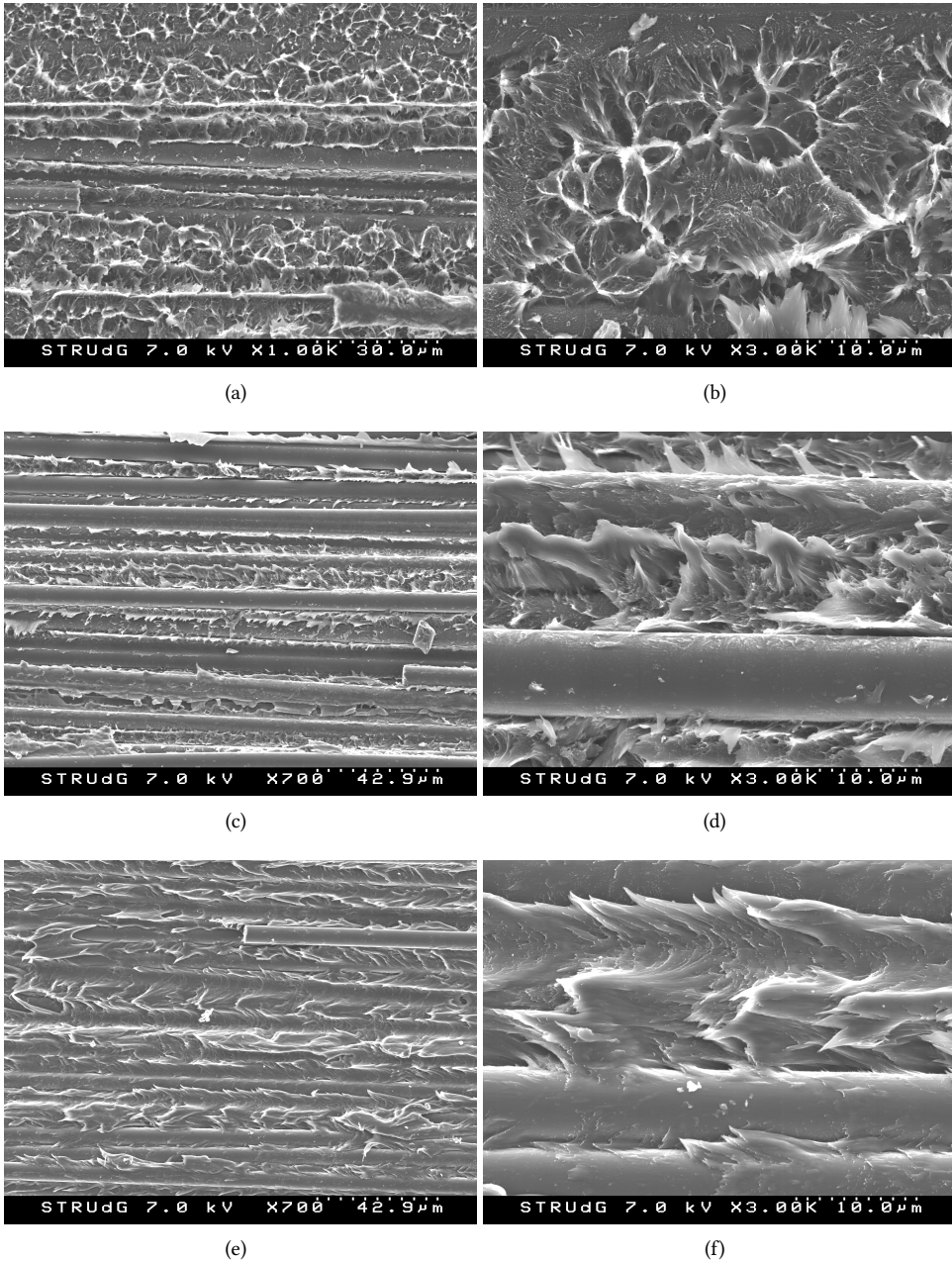
Figure 3.3.13: SEM micrographs of fracture surface at different magnifications: a) Mode I 1000x; b) Mode I 3000x; c) Mixed Mode I/II at 50:50 700x; d) Mixed Mode I/II at 50:50 3000x; e) CELS Mode II 700x; f) CELS Mode II 3000x.

3.4 Analysis and discussion

Numerical analyses of the Double Cantilever Beam (DCB), End-Notched Flexure (ENF), Calibrated End Loaded Split (CELS) and Mixed-Mode Bending 50% (MMB50) tests have been simulated by using the commercially available finite element software ABAQUS/Standard. The result of both data reduction approaches as defined in Figure 3.2.1 are simulated in order to verify the derived interlaminar behavior and analysis methodology. The specimens are modelled by using two-dimensional plane strain elements (CPE4I) for the composite laminate and COH2D4 cohesive elements for the interface. A fine mesh of 0.1 mm is used to ensure that sufficient elements are within the fracture process zone [99]. The rolling conditions of the CELS test are not modelled, instead the beam length is increased by the clamp correction length and fixed. The values for the relevant geometric parameters that are used in the numerical analysis are summarized in Table 3.4.1 and the geometry follows the configurations as specified in Section 3.2.

Table 3.4.1: Summary of geometric parameters used in the numerical analysis.

Test	W [mm]	$2h$ [mm]	a_0 [mm]	L [mm]	L_{clamp} [mm]	c [mm]
DCB	25	4.2	40 / 48	100	-	-
ENF	25	4.2	40	65	-	-
CELS	25	4.2	56	100	13.64	-
MMB50	25	4.2	40	65	-	54.4

The elastic material properties that are used in the analysis are specified in Table 3.2.1. For the Young's modulus E_{11} and E_{22}, the average of tension and compression is used. The initiation strength values of the numerical cohesive laws are based on the prediction from the experimental cohesive laws and are aligned to the strength values reported in [12]. Therefore, the mode I initiation strength is set equal to the matrix tensile strength Y_T of 87 MPa. However, the mode II initiation strength is not set equal to the matrix 5% offset shear strength S_L. Damage initiation in mode II occurs at a much smaller shear strain [100], therefore the mode II initiation strength value is set to the 0.5% offset shear strength of approximately 60 MPa. The value is estimated from the nonlinear parameters and equations in [12]. For the penalty stiffness of the interface, a value of $K = 10^6$ N/mm^3 is used. Considering the amount of plastic deformation on the fracture surface in Figure 3.3.13, and predicted initiation strength by the inverse method in the range of 45-60 MPa, it becomes apparent that a large portion of the fracture energy at the start of the cohesive law is likely due to plastic deformation. Depending on the choice of shear initiation strength, this would results in either an exponential or trapezoidal shape of the cohesive law. In the current work, an exponential shape is assumed. It is also expected that constraining effects of different fiber orientations on plasticity may need to be considered. However, this is not included in the present study. In Section 3.3.1 it is shown that fiber bridging has a significant influence on the mode I fracture toughness. It is concluded that the propagation fracture toughness without the influence of fiber bridging is approximately 0.95 kJ/m² and no clear signs of fiber bridging are observed during evaluation of the mode II and mixed-mode 50% test. This means that the BK-coefficient [57] for mixed-mode behavior could be calculated with or without the influence of fiber bridging for simulations that

do not take into account R-curve effects. The BK-coefficient with the influence of fiber bridging is 2.9 and without is 2.1. The cohesive laws derived for Mode I and II as defined in section 3.3 are implemented into a single material card in tabular format, considering the mixed-mode behavior. It is assumed that the shape of the mixed-mode 50% follows an exponential form, similar to mode II, while respecting the mixed-mode fracture energy and initiation stress according to the BK-criterion including fiber bridging. A summary of the numerical cohesive laws and corresponding J-curves are given in Figure 3.4.1.
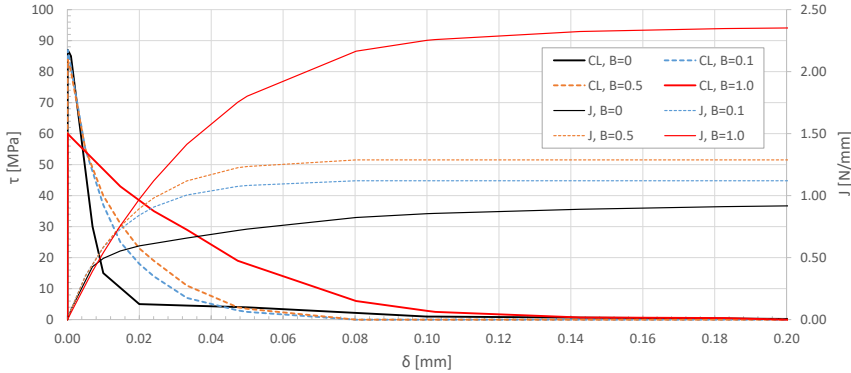
Figure 3.4.1: Summary of numerical cohesive laws and corresponding J-curves.

The simulation results of using both tabular and linear cohesive laws are compared against the experimental load-displacement and analytical solutions in Figure 3.4.2 for all the different test configurations. The results for the DCB simulation are shown in Figure 3.4.2a and the simulation using the tabular cohesive law matches the experimental load-displacement curve and the R-curve effect with high accuracy. When using the traditional data reduction approach and only the propagation fracture toughness in the numerical analysis, similar results as the analytical LEFM solution are achieved. This means that the numerical results will be inaccurate and unconservative for cracks smaller than 15mm as also indicated by the R-curve in Figure 3.3.2.

Simulating the mixed-mode bending 50% test using linear softening and low initiation strength in mode II, results in early propagation and inaccurate predictions, as explained in more detail in [76] and is solved by setting the shear initiation strength to the 5% matrix shear strength S_L = 90 MPa. This results in the correct propagation behavior as shown in Figure 3.4.2b, but no R-curve effect is observed. Initially, the mixed-mode bending 50% test also showed some issues for the tabular approach. A large mismatch during propagation as indicated by the red dotted line in Figure 3.4.2b is observed. It is found that this may be caused by the large difference in shape of the mode I and II cohesive laws due to fiber bridging, which may result in incorrect interpolation for the modes that are not included in the tabular format. Fiber bridging was not observed during the MMB50 test, however the exact mode-mixity at which this effect is not present anymore is not determined experimentally, but it is assumed to be close to mode I. It is there decided to insert another cohesive law at a mixed-mode of 10% to cut the fiber bridging contribution from the total fracture toughness.
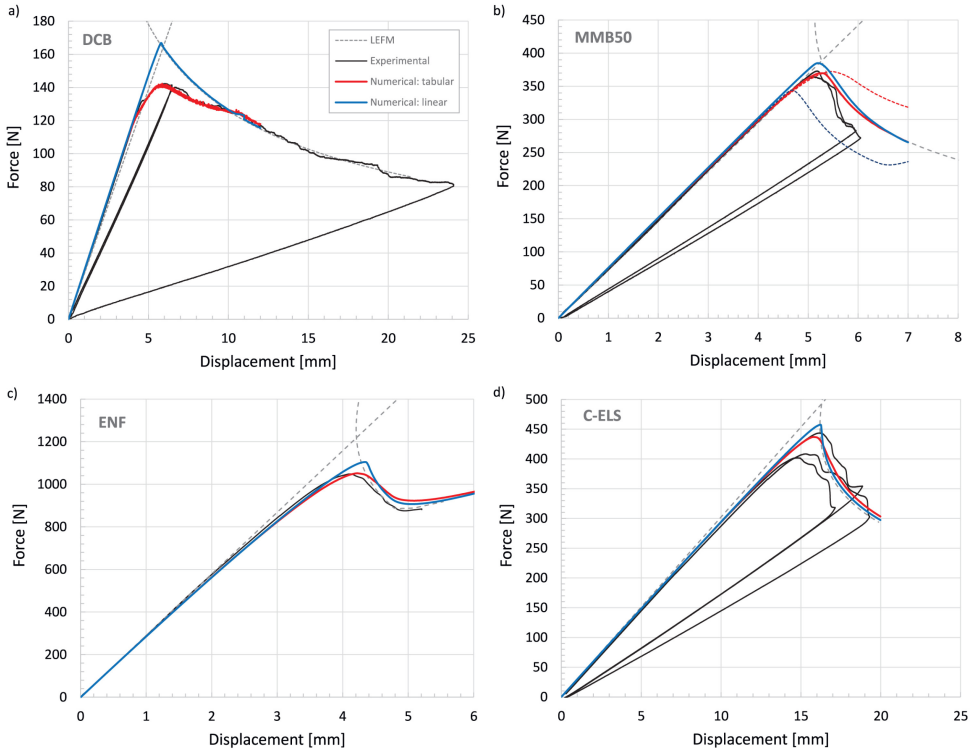
Figure 3.4.2: Experimental versus numerical results: a) Mode I - Double Cantilever Beam; b) Mixed-Mode Bending 50%, dotted line excluding B=0.1 cohesive law; c) Mode II - End-Notched Flexure; d) Mode II - Calibrated End Loaded Split.

It was found that the J-curve of the 10% and 50% cohesive laws need to reach their propagation values according to BK [57] at a much shorter opening displacement compared to mode I. From this it can be concluded that the BK interpolation is valid for the total energy, but not for the individual parts of the J-curve as shown in Figure 3.4.1. The difference between including the additional cohesive law at 10% mode mixity (B=0.1) is further investigated using the MMB50 test. It is found that a significant change in the size of the fracture process zone is observed and also a large difference in mode-mixity as damage progresses. This is shown in Figure 3.4.3 which shows the ABAQUS field output *mode mix at damage evolution (MMIXDME)* for the two different configurations. Therefore, it would be beneficial to perform additional experimental tests at different mode mixity, but it also demonstrates that the new tabular approach can be used to easily estimate the intermediate shapes of the cohesive law and it is not constrained to a fixed mixed-mode interaction for the whole J-curve.
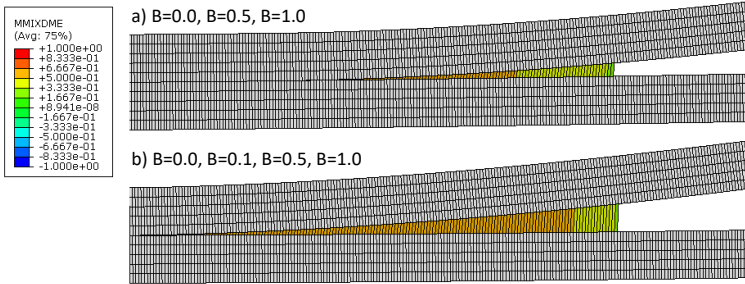
Figure 3.4.3: Mixed-mode bending 50%, mode mixity in fracture process zone: a) Tabular cohesive law excluding B=0.1; b) Tabular cohesive law including B=0.1.

It is also shown that both the ENF and CELS test can be predicted using the same cohesive law by comparing the numerical analysis with the experimental results in Figure 3.4.2c and d, thus showing that the cohesive law is independent of the test configuration. Using the low initiation strength already predicts part of the initial nonlinearity in the ENF load-displacement curve as shown in Figure 3.4.2c, and using the tabular cohesive law further improves this. For the CELS test, as shown in Figure 3.4.2d, the numerical analyses predicts the average of the experimental load-displacement curves with an improvement in the initiation when using the tabular approach. Summarizing, it is concluded that by using the proposed methodology the experimental load-displacement curves can be accurately predicted for all four tests, while using only a single material card as input.

3.5 Conclusions

The interlaminar behavior of AS4D/PEKK-FC thermoplastic composites is characterized and analyzed during quasi-static loading, while considering fiber bridging and R-curve effects. Mode I, II and Mixed Mode I/II at 50:50 experimental tests and numerical analyses are performed on the Double Cantilever Beam, End-Notched Flexure, Calibrated End Loaded Split and Mixed-Mode Bending 50% test configurations. Mode II testing with the End-Notched Flexure test method appeared to be difficult due to the large fracture process zone, but this could be adjusted for by using a larger span and a different initial crack length. Scanning electron microscopy is performed to provide new insights into the interlaminar damage mechanisms present in this large fracture process zone. The SEM micrographs confirmed the presence of large scale fiber bridging and significant plastic deformation is observed in the thermoplastic polymer matrix. The SEM micrographs also confirmed the absence of fiber bridging in Mixed Mode I/II at 50:50 and Mode II loading conditions and suggests that polymer crystallization plays and important role in the matrix-dominated behavior. A new data reduction approach based on only the load-displacement is validated on thermoplastic composites. This approach provides a convenient way of evaluating the experimental data, especially when it is difficult to accurately monitor the crack tip experimentally due to the large fracture process zone. By using this new approach it is also found that the cohesive laws of the Mode II tests were nearly identical, which confirms that the cohesive law is indeed independent of the test configuration. It is also shown that, even though both mode I and II tests were performed in different labs with different testing methods, reproducible results are obtained. Furthermore, a new procedure is developed to implement user-defined cohesive laws in commercial finite element software, without the need for user-subroutines. The procedure ensures an accurate solution, even when a high penalty stiffness and/or rapid changes in shape of the cohesive law are present. The use of these new methods also provides new insights into the role of fiber bridging on the mixed-mode interlaminar behavior. Especially in mode I, a large influences in the fracture toughness is found, while the initiation fracture toughness is found to be rather low. As fiber bridging is not present during all mode I tests, it is considered to be a likely source of scatter in the propagation fracture toughness. It is also found that fiber bridging only contributed when sufficient crack opening is present. This makes accounting for the full cohesive law important, especially for small cracks that do not benefit from this increased mechanical property. Mixed Mode I/II at 50:50 and Mode II loading conditions also showed low initiation fracture toughness values. However, the initiation strength values from the experimental cohesive laws were found the be in line with the low shear initiation strength measured during during cycle in-plane shear loading from literature. The means the shear initiation strength is close to the 0.2% or 0.5% off-set shear strength. The resulting mixed-mode tabular cohesive laws are successfully implemented into a single material card for the numerical analysis and allows to obtain good correlation for all the different experimental test configurations.

4

EXPERIMENTAL AND NUMERICAL EVALUATION OF CONDUCTION WELDED THERMOPLASTIC COMPOSITE JOINTS

The capability of joining two thermoplastic composite parts by welding is a key technology to reduce the weight and cost of assembled parts and enables high volume manufacturing of future aeronautical structures made of thermoplastic composite materials. However, there is not much experimental understanding of the mechanisms involving welded joint failure, and the computational tools available for the simulation of thermoset composites have not yet been completely assessed for thermoplastic materials. In this work, a numerical and experimental evaluation is performed to investigate the strength and failure behavior of conduction welded thermoplastic composite joints. A welded single lap shear joint is designed, manufactured, tested and analyzed proposing two distinct modelling approaches. A simplified modelling strategy which only accounts for damage at the weld is compared to a high-fidelity model which can take into account the physical failure mechanisms at the lamina level. The high-fidelity modelling methodology is able to predict the experimental failure mode of the investigated welded joints with high accuracy and is used to gain new insights into the key-variables that influence the strength of thermoplastic welded joints. It is also found that the joint strength is highly influenced by the failure mechanisms not only of the welded interface but also of the surrounding plies.

4.1 Introduction

The use of thermoplastic composite materials is gaining momentum in the transportation sector due to their improved mechanical properties, 'unlimited' shelf life and offers a number of advantages that can benefit cost-efficient and high-volume manufacturing. One of the main manufacturing techniques that enables this is thermoplastic welding. Joining of two parts is achieved by locally melting the material through application of heat and pressure. As a consequence of this local heating, very short processing times can be achieved (seconds to minutes) compared to typical manufacturing processes such as autoclave-, oven- and press-consolidation. The most established joining techniques for continuous fibre reinforced thermoplastic composites are resistance, induction and ultrasonic welding [1]. The welding technique investigated in this work is conduction welding (Patent [10]), which is currently under development at Fokker/GKN Aerospace [8, 9]. Conduction welding is based on heating the surface of the part through an induction heated tool and generating the weld bath by heat conduction through the laminate. The benefit of this technique is that it does not require addition of welding specific materials such as energy directors or conductive strips. Furthermore, the technique is more suitable and scalable for welding of large parts and allows for absorbing of manufacturing tolerances like gaps. However, introducing these fastener-free joints also comes with new challenges. The strength of these highly loaded joints relies on the performance of the thermoplastic matrix which may be influenced by the welding process. It also needs to be investigated if the joint strength is influenced by the intra- and interply failure mechanism of the composite material. This may make it difficult to predict the strength of the welded joints without the availability of advanced predictive tools.

A popular approach to model failure of joints and interfaces is the Cohesive Zone Model (CZM). The main advantage of this method is the ability to simulate both the onset and propagation of damage without the need for an initial flaw. This methodology may provide to be a convenient method to evaluate the strength of adhesively bonded joints [101–103] and delaminations [76], but due to the complex failure behavior of welded thermoplastic composites [4, 104] both inter- and intralaminar failure behavior has to be taken into account, as also observed for composite bonded joints [105].

Modelling of fracture and damage in composites has been achieved through various approaches that model the crack in either a discrete or smeared manner. For the discrete approach, the eXtended Finite Element Method (X-FEM) [29] and similar enriched finite element-based approaches such as the discrete cohesive crack approach [30] and the floating-node method [31] have been employed to simulate both intra- and interlaminar damage with high accuracy but at a high cost of computational efficiency. A methodology that provides more computational efficiency is Continuum Damage Mechanics (CDM). In continuum approaches, the effect of material degradation due to damage is modelled in a smeared manner through reducing the apparent stiffness of the material (strain-softening) inside the fracture process zone. Although strain-softening is not a real physical phenomenon at the micro-scale of the material, it provides an appealing framework to simulate the effect of damage at the meso-scale [16]. Continuum damage models are already used to study the failure behavior of composite plain and open-hole strength coupons [16] and bolted single lap shear joints [106], however their application to welded composite joints is rather limited in literature.

The aim of this chapter is to evaluate the strength and failure behavior of conduction welded joints and to develop a validated numerical methodology to support the design of thermoplastic welded joints [15]. Single lap shear specimens are designed and manufactured by means of a conduction welding robot and are tested at the Fokker/GKN Aerospace R&D facilities. For the development of the numerical methodology both a simplified and a high-fidelity approach are proposed. The validity of the modelling strategy is assessed by comparing the predictions with the experimental results. The numerical approach is then used to study the most significant material parameters and model assumptions that may influence the strength and failure modes of these welded joints.

4.2 Manufacturing and testing of welded specimens

The section describes the design, manufacturing and testing of the conduction welded thermoplastic composite single lap shear joints. The properties of the thermoplastic composite material are reported first followed by the design of the welding rig and single lap shear specimen design. The welded joints are then manufactured using a conduction welding robot and the weld quality is inspected by means of non destructive inspection. Finally, static tensile tests are performed until failure and the results are reported and discussed.

4.2.1 Thermoplastic composite material

The material used in this research is the Solvay (formerly Cytec) thermoplastic polymer prepreg which consists of a fast crystalizing thermoplastic matrix of poly(ether ketone ketone) commonly referred to as PEKK-FC, reinforced with the continuous unidirectional AS4D fiber with a nominal ply thickness of 0.138 mm. The coupons for material properties characterization are manufactured by means of autoclave consolidation and tested by Fokker/GKN Aerospace at room temperature ambient conditions and are reported in Table 4.2.1. The Young's modulus is given in both tensile and compressive direction. In the analysis, the longitudinal tensile modulus (loading direction) is used, while the average modulus is used for the transverse direction. For the matrix fracture toughness both the initiation and propagation values are measured. The longitudinal fracture data are not measured but are assumed to be the same as for the AS4 fiber reported in [16]. The longitudinal strength and fracture toughness ratios are assumed to be similar to [44] and are validated with internal Fokker/GKN Aerospace experimental open-hole coupon data.

From literature it is known that the manufacturing process may significantly influence the material properties of thermoplastic composites.Parameters such as the local temperature profile and gradients, heat-up speed, constant time and temperature at the welded interface, may affect the melting conditions [67] or flow [107] of the polymer and the cooldown speed may significantly influence the final crystallinity of the material. Furthermore, thermal residual stress may be introduced during the welding process due to both the high temperature and shrinkage of the material during cystallization. Sacchetti et al. [108] showed an increase of factor 2.5 on the fracture toughness by changing the cooling rates during processing. The main reason can be explained by changes in crystallinity of the semi-crystalline polymer that can affect the ductility and fracture properties of the thermoplastic composite material.

Table 4.2.1: AS4D/PEKK-FC thermoplastic composite material properties

Property	Description	Value	Unit
E_{1t}	Young's modulus, longitudinal tensile direction	138300	MPa
E_{1c}	Young's modulus, longitudinal compressive direction	128000	MPa
E_{2t}	Young's modulus, transverse tensile direction	10400	MPa
E_{2c}	Young's modulus, transverse compressive direction	11500	MPa
$G_{12}=G_{13}$	Shear modulus	5190	MPa
v_{12}	Poisson ratio, 1-2	0.316	-
v_{23}	Poisson ratio, 2-3	0.487	-
X_T	Longitudinal tensile strength	2350	MPa
X_C	Longitudinal compressive strength	1621	MPa
Y_T	Matrix tensile strength	87	MPa
Y_C	Matrix compressive strength	273	MPa
S_L	Matrix 5% shear strength	90	MPa
α_{pl}	Ramberg-Osgood fitting parameter 1, non-linear shear	8.5E-10	-
η_{pl}	Ramberg-Osgood fitting parameter 2, non-linear shear	5.9	-
G_{Ic_i}	Mode I matrix fracture toughness, initiation	0.7	kJ/m^2
G_{Ic_p}	Mode I matrix fracture toughness, propagation	1.12	kJ/m^2
G_{IIc_i}	Mode II matrix fracture toughness, initiation	1.45	kJ/m^2
G_{IIc_p}	Mode II matrix fracture toughness, propagation	2.35	kJ/m^2
η	Benzeggagh-Kenane coefficient	2.9	-
G_{XT}	Longitudinal tensile fracture toughness	125	kJ/m^2
G_{XC}	Longitudinal compressive fracture toughness	61	kJ/m^2
f_{XT}	Longitudinal tensile strength ratio	0.8	-
f_{XC}	Longitudinal compressive strength ratio	0.8	-
$f_{G_{XT}}$	Longitudinal tensile fracture toughness ratio	0.3	-
$f_{G_{XC}}$	Longitudinal compression fracture toughness ratio	0.3	-
α_{11}	Coefficient of thermal expansion, longitudinal direction	0.19e-06	$/°C$
α_{22}	Coefficient of thermal expansion, transverse direction	3.17e-05	$/°C$

However, it is shown in [67] that for the material used in this work (PEKK-FC), even at high cooldown rates (-60 °C/min) the material still achieves high levels of crystallinity (Xc=27%). This is however, still significantly lower compared to crystallinity (Xc=36%) measured with very slow cooldown rates (-0.5 °C/min), so some influence on the local material properties due to changes in crystallinity is expected. Grouve et al. [109] investigated the sensitivity and effect of material variability of the C/PEKK-FC material during induction heating. It was found that laminates showed a inhomogeneous fiber distribution and resin rich regions were identified. This variability may have a significant effect on temperature evolution in the welded joint. Furthermore, it is also known [66] that excessive resin or a thick interface may also increase the fracture toughness, as this may allow for more plastic deformation at the crack tip. Accounting for these influences in the analysis would require detailed knowledge on the local thermal behavior and characterization of the in-situ material properties, which is out-of-scope for this work. However, the developed numerical methodology is used to study the effect of changes in material properties on the joint strength and failure behavior.

4.2.2 Welding setup and single lap shear specimens

The rig shown in Figure 4.2.1a is designed to support the welding of two laminates by means of a conduction welding robot. The laminates are welded at three positions and specimens are machined from the center section of each weld as shown in Figure 4.2.1b in order to create a single lap shear specimen. The specimen design (Figure 4.2.1c) follows ASTM standard D3165 [110], with overlap length of 30 mm and nominal width of 25.4 mm. The length of each composite laminate is 75 mm and the height of the weld at the interface is approximately 18 mm. This dimension is a typical value measured from the weld size of the tested samples. The layup of the composite laminates consists of 16 plies ([-45,0,45,90,-45,90,45,0]$_S$) for each laminate which is rotated to create a +45/-45 interface at the weld. The 0-degree ply is oriented in the loading direction of the specimen.
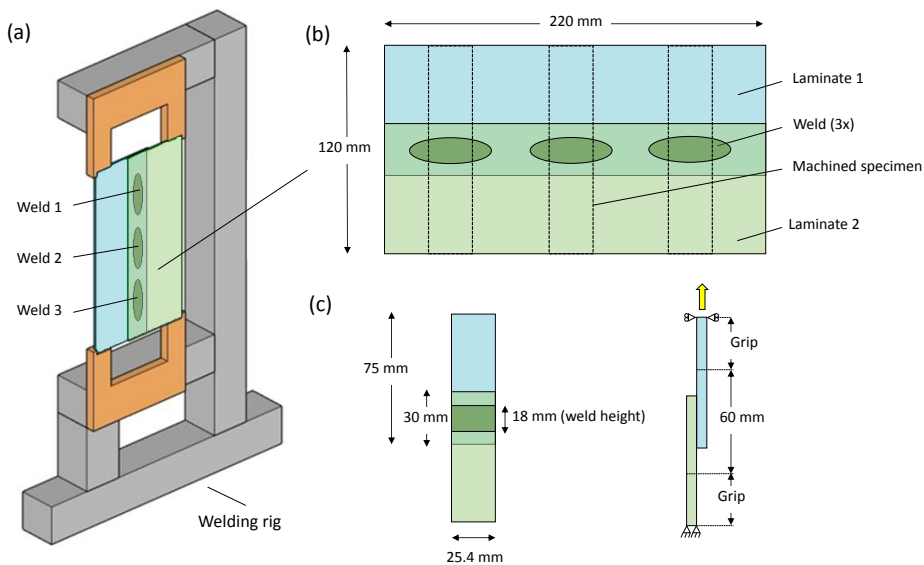
Figure 4.2.1: Welding of single lap shear specimens: a) Conduction welding rig; b) Details of welded laminates, c) Single lap shear specimen.

4.2.3 Conduction welding of the laminates

All laminates used in the test campaign are manufactured from two large autoclave consolidated AS4D/PEKK-FC laminates according to a typical process cycle for aeronautical parts and are cut into smaller laminates for welding. Additional PEKK-FC foil is included in each laminate to make sure sufficient resin is present at the weld interface. The welding robot, shown in Figure 4.2.2, consists of a clamping system which applies local heat and pressure through an induction heated stamp. The two AS4D/PEKK-FC laminates are positioned and clamped by the robot after which heat and pressure are applied to locally melt the thermoplastic material. The system is heated from one side at approximately 400 °C in order to reach the typical processing temperature of 377 °C [61] at the welded interface and to ensure a complete melt [67]. The maximum temperature is limited to approximately

400 °C in order to prevent polymer degradation at the laminate surface near the welding tool. This value is based on Fokker/GKN experience and can be determined by techniques such as thermogravimetric analysis (TGA).
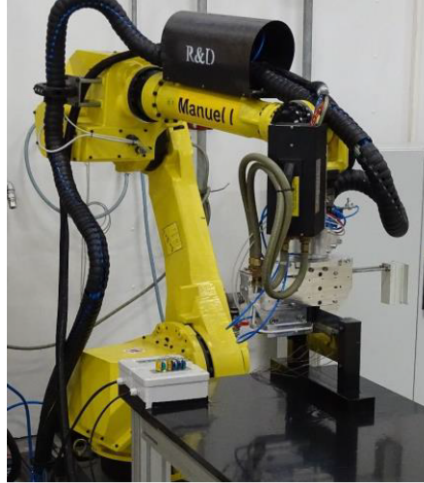
Figure 4.2.2: Conduction welding robot at Fokker/GKN Aerospace.

The welding temperature is measured at the weld interface by means of several thermo-couples and the quality of the weld is inspected by means of Non Destructive Inspection (NDI) by using a phased array setup that inspects the width and the position of the conduc-tion weld. The equipment consist of the Omniscan MX and a probe that generates ultrasonic soundwaves. When putting the probe on the composite laminate the sound waves travel through the composite plate and reflect back to the probe. The sound waves are dampened when a change in density is detected. This can be an indication of voids, delaminations or an area which is not welded. The different type of scans that are performed are shown in Figure 4.2.3 on a conduction welded laminate. NDI C-scan results are shown in Figure 4.2.4 where the colors represent the damping of the sound. The color red is 0% and blue is 100% attenuation of the ultrasonic sound waves. The phased array probe can perform different types of scans. The A-scan provides information about a local point of the weld; this point is perpendicular to the welding location. The C-scan provides information about the weld in top view. The S-scan provides information about the cross-section of the weld, perpendicular to the weld, this is a combination of the data from the A- and C-scan.

The C-scan results of the first welded laminate (Specimens 1-3, Table 4.2.2) is compared in Figure 4.2.4a to a welded laminate with a more consistent weld quality and higher strength (Specimens 7-9, Table 4.2.2) in Figure 4.2.4b. Figure 4.2.4a shows some indication of delamination or variation through the thickness (blue-green region with <50% attenuation) compared to the higher quality welds in Figure 4.2.4b that show a more consistent C-scan result above 50% attenuation.
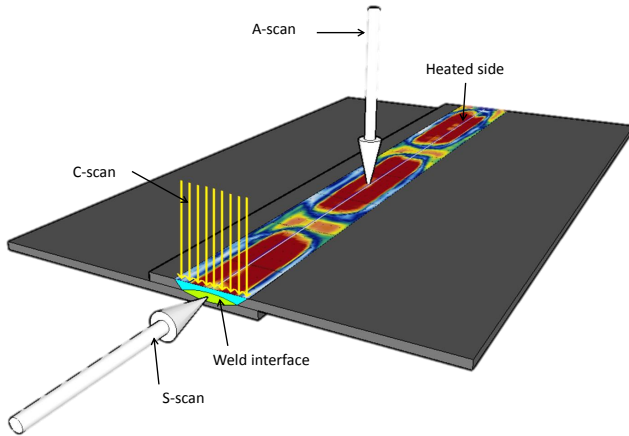
Figure 4.2.3: NDI of conduction welded laminates.
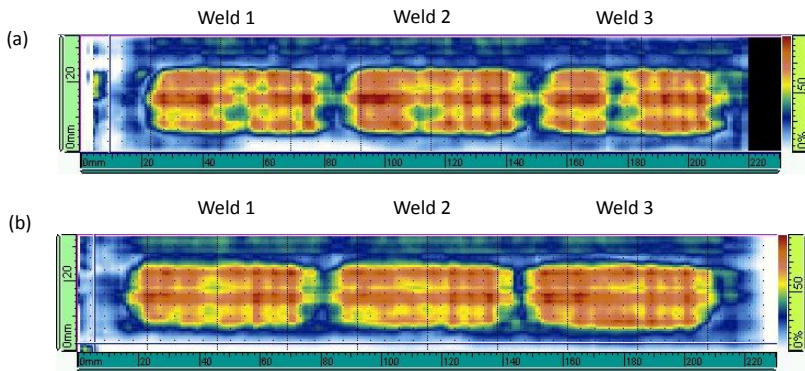
Figure 4.2.4: NDI C-scan results: (a) Welds for specimen 1-3, with indications (<50% attenuation zones); (b) Welds for specimen 7-9, more consistent quality welds (all >50% attenuation).

4.2.4 Experimental results

In total, 21 conduction welded single lap shear joints are manufactured and tested. Static tensile tests are performed according to ASTM D3165 [110] until failure.

The tests are carried out using a ZWICK 100kN universal test machine with self-aligning wedge grips. The cross-head speed is set to 1 mm/min and the test is automatically stopped after measuring a load drop to 75% of the highest measured force. It is noticed that the self-aligning grips do not provide clamped conditions at the grip area and some gapping is observed due to secondary bending, so the effective specimen length between the grips is unknown. Furthermore, the clamping pressure of these wedge grips increases during loading due to axial movement. This makes comparing load-displacement curves of the experimental and numerical results difficult, as the machine displacement includes both the machine compliance and the movement of the wedge grips. Therefore, the numerical load-displacement curve is only compared to the experimental failure loads.

The results are shown in Table 4.2.2. The specimens are grouped according to the laminates from which they are machined. The relation of the weld position with the specimen, is also given. Furthermore, the height of the weld and the measured weld area based on the fracture surface are also reported. The average failure load is 18841 N and the minimum and maximum failure loads are 12307 N and 21556 N, respectively.

Table 4.2.2: Welded single lap shear joint experimental results.

Specimen (Weld) number	Weld position	Specimen width [mm]	Weld height [mm]	Weld surface [mm2]	Failure load [N]
1	1	25.48	17.32	441	12307
2	2	25.50	17.65	450	20348
3	3	25.48	17.41	444	14675
4	1	25.49	17.60	449	19929
5	2	25.48	18.05	460	20535
6	3	25.49	17.92	457	13594
7	1	25.49	17.91	457	19608
8	2	25.47	17.50	446	19805
9	3	25.47	17.09	435	18771
10	1	25.50	17.87	456	19780
11	2	25.51	17.67	451	20656
12	3	25.52	17.54	448	20298
13	1	25.53	17.88	456	20403
14	2	25.53	17.87	456	20890
15	3	25.54	17.89	457	17780
16	1	25.51	17.49	446	18177
17	2	25.50	18.09	461	19731
18	3	25.49	17.63	449	19788
19	1	25.49	18.00	459	16893
20	2	25.54	18.08	462	21556
21	3	25.49	17.36	443	20133

The failure modes of a typical lower (Specimen 3) and higher bound experimental result (Specimen 8) are shown in Figure 4.2.5. The fracture surface of the weld is shown for both the top and bottom laminate as indicated in Figure 4.2.5a. For Specimen 3 the failure mode extended outside of the weld (Figure 4.2.5b), which may be related with the NDI indication at the same location as shown in Figure 4.2.4a. It is also observed that the failure mode of Specimen 8 show clear signs of a resin rich area at the tip of the weld and clear signs of delamination propagation (light colored zone) as indicated in Figure 4.2.5c. The failure modes are investigated and explained in more detail in section 4.4 evaluating the results from the numerical analysis.
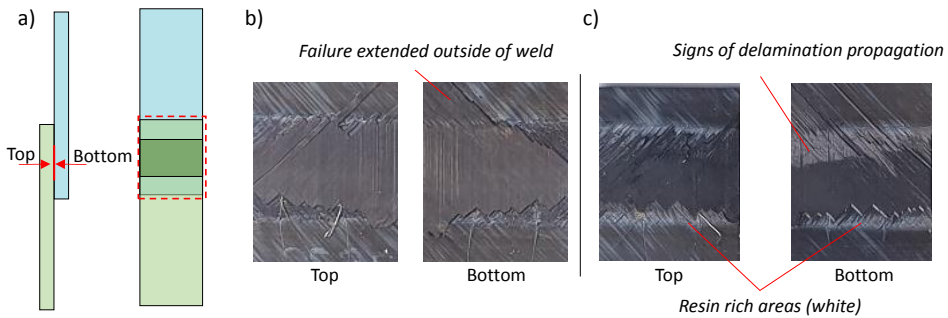
Figure 4.2.5: Failure modes of welded single lap shear specimens: a) Specimen geometry and views; b) Specimen 3; c) Specimen 8.

4.3 Modelling strategy

Two numerical strategies are explored to analyse the strength of the thermoplastic conduction welded single lap shear joints. The first simplified approach considers failure only at the welded joint and simplifies all damage mechanisms into a single cohesive interface (Figure 4.3.1), while the second follows a high-fidelity approach that considers both inter- and intralaminar damage in each ply of the single lap shear joint and the welded interface (Figure 4.3.2). This section first explains the general model parameters and geometry, followed by the damage models used in the work and a study on how to efficiently simulate single lap shear joints in ABAQUS/Explicit [45].

4.3.1 Models and parameters

The two models follow the specimen design and geometry as shown in Figure 4.2.1. The single lap shear joint is divided into two zones and assembled from separate parts. The composite sections at the load introduction, which are far from the welded joint, are discretised with through-thickness continuum shell elements (SC8R) as shown in Figure 4.3.1a and considers only linear-elastic material behavior. The central zone of the joint in the simplified model is also modelled using SC8R elements but a smaller mesh size is used to meet mesh size requirements [99] for cohesive zones. The central section consists of a surface with contact (Figure 4.3.1b) and cohesive surface for the welded interface (Figure 4.3.1c).
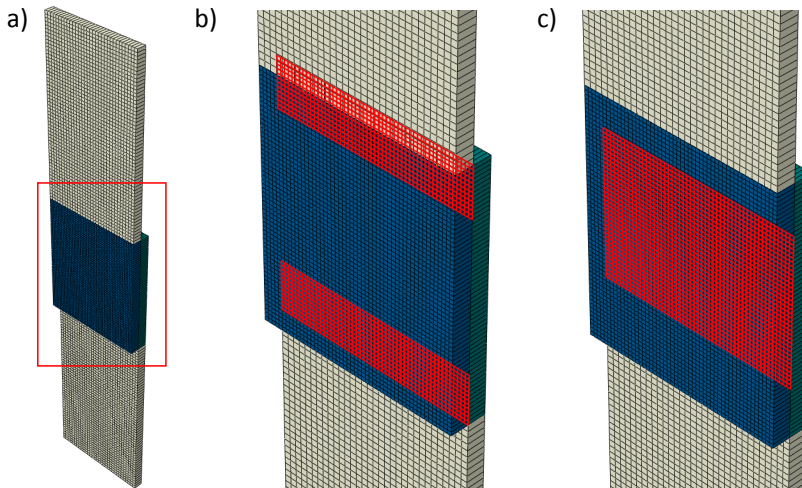
Figure 4.3.1: Simplified single lap shear model: a) Continuum shell model; b) Contact surface outside of weld; c) Cohesive surface of welded interface.

The central zone of the high-fidelity model, also referred to the damage zone, is shown in Figure 4.3.2a and follows a ply-by-ply modelling strategy where each ply is discretized as a layer of reduced-integration solid elements (C3D8R). A fiber aligned mesh with an aspect ratio of three is used following the guidelines given in [16]. The welded interface, as

in the simplified model, consists of a cohesive surface for the weld and a contact definition outside of the weld, as shown in Figure 4.3.2b.
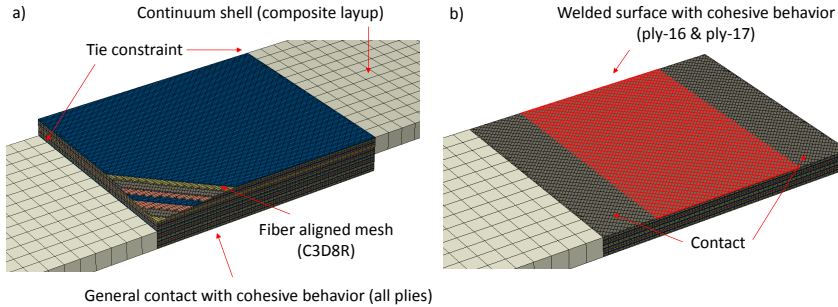
Figure 4.3.2: High-fidelity single lap shear model: a) Overview of different model features; b) Details on welded surface showing only the lower laminate.

The connection between the damage zone and supports is implemented with kinematic constraints (*TIE) in order to transfer displacements and rotation across their boundaries. The boundary conditions are applied by means of a velocity amplitude profile imposed at the top and bottom surfaces of the supports. The fixed boundary condition at the bottom surface is enforced by means of conditions of zero velocity while the velocity at the top surface is ramped-up to a constant velocity until failure. The simplified model consists of approximately 10.000 elements, while the high-fidelity model consists of approximately 100.000 elements. The optimization of the analysis parameters to achieve efficient analysis times is explained in more detail in section 4.3.3.

4.3.2 INTER- AND INTRALAMINAR DAMAGE MODEL

Failure of the welded joints is considered to be similar to the failure of general composite laminates due to the nature of the joining process. The laminate is locally melted and consolidates in a similar manner as consolidating plates in an autoclave process, if the right manufacturing conditions are respected. This means that the welded interface is locally indistinguishable from the bulk material. Therefore, the failure of the welded joint is expected to behave the same as interlaminar damage in the thermoplastic composite material and that a zero-thickness interface can be assumed, which is different from bonded joints that have a non-zero adhesive thickness.

The failure mechanisms of the welded joint can therefore be divided into the typical categories of composite failure modes, namely interlaminar and intralaminar damage. Failure of the weld and failure of the ply-to-ply interface of the laminates fall into the interlaminar category. This damage behavior affects the separation between plies, which forms a delamination that can occur under different opening modes. Intralaminar damage considers all the failure modes that occur within each ply such as fiber and matrix failure. The interlaminar model already available in ABAQUS/Explicit has been used, while the intralaminar model has been implemented in a Continuum Damage Model (CDM) through a user-defined "VUMAT" subroutine using a numerically explicit integration scheme.

Interlaminar damage

The interlaminar behavior of the welded joints is modelled through the general contact algorithm available in ABAQUS/Explicit [45]. This method takes care of the kinematics of surface contact, cohesive and frictional behavior. The cohesive zone model describes the opening of the delamination in terms of tractions and displacements. Once damage is initiated, the model reduces the stiffness of the cohesive surface thus decreasing the traction while dissipating the fracture energy corresponding to the specific mixed-mode opening mode, as given by the Benzeggagh-Kenane criterion [57]. Damage initiation is identified by means of a quadratic nominal stress failure criteria which is a function of the interlaminar strength values for each damage mode. Frictional effects are considered on the surface to include possible effects of ply friction within the delaminations. For the simplified model, this behavior is only considered at the weld interface as shown in Figure 4.3.1c, while for the high-fidelity model it is considered for each ply interface. Outside the weld surface, only contact and frictional behavior are considered. A value of $200000 N/mm^3$ is used for the mode I penalty stiffness and Turon's equation [58] is used to calculate the shear penalty stiffness value. Friction is considered to be ply interface angle dependent and follows the approach and values from [19].

Intralaminar damage

CDM is used for modelling damage in the plies taking into account the three-dimensional stress states through the physically-based three-dimensional failure criteria proposed by Catalanotti et al. [46]. This effect is considered to be important for the analysis of single lap shear joints because significant out-of-plane loading may be present due to secondary bending. The implementation follows the approach defined in [19] and is originally based on the work of Maimi et al. [47] that guarantees the correct energy dissipation for each composite fracture mode. The model is also enhanced to account for large shear deformations through the use of the 2nd Piola-Kirchhoff stress and Green-Lagrange strain to accurately predict matrix cracks and ply splits as demonstrated in [40, 111]. Capturing large shear deformations is relevant for accurately predicting the matrix-dominated failure modes of the welded joints. The implementation following [56] is briefly explained below and the influence of some of the assumptions are discussed in Section 4.4.

The stress and strain in the element is based on a Lagrangian kinematic measure where the constitutive equations can be defined within a orthonormal material frame. Therefore, fiber rotation due to large shear deformation is intrinsically captured. The 2nd Piola-Kirchhoff stress $\mathbf{S}$ is the work conjugate to the Green-Lagrange strain $\mathbf{E}$, which is determined from the deformation gradient tensor $\mathbf{F}$:

$$\mathbf{E} = \frac{1}{2} \left(\mathbf{F}^\top \cdot \mathbf{F} - \mathbf{I} \right) \tag{4.1}$$

where $\mathbf{I}$ is the identity tensor. The 2nd Piola-Kirchhoff stress $\mathbf{S}$ can be determined from the material stiffness tensor $\mathbf{C}$ and the Green-Lagrange strain $\mathbf{E}$:

$$\mathbf{S} = \mathbf{C} : \mathbf{E} \tag{4.2}$$

and can be mapped to the current configuration by

$$\boldsymbol{\tau} = \mathbf{F} \cdot \mathbf{S} \cdot \mathbf{F}^T \text{ and } \boldsymbol{\sigma} = \frac{1}{J} \boldsymbol{\tau} \text{ with } J = \det(\mathbf{F}) \tag{4.3}$$

where $\boldsymbol{\tau}$ and $\boldsymbol{\sigma}$ are the Kirchhoff and Cauchy stress. The stress has to be returned in the co-rotational basis of Abaqus ($\boldsymbol{\sigma}_{abq}$) through a change of basis operation by using the rotation matrix $\mathbf{R}$.

$$\boldsymbol{\sigma}_{abq} = \mathbf{R} \cdot \boldsymbol{\sigma} \cdot \mathbf{R}^T \tag{4.4}$$

The strain tensor for an orthotropic ply is defined as $\{\boldsymbol{\epsilon}\} = [H(d_M)]\{\boldsymbol{\sigma}\} + \{\boldsymbol{\alpha}\}\Delta T$, where $\{\boldsymbol{\sigma}\}$ is the tensor of effective stresses in Voigt notation, ΔT is the isotropic thermal load and $\{\boldsymbol{\alpha}\}$ are the ply thermal expansion coefficients following the normal orthotropic directions. Although the model can take into account the influences of thermal stress due to the welding process, this has not been considered in this work, as this would require detailed knowledge and prediction of the local thermal gradients and material behavior during welding conditions.

The laminate compliance tensor $[H(d_M)]$ is affected by the damage variables $d_M(M = 1\pm, 2\pm, 3\pm, 4, 5, 6)$ in each orthotropic direction and is associated with the damage evolution laws for each failure mode, respectively in fiber/longitudinal ($M = 1\pm$), matrix/transverse ($M = 2\pm, 3\pm$) and matrix shear ($M = 4, 5, 6$).

The compliance tensor, following the convention adopted in the ABAQUS/Explicit implementation, is expressed as:

$$[H(d_M)] = \begin{bmatrix} \frac{1}{(1-d_1)E_1} & -\frac{v_{12}}{E_1} & -\frac{v_{12}}{E_1} & 0 & 0 & 0 \\ -\frac{v_{12}}{E_1} & \frac{1}{(1-d_2)E_2} & -\frac{v_{23}}{E_2} & 0 & 0 & 0 \\ -\frac{v_{12}}{E_1} & -\frac{v_{23}}{E_2} & \frac{1}{(1-d_3)E_3} & 0 & 0 & 0 \\ 0 & 0 & 0 & \frac{1}{(1-d_6)G_{12}} & 0 & 0 \\ 0 & 0 & 0 & 0 & \frac{1}{(1-d_4)G_{23}} & 0 \\ 0 & 0 & 0 & 0 & 0 & \frac{1}{(1-d_5)G_{13}} \end{bmatrix} \tag{4.5}$$

Softening laws are used to ensure physically correct dissipation of fracture energy for each failure mode. The exponential softening law in general form, which is used for all matrix failure modes, is expressed in equation 4.6.

$$d_M = 1 - \frac{1}{r_M} \exp\{A_M[1 - r_m]\}(M = 2\pm, 3\pm, 4, 5, 6) \tag{4.6}$$

where $r_M(M = 1\pm, 2\pm, 3\pm, 4, 5, 6)$ are elastic domain thresholds, which are initially 1.0 for an undamaged material and increase after damage initiation. The physically-based three-dimensional failure criteria proposed by Catalanotti et al. [46] is used to identify initiation of damage and can also account for combined loading effects. The parameter A_M ensures that the dissipated energy is independent of mesh refinement [112] by relating the element characteristic length $l_i^*(i = 1, 2, 3)$ for a fiber aligned mesh with the material and fracture properties in the corresponding directions. For matrix damage the equation is as follows [19]:

$$A_M = \frac{2l_i^* X_{mm}^2}{2E_{mm}G_{mm} - l_i^* X_{mm}^2}(M = 2\pm, 3\pm, 4, 5, 6, i = 2, 3) \tag{4.7}$$

Matrix cracking is assumed to occur under general mixed-mode (mm) conditions, with initiation X_{mm} predicted by the three-dimensional failure criteria and the propagation fracture energy G_{mm} by the energy-based Benzeggagh-Kenane (BK) criterion [57].

Softening in fiber direction requires taking into account both fiber pull-out and bridging and is implemented through a trilinear softening law following the implementation of CompDam [44]. However, this failure mode is less relevant for the matrix dominated failure modes of the welded single lap shear joints.

Failure in out-of-plane direction is accounted for by the cohesive surfaces between the plies and can be disabled in the CDM, but nonlinear elastic-plastic response is taken into account for each shear direction (1-2, 1-3, 2-3). This is achieved using the Ramberg-Osgood equation following the implementation of CompDam [44]. The engineering shear strain (γ_i) is defined as:

$$\gamma_i = \frac{\tau_i + \alpha_{pl}\,sign(\tau_i)|\tau_i|^{\eta_{pl}}}{G_i}(i = 12, 23, 13) \tag{4.8}$$

where α_{pl} and η_{pl} are the fitting parameters obtained with experimental data from in-plane shear tests. The nonlinear shear response is assumed to be plastic until the onset of damage, after which the element is damaged following an exponential softening law that is regularized according to the mode II fracture toughness.

The use of exponential softening laws allows for gradual changes in stiffness and a more robust solution, however during softening the strains in the elements may reach very high strain levels. Furthermore, highly distorted elements, which can be detected by sudden changes in volume, may influence the stability of the analysis. These elements can be detected through the determinant of the deformation gradient $\det(\mathbf{F})$ [54]. The criteria for element deletion is adopted from [16], with more strict conditions during very large deformation. In summary, the elements fulfilling any of the following criteria are deleted during the simulation:

$$
\begin{aligned}
d_{1\pm} &\geq 0.99999 \\
|\epsilon_i| &\geq 1.0(i = 1, 2, 3) \\
|\gamma_i| &\geq 1.0(i = 12, 23, 13) \\
\det(\mathbf{F}) &\leq 0.4 \text{ or } \det(\mathbf{F}) \geq 4.0
\end{aligned}
\tag{4.9}
$$

4.3.3 Analysis parameters explicit finite element method

The explicit finite element method implemented in ABAQUS is selected for the analysis, as it involves solving a highly nonlinear dynamic problem such as large displacements, non-linear material behavior including damage and complex contact interaction with damage and frictional behavior. In order to perform computational efficient analyses in ABAQUS/Explicit, the total analysis time should be as short as possible. This can be achieved by mass-scaling or through the loading velocity. Mass-scaling up to 1000x as proposed in [16] combined with high loading velocities may not be a issue for in-plane coupons such as plain and open-hole strength, but they may cause unwanted dynamic effects such as oscillations and overshoots for problems that are more sensitive to dynamic or inertia effects. This may be the case for single lap shear joints as in-plane loading results in out-of-plane deformation due to secondary bending. The three main parameters that determine the total analysis time are (1) the stable time increment related to element size and density, (2) the ramp up time or loading amplitude and (3) the loading velocity. Although the element size is a parameter that could be adjusted, it is indirectly limited through the mesh size requirement of the damage models. This leaves the density, loading amplitude and velocity as the main parameters for the investigation. The simplified model has been used to conduct the parameter study. The following combination of parameters is investigated:

1. Mass-scale factor: 1, 10, 100 and 1000 [-]

2. Loading amplitude: 0.001, 0.0025, 0.005 and 0.01 [s]

3. Velocity: 25, 50 and 100 [mm/s]

Where the baseline analysis is defined with a density scaling factor of 1, a loading amplitude of 0.01s and a velocity of 25 mm/s. The total analysis time for this case is over 2 hours on 10 CPUS (Intel(R) Xeon(R) CPU E5-2640v4 @ 2.40GHz). The predicted failure load is checked against the solution of the implicit solver and the results are nearly identical. If is found that by using the maximum mass-scaling factor and loading velocity, severe dynamic effects occur and the failure load is over-predicted by approximately 10 percent. This means that the typical parameters for in-plane coupons [16] are not valid for single lap shear joints. Based on the results of this study, it is chosen to select a loading velocity of 50 mm/s in combination with a ramp up time of 0.0025 s and 10 times mass-scaling. This results in an analysis time of approximately 20 minutes on 10 CPU which is a significant reduction in analysis time compared to the baseline of over two hours, while staying within 1% of the expected failure load. On the high-fidelity model this results in a analysis time of 8 to 10 hours when using 20 CPUS.

4.4 Numerical evaluation of thermoplastic conduc-tion welded single lap shear joints

The strength and failure modes of the welded joint are evaluated using the two modelling approaches and comparisons are made against the experimental results. First, only failure at the welded interface is considered using the simplified approach followed by a discussion on the apparent fracture toughness of the welded joint. The high-fidelity model is then used to investigate failure of the surrounding plies and to study the behavior due to these additional failure modes. This is followed by a discussion on the influence of the inter- and intralaminar material properties and some limitations of the modelling approaches are identified.

4.4.1 Simplified modelling approach

The single-lap shear specimens are at first simulated using the simplified approach which only accounts for damage in the welded interface. The material properties used are reported in Table 4.2.1 and the ply thickness is adjusted to 0.144 mm, based on the measured thickness of the test specimens. The mode I and mode II propagation fracture toughness values measured from unidirectional specimens are used in the cohesive model for the weld.
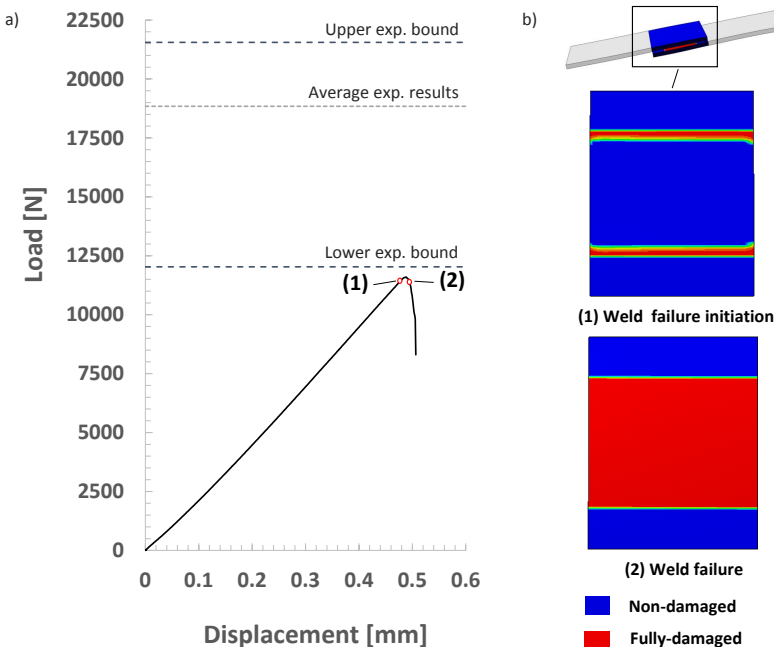
Figure 4.4.1: Simplified model result: a) Load-displacement curve; b) Initiation of weld failure and failure of welded interface after reaching the peak load.

The grip length is conservatively taken as the full specimen length as support conditions of the self-aligning wedge grips are difficult to determine. Some analyses are performed to

study the influence of the gripping distance and the predicted failure loads would increase by 1-2% due to slightly reduced secondary bending of the specimen. The numerical load-displacement curve is compared against the upper and lower bound experimental results in Figure 4.4.1a. The status of the weld can be represented by the cohesive damage variable (CSDMG) that identifies the area of the weld undergoing degradation. This is shown for two locations along the load-displacement curve in Figure 4.4.1b. During damage initiation at the edge of the welded joint a Fracture Process Zone (FPZ) develops where the damaged area becomes critical, causing the load-displacement curve to suddenly drop. The predicted failure load using this approach is 11597 N which is just below the lower experimental bound equal to 12307 N. The mismatch between the numerical and experimental results can be caused by several factors. The most likely causes are the influence of the +45/-45 interface angle, the more complex failure modes, that are not taken into account by the simplified modelling approach, and the influence of the manufacturing process on the material properties as discussed in section 4.2.2.

4.4.2 Apparent fracture toughness of conduction welded joints

The simplified modelling approach is used to investigate how the fracture toughness determines the upper and lower bounds of the experimental campaign. The strength of the joint is analyzed scaling the interlaminar fracture toughness of the material, which can be referred to as the apparent fracture toughness of the joint. The result of this study is shown
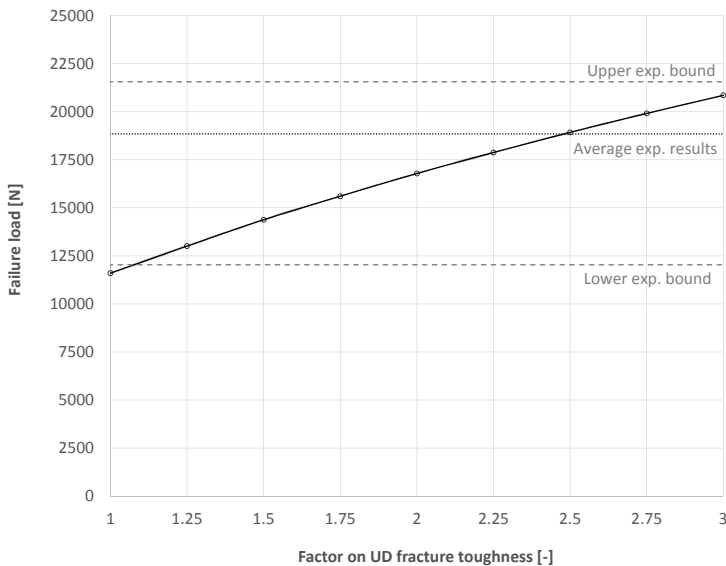
Figure 4.4.2: Influence of scaled interlaminar fracture toughness on conduction welded joint strength.

in Figure 4.4.2 where the joint strength is plotted against a factored interlaminar fracture toughness. It becomes clear that the interlaminar fracture toughness has to be increased by approximately a factor three in order to achieve the upper bound experimental results.

The average experimental results can be approached by using a factor of 2.5. The apparent fracture toughness of the joint can be used in an engineering approach to take into account effects such as changes in material properties, dependence of the fracture properties on the interface mismatch angle or complex failure mechanisms that cannot be predicted with the simplified modelling approach. The benefit of this is that the effective material properties can be determined at the coupon level and applied in coarser models at the structural level to efficiently perform simulation at that scale. Compared to thermoset composites, the fracture toughness of thermoplastic composites is much higher, making it easier to meet mesh-size requirements in cohesize zone or VCCT analyses [99, 113] with a coarse mesh and reduce mesh dependency. However, the validity has to be further investigated for different materials, loading modes and interface angles.

4.4.3 High-fidelity modelling approach

The high-fidelity modelling approach described in Section 4.3 is used to predict both the failure load and failure mode of the welded single lap shear joint. The same geometry and unidirectional material properties are used as the simplified model, but now following the ply-by-ply modelling strategy as shown in Figure 4.3.2 that allows for both intra- and interlaminar damage. The numerical load-displacement curve is compared with the upper and lower bound experimental results, and also with the curve obtained using the simplified model, in Figure 4.4.3a.
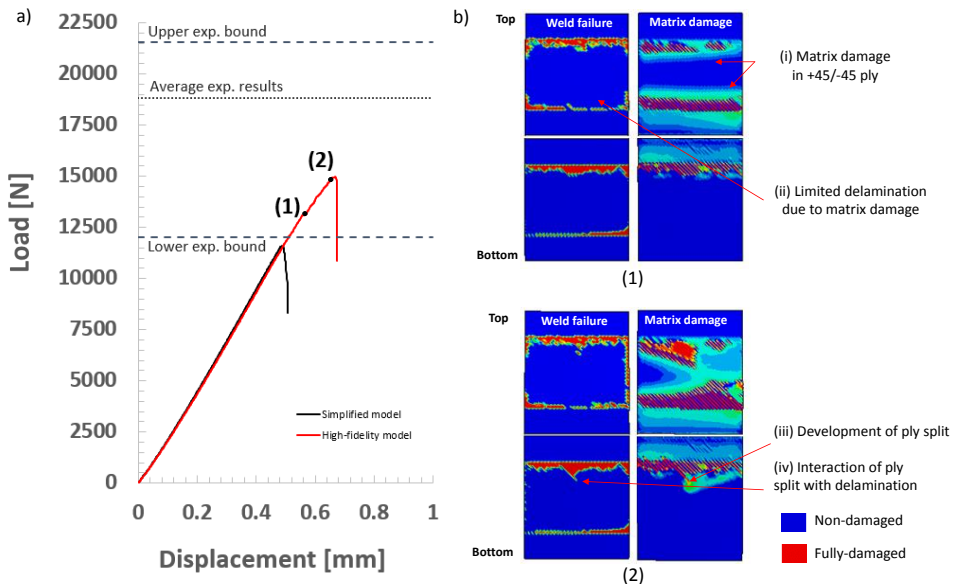
Figure 4.4.3: High-fidelity model results: a) Load-displacement curve compared to simplified model; b) Predicted weld and matrix damage at two points along the load-displacement curve.

It is evident that the joint strength is highly influenced by the complex interaction of failure modes in the surrounding plies of the laminates. The predicted failure load

following the high-fidelity approach is 14962 N. Figure 4.4.3b shows the failure modes at two points along the load-displacement curve prior to final failure. Both the weld failure (delamination, CSDMG) and matrix damage (D2) are shown in Figure 4.4.3b for each side of the joint indicated with the top and bottom view. The failure process predicted by the numerical model at the first point is as follows: (i) Matrix damage starts to develop in both 45 degree plies near the edges of the weld. This occurs at approximately the failure load of the simplified model. (ii) The damage appears to slow down the initiation of delamination in the weld interface, while the matrix damage starts to develop ply splits along the fiber direction in the 45 degree plies. Further along the load-displacement curve at the second point these ply splits (iii) continue to grow and migrate into delaminations between the first and second ply above the weld interface and (iv) will cause the joint to fail after they become critical.
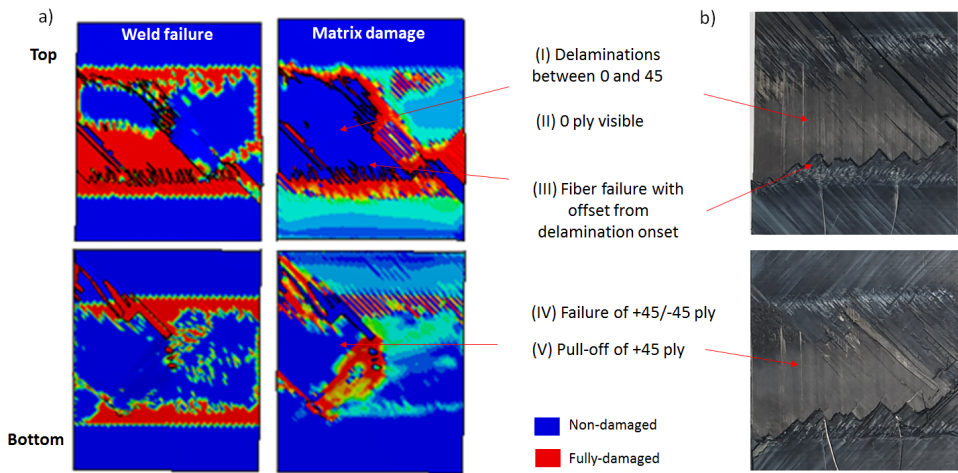
Figure 4.4.4: Comparison between final failure modes: a) Numerical prediction; b) Experimental data of failure mode.

The final failure mode of the numerical model is compared in Figure 4.4.4a to the experimental failure mode in Figure 4.4.4b and similarities can be identified. The main failure mode, that most likely caused the failure of the single lap shear joint, is the large delamination between the first ply at 45 degree and second ply at 0 degree (I) and not at the +45/-45 degree welded joint interface, because a large portion of the zero degree ply (II) is visible. Another interesting feature is the location at where the 45 degree ply failed by means of fiber failure (III) which is at an off-set from where the delamination initiation is predicted by the numerical model. The white markings on the test sample are a sign of resin rich areas at the edge of the weld which may increase the initiation strength and fracture toughness locally [66]. Several ply splits of the +45/-45 ply (IV) are visible on both sides of the specimen, which led to the pull-off of one of the 45 degree plies (V) due to the interaction with delamination on the 0/45 interface.

4.4.4 Influence of the fracture properties

The influence of the intra- and interlaminar and weld interface fracture properties on the single lap shear joint strength and failure mode is investigated by using the high-fidelity modelling approach. Changes in these properties could, as already discussed, be caused by the manufacturing process but also by assumptions in the modelling approach such as taking into account in-situ material strength or by accounting for the full cohesive law of the different fracture modes and/or the effect of interface layup angles at the welded interface (0/0 versus +45/-45).

Several different models, see Figure 4.4.5, are run with different fracture toughness values for intra- and interlaminar fracture properties in order to gain insight into how the material properties influence the joint strength and corresponding failure modes.
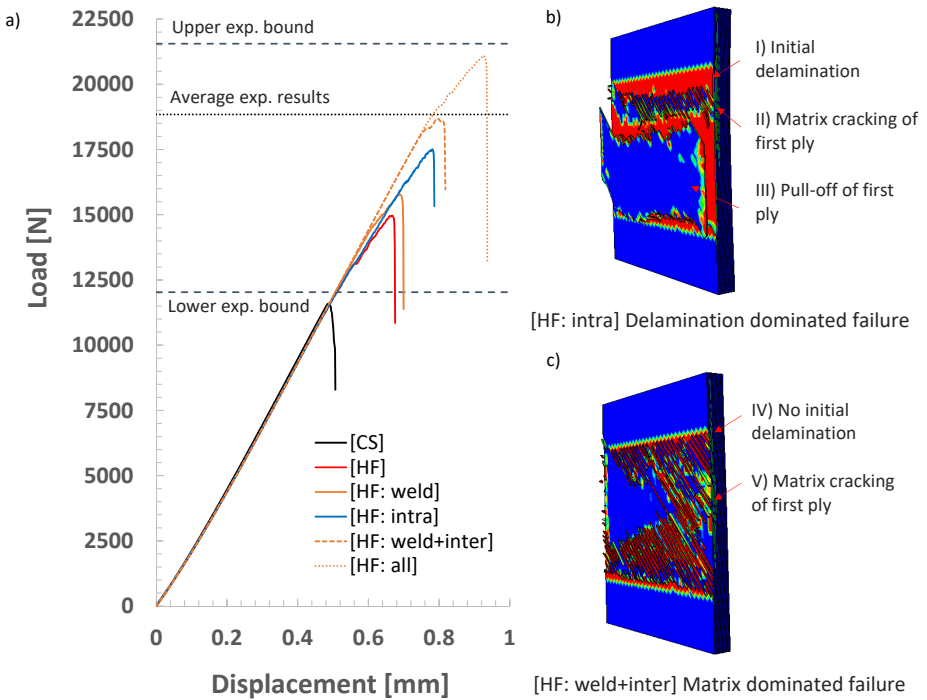
Figure 4.4.5: Influence of inter- and intralaminar material properties: a) Load-displacement curves; b) Example of delamination dominated failure mode; c) Example of matrix dominated failure mode. *CS* - Simplified Continuum Shell model, *HF* - High-fidelity model, *HF: weld* - Increased weld toughness, *HF: intra* - Increased intralaminar matrix-dominated fracture toughness, *HF: weld+inter* - Increased weld and interlaminar fracture toughness, *HF: all* - Increased weld, intra- and interlaminar fracture toughness.

The *CS* and *HF* models are the models considered in the previous sections and are the simplified continuum shell and high-fidelity model, respectively. The *HF: weld* model is the high-fidelity model with an increased fracture toughness at the welded interface. A factor of 2.5 is chosen based on the prediction of the average experimental results by using

the simplified approach. This brings the joint strength to 15776 N, which is much less compared to scaling the weld fracture toughness in the simplified approach. This difference between the simplified and high-fidelity approach is explained by the change in failure mode to matrix cracking and failure of the first ply. Interestingly, this also suggests that having increased material properties at only the welded interface cannot explain the upper bound experimental results. If only the matrix fracture toughness of the ply (*HF: intra*) is increased the failure mode becomes delamination dominated, as shown in Figure 4.4.5b. Delaminations initiate (I) at the same level as the HF model and migrate through matrix damage (II) to the first ply and eventually pull-off (III) the first ply. Due to the increased matrix fracture toughness the load is increased from 14962 N to 17509 N. When both, the interlaminar fracture toughness of the first ply and the weld (*HF weld+inter*), are modified, the strength further increases to 18685 N and a more ply dominated failure mode, as shown in Figure 4.4.5c, is observed. In this situation, there are no signs of initial delaminations (IV) and failure of the joint is caused by matrix failure (IV) of the first ply. The strength can be even further increased if the fracture toughness of all adjacent plies and interfaces is increased (*HF: all*).

The under-prediction of the numerical simulations cannot be attributed only to the properties of the weld and of the plies, and require further analysis on the damage development and assumption of the numerical model. When taking a closer look at matrix failure of the ply, it is observed that the loading of the matrix cracks changes as damage progresses. Matrix damage and welded interface initiation is mostly due to in-plane shear loading with some influence of mode I opening due to secondary bending, but as damage progresses the cracks become predominately loaded in out-of-plane shear (Figure 4.4.6a) and element deletion is triggered when 100 percent out-of-plane shear is reached. This identifies one of the limitation of the current modelling approach. Changes in loading mode of existing in-plane cracks, changes in crack angles of partially developed cracks and possible effects of friction due to crack closure are not taken into account. The influence of these effects may effectively delay the propagation of damage and significantly increase the strength of the matrix dominated failure modes.
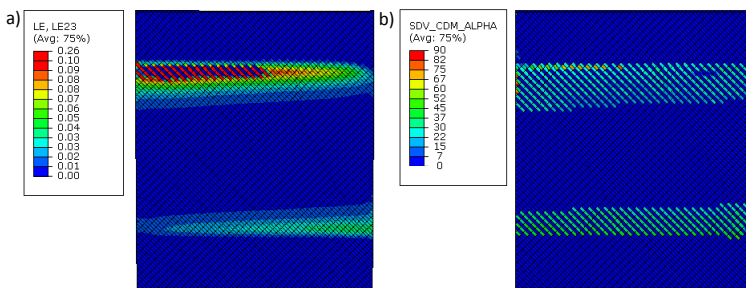

Figure 4.4.6: Analysis of intralaminar behavior: a) Excessive out-of-plane shear strains; b) Non-zero matrix crack angles.

Although the modelling strategy is already able to limit the delamination growth due to damage and softening of the plies, it is also observed that the predicted crack angles for matrix damage are generally between 20 and 45 degrees as shown in Figure 4.4.6b, where a 0 degree crack represents a pure in-plane matrix crack [46] or no damage initiation. At some locations near the start of the fully developed ply splits the angles are closer to in-plane failure while at most other locations they are at the lower angles, which supports the experimentally observed migration of delamination to the second interface. As the current modelling approach is using the Abaqus/Explicit built-in failure criteria, there is no control in preventing failure of the welded interface when crack migration is detected.

Another important consideration is that the bending stiffness of the laminate will influence secondary bending of the welded joint and will change the local mode mixity at the welded interface. This means that a more stiff or hard laminate will experience less secondary bending and a mode II induced failure mode. Secondary bending is higher for soft laminates and will result in a higher mode I component at the welded interface. Furthermore, since the joint strength appears to be highly influenced by the matrix dominated failure modes of not only the weld but also the composite laminate, it is evident that the interface angle and ply orientation near the weld plays an important role for the strength of the joint. These effects may have to be considered when establishing design guidelines for composite welded joints.

4.5 Conclusions
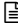
Single lap shear thermoplastic composites welded joints have been designed, manufactured and tested. Evaluation of the experimental results provided new insights into the complex failure behavior of the joint and of the interaction with the failure modes of the laminate. For the numerical analysis both a simplified and a high-fidelity approach are developed and evaluated. It is found that the simplified approach, based on the cohesive zone method, predicts a very conservative joint strength when unidirectional interlaminar fracture toughness properties are used. The apparent fracture toughness of the joints is found to be approximately 2.5 times higher. A high-fidelity modelling approach is developed to investigate the influence of the complex failure behavior of the welded joint using an improved Continuum Damage Model to accurately predict matrix failure and ply splitting. This model provides new insights in the failure behavior of the joint and is able to accurately predict the failure mode. However, predicting the upper bound experimental results is still difficult and some limitations to the numerical methodology are identified. This includes changes in mode-mixity during crack propagation, non-zero matrix crack angles near the welded interface and not considering frictional effects on the fracture plane. The analysis using the high-fidelity model shows that different material properties for the inter- and intralaminar failure modes have a strong effect on the joint strength and may significantly influence the failure modes. A better understanding of the material properties of the welded joint is still needed and design guidelines may need to not only consider the welded interface but also the surrounding plies.

5

CHARACTERIZATION AND ANALYSIS OF CONDUCTION WELDED THERMOPLASTIC COMPOSITE JOINTS CONSIDERING THE INFLUENCE OF MANUFACTURING

Thermoplastic composite welding is a key technology that can help to make the aviation industry more sustainable, while at the same time enable high-volume production and cost-efficient manufacturing. In this work, characterization, testing and analyse of thermoplastic composite conduction welded joints are performed accounting for the influence of the manufacturing process. Test specimens are designed from welds of a half a meter long welding tool that is developed to weld the stiffened structures of the next-generation thermoplastic composite fuselage. In the design, special attention is paid to the weldability of the laminates, while ensuring fracture occurs only at the welded interface. Two specimen configurations are evaluated for the Double Cantilever Beam and End-Notched Flexure characterization tests. Moreover, Single Lap-Shear specimens are tested in tension and in three-point-bending. Finally, the characterized material properties are introduced in finite element analyses to demonstrate that the cohesive zone modeling approach can be used to conservatively predict the strength of these welded joints. New insights are obtained in the relation between the manufacturing process, the quality of the weld and the mechanical properties of the joints, which are significantly different compared to autoclave consolidated composites.

5.1 Introduction

The use of thermoplastic composite materials can substantially increase the sustainability of the aviation sector through achieving a paradigm shift in aircraft manufacturing. Thermoplastic composites may enable such a shift and can offer improved mechanical properties, 'unlimited' shelf life and provide a number of advantages that can benefit cost-efficient and high-volume manufacturing. One of the recent advancements as part of the EU's Clean Sky 2 initiative is the Multi-Functional Fuselage Demonstrator (MFFD) [15, 114–116]. This demonstrator gives a glimpse of what a next-generation aircraft could be and makes use of new joining techniques such as thermoplastic welding. Compared to typical manufacturing processes such as autoclave-, oven- and press-consolidation, thermoplastic welding can achieve much shorter processing times (seconds to minutes). The most established thermoplastic welding techniques are induction, ultrasonic and resistance welding [1]. Another method of joining thermoplastic composites is conduction welding, currently under development at Fokker/GKN Aerospace [9] and patented [10].

One of the main benefits of thermoplastic welding is that it reduces the amount of mechanical fasteners required. However, introducing these fastener-free joints also comes with new challenges such that the strength of the structure becomes more reliant on the properties of the thermoplastic matrix material [12, 21]. Furthermore, these properties may also be influenced by the welding process parameters. For composite fuselages, skin-stiffener separation [117–119] is one of the most common failure modes [115, 120], which makes the strength of these new fastener-free joints especially important.

A common methods to test the strength of thermoplastic composite welded joints is by means of Single Lap-Shear (SLS) joints. These specimens are straightforward to manufacture and test, and are often used as a tool to determine the strength and quality of welded joints [121, 122]. There is no specific standard for composite welded joints, therefore researchers typically make use of the test standards of metallic (e.g., ASTM D1002 [123]) or laminated (e.g., ASTM D3165 [110], ASTM D5868 [124]) bonded joints. Other methods to test composite welded joints are for example double-lap shear and pull-through [104], interlaminar shear strength [125] and three-point bending [126]. All of these tests may be used to compare strength values for a specific configuration, but just as the SLS test, they only provide an apparent strength value, and do not provide direct material property values that can be used in a general analysis method to predict different designs. The joint typically fails under mixed-mode (combined peel and shear) loading condition, which makes it generally highly dependent on the configuration, geometry, boundary conditions and secondary bending effects [127, 128]. Furthermore, when joining composite laminates, Tijs et al. [12] showed that the failure mechanisms such as matrix cracks and delaminations [59] in the surrounding plies near the welded joint play an important role in the strength and failure behavior of the welded joint. It is also shown that the apparent fracture toughness of the welded joint is a factor 2.5 higher compared to the autoclave consolidated fracture toughness [21], which suggests that the welding process may locally affect the material properties [129].

Manufacturing process parameters that may influence the material properties of the thermoplastic material and welded joint are local temperature gradients, heat-up speed, constant time and temperature at the welded interface. These parameters may affect the flow [107] of the polymer, the melting conditions, the crystallization kinetics or may significantly

influence the final crystallinity of the material [67]. Furthermore, the welding process may introduce thermal residual stress due to both the high temperature and shrinkage of the material during crystallization. Sacchetti et al. [108] showed that the fracture toughness of thermoplastic composites may significantly increase during high cooldown rates, which can be explained by a limited amount of crystallization of the semi-crystalline polymer, making the material more ductile. Other thermoplastic polymers, such as the fast-crystallizing Poly(Ether-Ketone-Ketone) thermoplastic polymer (PEKK-FC) [67], achieve full crystallization (approximately 30%) even at cooldown rates up to -60 °C/min. However, the manufacturing process parameters for heating and cooldown during welding may be much faster. Furthermore, a thick interface or resin pockets may also play an important role [66] on the fracture behavior and toughness as it allows for more plastic deformation at the crack tip. The material fracture properties of thermoplastic welded composites can not be directly derived from single lap-shear tests due to mixed-mode loading conditions as previously discussed. Researchers have instead used autoclave consolidation to study the key parameters such as temperature, pressure and time that govern the joining process [130]. Furthermore, for some welding methods such as ultrasonic welding Double Cantilever Beam (DCB) and End-Notched Flexure (ENF) tests were manufactured to characterize the pure mode I and II fracture toughness [129]. For ultrasonic welding, the use of energy directors may allow for welding of unidirectional (UD) plies, however for other methods such as conduction welding this is very difficult due to the difference in thermal conductivity in longitudinal and transverse direction of the UD plies.

The characterized fracture properties can be used in analysis methods by means of the Cohesive Zone Model (CZM). The main benefit of this methodology is that it can predict both the onset and propagation of damage, without the need to define an initial flaw as required for virtual crack closure techniques [120, 131]. The CZM methodology has been used extensively already to evaluate the strength of adhesively bonded joints [101–103], delaminations [76] and more recently also on thermoplastic composite welded joints [12]. The CZM approach can also account for changes in the mechanical behavior of the interface, for example plasticity or fiber bridging, which are found to have a significant influence on the total amount of dissipated energy during fracture as shown by Tijs et al. [21].

Considering the aforementioned challenges, it is therefore needed to characterize and analyse the fracture behavior of thermoplastic conduction welded joints taking into account also the influence of the welding manufacturing process parameters on the weld quality and mechanical properties of the joints. The link between design, manufacturing and the analysis methodology is considered to be of high importance in the design and certification of the new fastener-free thermoplastic composite structures.

In this work, the characterization and analysis of thermoplastic composite conduction welded joints is performed accounting for the influence of the manufacturing process. DCB, ENF and SLS specimens are welded by means of a half a meter long welding tool, representative of the process used to weld stiffened structures of the next-generation thermoplastic composite fuselage. During the design of the specimens, special attention is paid to the weldability of the laminates, while ensuring that fracture occurs only at the welded interface. For the design of the fracture toughness characterization specimens, two configurations are designed and tested. The welded joints are also tested during different

loading conditions by means of SLS specimens in tension and three-point-bending. Finally, the characterized material properties are used in numerical analyses to evaluate if the cohesive zone modeling approach can be used to reliably predict the strength of these welded joint and to validate the proposed methodology.

5.2 Conduction welding the next-generation thermoplastic composite fuselage

The MFFD is a 8.5 meter long thermoplastic composite-made fuselage demonstrator that is 4 meter in diameter. The main objective of the MFFD is to demonstrate the benefits of integrating various functions such as passenger/cargo transport, electrical/mechanical/hydraulic systems, interior as well as load carrying capability [114]. The MFFD is stiffened by means of omega profiles which are joined to the skin through conduction welding. Figure 5.2.1 shows an overview of the stiffened skin (5.2.1a) with close-ups of the welding tool (5.2.1b) and the welded omega stiffener (5.2.1c).
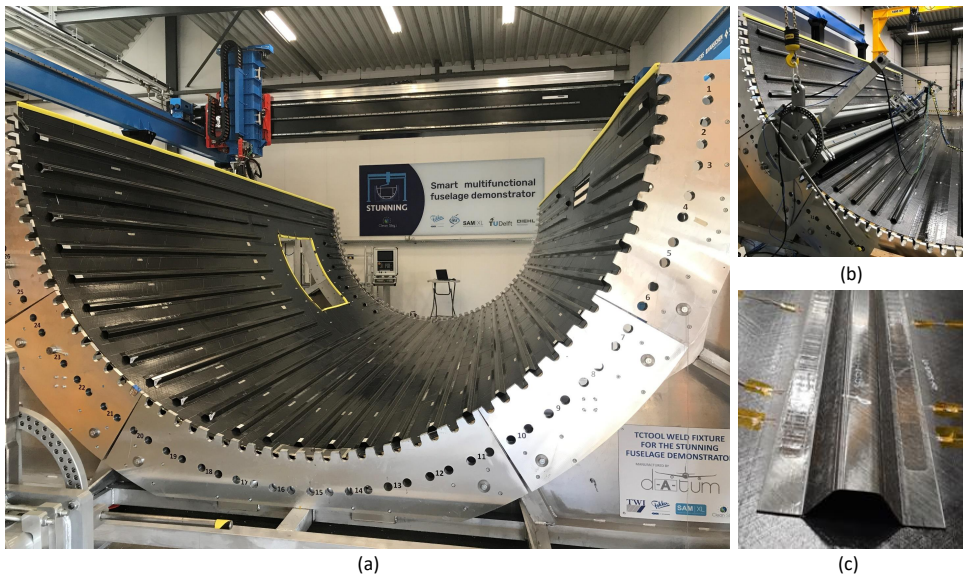
Figure 5.2.1: Multi-Functional Fuselage Demonstrator: a) omega stiffened skin structure; b) welding tooling; c) close-up welded omega stiffener.

The conduction welding process is based on locally heating the surface of the part as shown in Figure 5.2.2a. The tool generates the weld bath by heat conduction from the stamp at the top through the laminate and heat is applied until the laminates are locally melted at their interface. Pressure is applied during heating and this force is reacted by the anvil on the opposite side of the stamp. The weld tooling consists of both stamps and heatsinks. The tooling design [10] can accommodate for changes in laminate thickness along the weld direction. Conduction welding is therefore suitable and scalable for welding of large aeronautical parts and can easily take care of absorbing manufacturing tolerances like

gaps. Another benefit of conduction welding is that it does not require addition of welding specific materials such as energy directors or conductive strips. The manufacturing process cycle of conduction follows the same principle as autoclave consolidation, but at a much shorter time span. A typical process cycle is shown in Figure 5.2.2b and consists of a heat-up, consolidation and cooldown phase. It is aimed to reach the consolidation phase, also referred to as constant-time, as quickly as possible to shorten the process cycle. The implication is, that in order to reach the required melting temperature at the welded interface, a higher temperature is applied at the stamp side. This temperature needs to be high enough to allow for a quick process cycle, but low enough not to damage the material near the stamp.
In this work, several welding process cycles are defined to study the influence on the

(a)

(b)
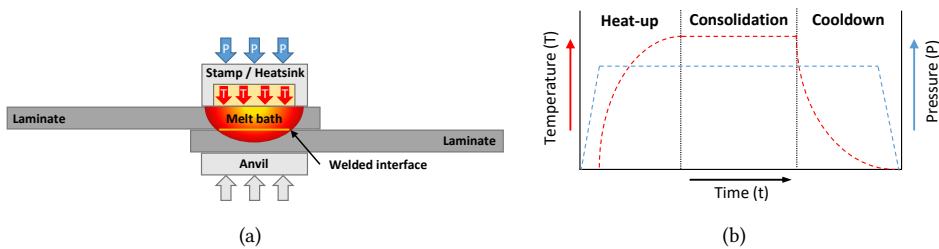
Figure 5.2.2: Conduction welding process: a) Schematic; b) Typical manufacturing process cycle.

weld quality and mechanical properties. The temperature during welding is monitored by means of several thermocouples at the top, bottom and weld interface along the width of the 0.5 meter tool. Two different studies were performed, namely the (I) influence of welding temperature and (II) the influence of cooldown method. For the first study, the characterization specimens were welded at four different weld interface temperatures in steps of 25 °C: (1) ~325 °C, (2) ~350 °C, (3) ~375 °C and (4) 375+ °C. The temperatures are indicated as approximate, as some variation in temperature is observed along the length of the weld. The lowest temperature is way below the typical autoclave consolidation temperature of ~375 °C [21, 67], but it is observed in the thermocouple data that the onset of melting is likely around this temperature. In the evaluation the temperatures (2), (3) and (4) are referred to as cold, typical and hot temperature, respectively. However, during characterization it is found that the lowest temperature (1) provided a kissing joint and not a weld, therefore the single lap shear tests were welded only at cold, typical and hot temperature. The constant-time is kept consistent for all welds. For the cooldown phase during the first study a constant cooldown is chosen. During the second study three different methods of cooldown are evaluated: (a) free cooldown, (b) controlled cooldown, and (c) stepped cooldown. Free cooldown resulted in the fastest process cycle. During stepped cooldown, the generator is turned off to cool down freely up to the crystallization temperature of approximately 275 °C [67] after which the temperature is kept constant at this temperature for a certain amount of time. In order to have consistency between different welds, a pre-heating step is introduced to warm up the tooling and the specimens prior to starting the welding process. Further details on the welding recipes are considered proprietary information and not provided.

5.3 Design and manufacturing of conduction welded joint specimens

An overview of the welded joint specimens is shown in Figure 5.3.1. Characterization of the welded fracture toughness is performed in mode I by means of the DCB test, while the mode II fracture toughness is characterized using the ENF test as shown in Figure 5.3.1a. The specimens are designed to closely match the geometry and manufacturing process of the thermoplastic composite fuselage structure and are chosen to be representative of a skin-stringer flange. The welded laminates follow the typical dimensions of the flange and are 30 mm wide. Furthermore, the layup of the laminates is chosen to be quasi-isotropic as it has proven to be difficult to weld unidirectional (UD) laminates. However, the welded interface of the quasi-isotropic laminates is chosen to be 0/0-degree to ensure that fracture only occurs in the welded interface and that no secondary failure modes in the surrounding plies occur [12].
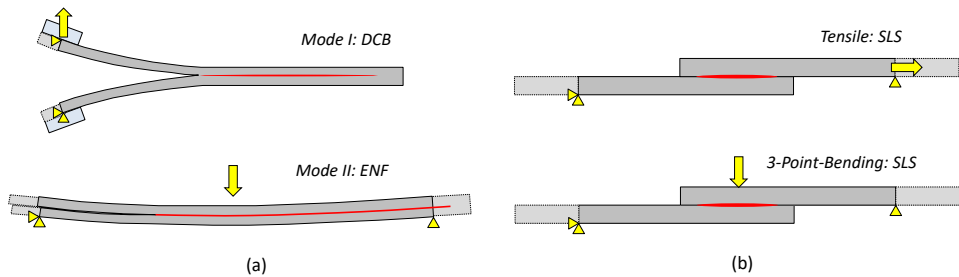
Figure 5.3.1: Characterization and validation tests of conduction welded joints: a) characterization, DCB and ENF; b) validation, SLS tensile and 3PB.

The welded joints are also tested during different loading conditions by means of SLS specimens in tension and three-point-bending as shown in Figure 5.3.1b. These tests are conducted to validate the use of the characterized material properties in the analysis.

5.3.1 Material properties

The material used in this work is the thermoplastic composite Solvay APC(PEKK-FC) thermoplastic polymer prepreg [67]. The fiber of the prepreg is the continuous unidirectional AS4D fiber and the nominal ply thickness is 0.14 mm. Manufacturing of the laminates that are welded is performed by means of autoclave consolidation. The autoclave process cycle is chosen to be representative for large aeronautical parts, which means a long cycle with a constant phase and slow cooldown speed is used. The mechanical properties of the AS4D/PEKK-FC thermoplastic composite material are provided in [12] and the relevant properties that are used in this research are summarized in Table 5.3.1. The properties are measured at room temperature ambient conditions.

Table 5.3.1: AS4D/PEKK-FC thermoplastic composite properties [12, 21]

Property	Description	Value	Unit
E_{1t}	Young's modulus, longitudinal tensile direction	138300	MPa
E_{1c}	Young's modulus, longitudinal compressive direction	128000	MPa
E_{2t}	Young's modulus, transverse tensile direction	10400	MPa
E_{2c}	Young's modulus, transverse compressive direction	11500	MPa
$G_{12}=G_{13}$	Shear modulus	5190	MPa
ν_{12}	Poisson ratio, 1-2 direction	0.316	-
ν_{23}	Poisson ratio, 2-3 direction	0.487	-
G_{Ic_p}	Mode I matrix fracture toughness, propagation	1.12	kJ/m^2
G_{IIc_p}	Mode II matrix fracture toughness, propagation	2.35	kJ/m^2
η	Benzeggagh-Kenane coefficient	2.9	-
Y_T	Matrix tensile strength	87	MPa
$S_{L_{0.2\%}}$	Matrix 0.2% offset shear strength (estimated)	50	MPa
$S_{L_{0.5\%}}$	Matrix 0.5% offset shear strength (estimated)	60	MPa
$S_{L_{5\%}}$	Matrix 5% offset shear strength	90	MPa

5.3.2 Specimen design

Two AS4D/PEKK-FC laminates that consists of 16 unidirectional plies each are manufactured by autoclave consolidation. The laminates are Quasi-Isotropic (QI) [0/45/90/-45/0/-45/90/45]$_S$ with the 0 direction in the length of the laminate and are welded on the 0/0-degree interface. For the characterization specimens (DCB and ENF), 540 mm long strips, 30 mm wide, are machined and are placed on top of each other as shown in Figure 5.3.2a in the welding tool. In the center of welded laminates a 125 mm wide UPILEX foil with a thickness of 12.5 μm is placed as insert to start the crack. The UPILEX foil is pre-treated with release agent. The benefit is that a very thin single insert can be used, thus guaranteeing a sharp as possible initial crack tip [21]. Two characterization (DCB or ENF) specimens are cut from a single weld.

The full length laminates are cut in half to create two test specimens and are each machined to a length of 225 mm, with an initial insert length of 60 mm. This specimen size means that the specimens are long enough to test both the mode I and II fracture toughness on the same specimen, or several tests on the same specimens, which is convenient during this research to develop the methodology. However, for actual characterisation tests, it is recommended to only perform a small pre-crack to ensure that the crack front remains straight and without a fully developed fracture process zone [21]. After welding, the specimens are machined to a typical specimen width of 25 mm for the full weld specimens and 12.7 mm for the weld center specimens as shown in Figure 5.3.2b. The width of 12.7 mm for the center specimens is chosen as the typical width of the welded interface is in the range of 14 to 18 mm, depending on the weld temperature. Cutting at the center of the weld for the weld center specimens is shown in 5.3.2c. The SLS specimens are machined from two 540 mm long laminates that are welded on the overlap as shown in 5.3.3a. The 0-degree direction is in the load direction of the specimen, so the welded interface is 0/0-degree. The specimen design of SLS specimens as shown in Figure 5.3.3 follows ASTM standard D3165 [110], with a total length of 120 mm an overlap length of 30 mm and nominal width of 25 mm.

(a)

(b)

(c)
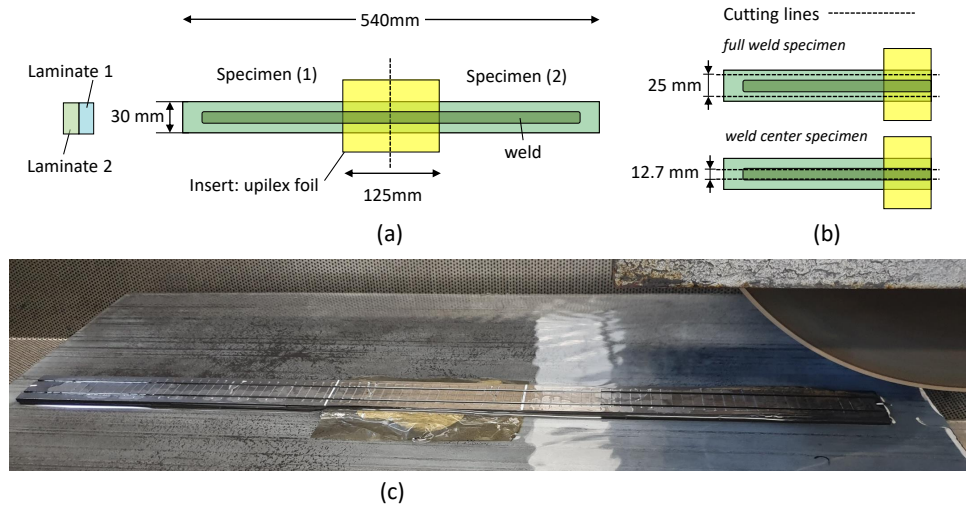
Figure 5.3.2: Welded joint characterization specimens: a) Welded laminates with upilex foil insert; b) Full weld and center weld specimen design; c) Machining of center weld specimens.
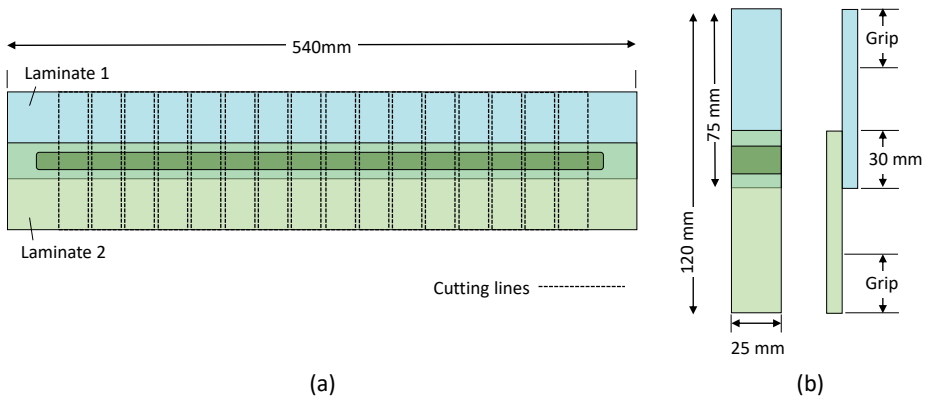

(a)

(b)

Figure 5.3.3: Welded joint validation specimen: a) Welded laminates and SLS cutting scheme; b) SLS specimen dimensions.

5.3.3 Non destructive inspection of conduction welded joints

Prior to machining the specimen, the quality of the weld is inspected by a Non Destructive Inspection (NDI) approach [12]. This system utilizes a phased array setup that can map the quality of the conduction weld through the thickness. The equipment used is the Omniscan MX scanner with ultrasonic probe. The NDI system can perform A-scan, C-scans and S-scans to provide information about the weld quality through the thickness and along the weld direction. Some typical NDI C-scan results are shown in Figure 5.3.4, where the colors represent the damping of the sound. The color red is 100% and blue is 0% attenuation of the ultrasonic sound waves. The NDI results presented are from scanning the full length (540 mm) welded laminates and provide a top view of indications through the thickness. The red area is typically air at the edges of the weld and at the upilex interface.

(a)

(b)

(c)
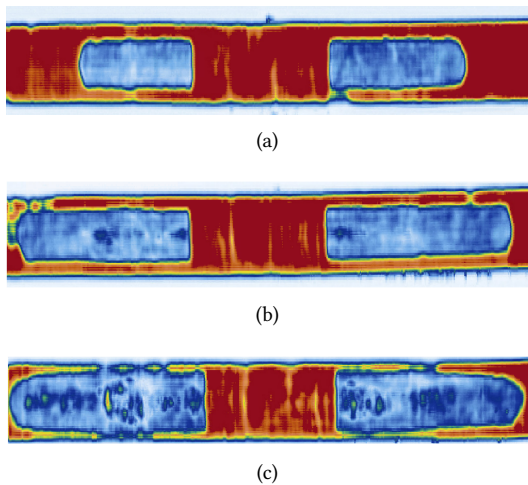
Figure 5.3.4: NDI results: a) Partial (kissing) joint; b) Typical weld; c) Overheated specimen with defects and edge delamination.

If is found that the very low temperature (~325 °C) welds showed a partial joint as shown in Figure 5.3.4a, while the typical (~375 °C, Figure 5.3.4b) welds are joined along nearly the full length. It is interesting to note that from only the C-scan results it is difficult to determine the difference between the kissing and the normal weld, however the quality may be guaranteed if also the temperature and pressure are monitored. During testing it is confirmed that the specimens from Figure 5.3.4a were indeed a kissing joint. It is also noted that very high temperatures may cause some (local) overheating. This resulted in more NDI indications and in some cases melting of the full specimen width, resulting in delaminations at the edges of the specimens as can be seen in Figure 5.3.4c. Therefore, when welding at high temperatures, for example welding thick laminates, the specimen width may need to be increases to prevent this. Furthermore, this also resulted in local impressions in the laminate. From the NDI inspection it is concluded that slightly wider specimens and a more gradual temperature ramp up would likely improve the weld quality, but the welds are considered of sufficient quality for the purpose of developing the characterization and analysis approach.

5.4 Methodology

The conduction welded joints are characterized, tested and analyzed. Testing is performed at Delft University of Technology (TU Delft). All the experiments are monitored by both a crack monitoring camera and Digital Image Correlation (DIC) system. For the numerical analysis, Abaqus commercial finite element software [45] is used.

5.4.1 Welded double cantilever beam test

The Double Cantilever Beam (DCB) test is performed to characterize the pure mode I fracture toughness of the welded interface. The test configuration of the DCB test with geometrical parameters is shown in Figure 5.4.1a. The DCB tests follow the ISO 15024 test standard [89] and loading blocks are used to load the specimens. The crack length during the propagation tests is closely monitored by means of a crack monitoring camera and a Digital Image Correlation (DIC) system as shown in Figure 5.4.1b. The specimens are tested on a tensile testing machine, at a displacement rate of 0.5 mm/min.

| (a) | (b) |
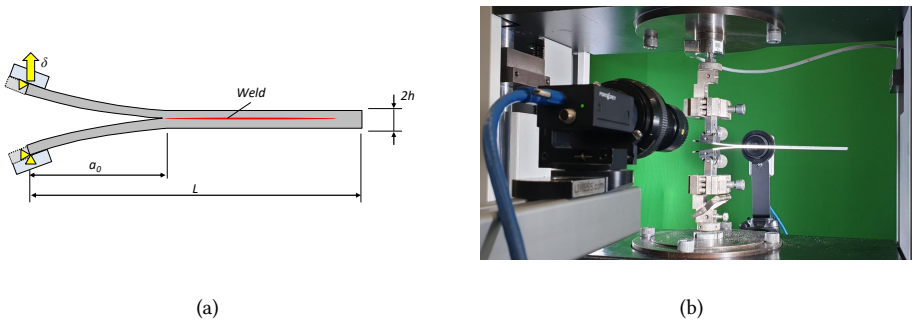
Figure 5.4.1: DCB test at TU Delft: a) Geometrical parameters; b) Test setup with crack monitoring camera and DIC system.

The initial crack length (a_0) for each configuration is determined by means of a compliance calibration procedure. This is done to ensure that the compliance of the QI welded specimens match the UD tests on autoclave consolidated specimens performed by Tijs et al. [21] so that the load-displacement curves can be easily compared. The compliance calibration procedure consists of the following steps. First, different initial crack lengths as shown in Figure 5.4.2a are tested in the elastic region of the load-displacement curve and the compliance is measured. Secondly, the compliance for each test is plotted in a graph as shown in 5.4.2b and a line is fitted. The slope (m) and intercept (n) can then be used to determine the crack length correction factor (Δ) at $C^{1/3} = 0$ as illustrated in Figure 5.4.2b. This parameter can also be determined as $\Delta = n/m$. The crack length that would result in the same compliance for each configuration can now be determined from Figure 5.4.2b or calculated from $\frac{C^{1/3} - n}{m} = a$. These steps are repeated for each configuration and the resulting parameters are summarized in Table 5.4.1, where L_0 is the distance to the front of the loading blocks.

The Corrected Beam Theory (CBT) is used for the experimental data reduction method

Figure 5.4.2: Compliance calibration methodology: a) DCB configuration at different crack lengths; b) Compliance calibration procedure and results.

Table 5.4.1: Compliance calibration parameters of the difference DCB specimens.

Configuration	a_0	L_0	m	n	Δ
Autoclave UD: 25mm	47.4	59.9	0.006060	0.055641	9.18
Full weld QI: 25mm	44.3	56.8	0.006908	0.036918	5.34
Weld center QI: 12.7mm	36.2	48.7	0.008594	0.032224	3.75

and follows the ISO 15024 test standard [89]. Following this method, the critical mode I energy rate G_{IC} is:

$$G_{IC} = \frac{3P\delta}{2b(a+\Delta)}\left(\frac{F}{N}\right) \tag{5.1}$$

where

$$F = 1 - \frac{3}{10}\left(\frac{\delta}{a}\right)^2 - \frac{3}{2}\left(\frac{\delta l_1}{a^2}\right) \tag{5.2}$$

$$N = 1 - \left(\frac{l_2}{a}\right)^3 - \frac{9}{8}\left[1 - \left(\frac{l_2}{a}\right)^2\right]\left(\frac{\delta l_1}{a^2}\right) - \frac{9}{35}\left(\frac{\delta}{a}\right)^2 \tag{5.3}$$

where P and δ are the load and displacement, a is the total crack length during crack propagation and b is the specimen width. The factor F corrects for large displacement, N corrects for stiffening of the specimen by the loading blocks and Δ is determined by the compliance calibration approach. l_1 and l_2 are distances to the loading pin centre, as described by the test standard [89].

5.4.2 WELDED END-NOTCHED FLEXURE TEST

The End-Notched Flexure (ENF) test [92], consists of a three point bending setup of a welded specimen that has a pre-crack at one of its ends. The test is standardized in ASTM D7905 / D7905M [84] and is commonly used due to its simplicity to characterize the mode II fracture toughness. Figure 5.4.3a shows the geometrical parameters of the ENF test and Figure 5.4.3b shows the test setup with crack monitoring camera and DIC system.   A

(a)   (b)
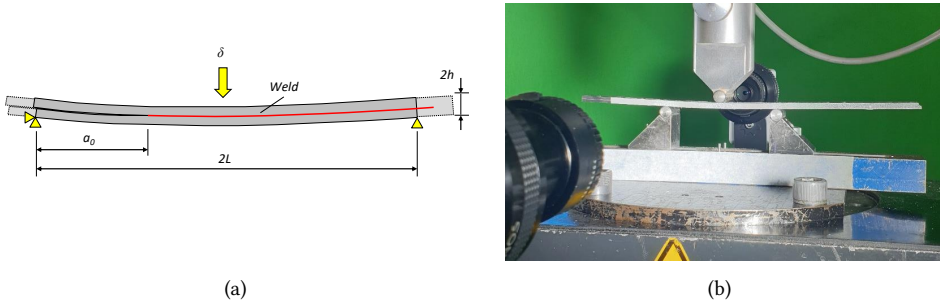
Figure 5.4.3: ENF test at TU Delft: a) Geometrical parameters; b) Test setup with crack monitoring camera and DIC system.

compliance calibration approach, based on the test standard [84] is used to determine the test setup parameters for the different configurations. The approach is shown in Figure 5.4.4a and consists of testing the compliance of specimens at different crack lengths (a_0) and spans ($2L$). The compliance of each test is then plotted against a^3, as presented in Figure 5.4.4b and a trendline is constructed. The slope, m, and intercept, A, of this trendline can then be used in the data reduction method to calculate the mode II fracture toughness. When the proposed method is used to characterize different welded laminates and layups, special attention needs to be paid to selecting a configuration that will ensure stable crack propagation. This is achieved by following the guidelines from Tijs et al. [21], which is briefly explained below.

It appeared not to be feasible to test each configuration at the same compliance while also respecting the above mentioned guidelines. It is found that testing the ENF specimens in a compliance range of 0.003 to 0.004 provides good results, if at the same time, the available crack growth length, $L_{cg} > 20$ mm, and a stability limit, $a_0/L > 0.55$ is respected. Several spans and crack lengths were tested to investigate the best setup and the parameters of the configurations selected in this study are presented in Table 5.4.2.

The following equations are used in the data reduction method to determine the mode II fracture toughness G_{IIC} [84]:

$$G_{IIC} = \frac{3mP^2a^2}{2b} \tag{5.4}$$

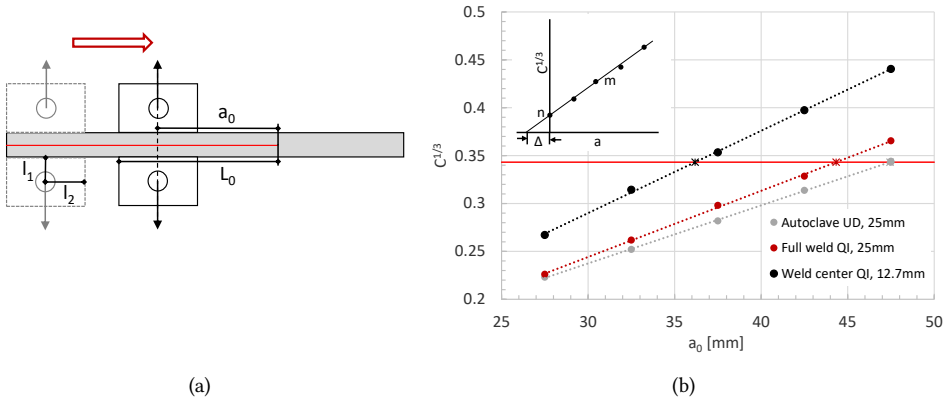$$a_{calc} = \left(\frac{C-A}{m}\right)^{\frac{1}{3}} \tag{5.5}$$
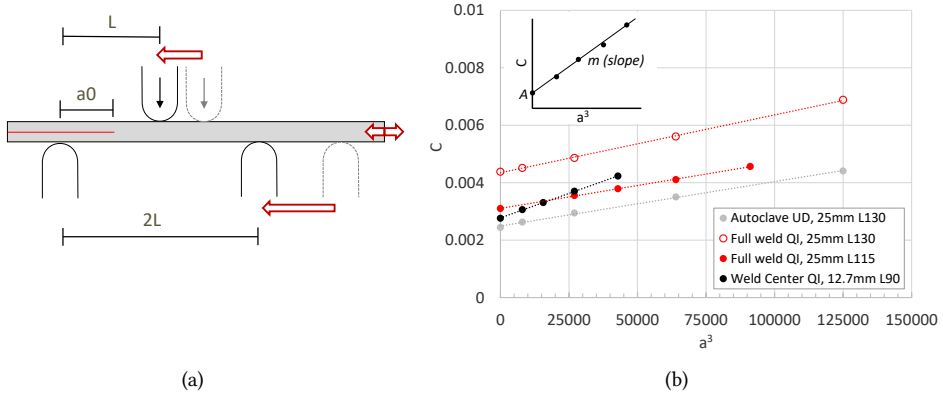
Figure 5.4.4: Compliance calibration methodology: a) ENF configuration at different crack lengths; b) Compliance calibration procedure and results.

where C can be determined for each point along the load-displacement curve ($C = \delta/P$) or calculated from:

$$C = A + ma^3 \qquad (5.6)$$

Table 5.4.2: Compliance calibration parameters of the difference ENF specimens and configurations.

Configuration	b	$2L$ (span)	m	A	a_0	a_0/L	L_{cg}
	$[mm]$	$[mm]$	$[\text{-}]$	$[\text{-}]$	$[mm]$	$[mm]$	$[\text{-}]$
Autoclave UD	25.0	130	1.546E-08	2.493E-03	45.0	0.69	20
Full weld QI	25.0	130	2.013E-08	4.347E-03	40.0	0.62	25
Full weld QI	25.0	115	1.594E-08	3.105E-03	33.5	0.58	24
Weld Center QI	12.7	90	3.407E-08	2.775E-03	25.0	0.56	20

5.4.3 Welded single lap shear tensile test

Static tensile SLS tests are performed according to ASTM D3165 [110] until failure. This test is performed as validation for the analysis approach. The tests are carried out using a ZWICK 250kN universal test machine with hydraulic grips. The specimen size is small compared to the grip size, so a short gripping length (L_{grip}) is used and set to 35 mm. The hydraulic grips allow for an offset in gripping position so that bounding of tabs is not required to prevent secondary bending due to clamping. Due to the small specimen size, the cross-head speed is set to 0.1 mm/min and a clamping pressure of 100 bar is used to prevent slippage. The testing machine automatically adjusts the displacements to account for compressive forces in the specimen due to clamping. DIC pictures of the specimens were taken before and after clamping to account for pre-stressing due to clamping. Figure 5.4.5a shows the geometrical parameters of the SLS test. One side of the specimen is speckled for DIC and the other side of the specimen is marked as shown in Figure 5.4.5b to visually follow the crack tip. Markings are placed starting from the edge of the weld stamp, which is a few millimeters wider compared to the width of the welded interface (w_{weld}) due to the thermal gradient through the thickness of the conduction weld. DIC is also used to evaluate the specimen deformation and for comparison against the measured load-displacement curves which include the compliance of testing machine.

(a)   (b)
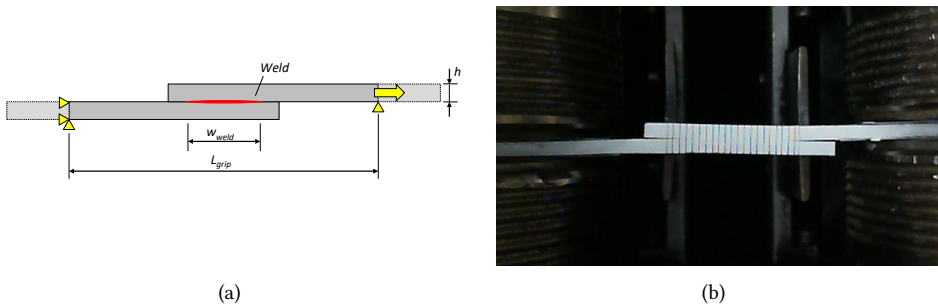
Figure 5.4.5: SLS tensile test at TU Delft: a) Geometrical parameters; b) Close-up of SLS specimen in hydraulic grips.

5.4.4 Welded single lap Shear 3-point bending test

Three-point-bending tests are performed on the single lap shear specimens (SLS-3PB) on a test fixture according to procedure A of ASTM D7264 [132]. The aim is to load the welded joint in a different conditions compared to the tensile test, in order to validate the analysis approach for a different loading condition. The specimens are positioned at the center of the overlap, which might have a slight mismatch with the center of the weld, due to inaccuracy in the actual weld position. The geometrical parameters of the 3PB test are given in Figure 5.4.6a. Typically, this test is performed on flat laminates with leveled rollers. Therefore, for the single lap shear joints one of the rollers is shimmed by using a laminate of the same thickness as the one of the single lap shear specimen arms as shown in Figure 5.4.6b. The span ($2L$) is set to 60 mm and a loading speed of 1 mm/min is used. The same crack monitoring system and DIC setup are used as the other tests.
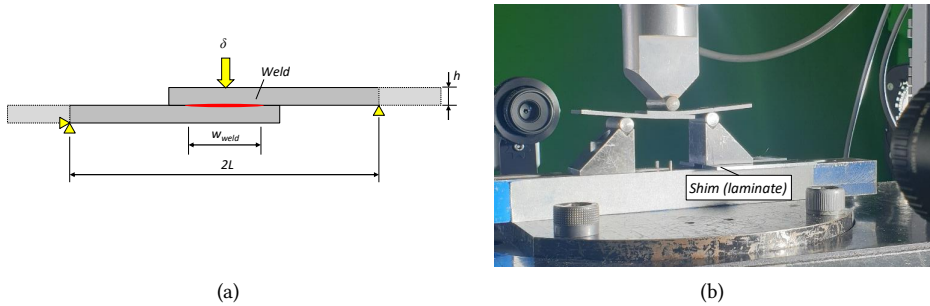
Figure 5.4.6: SLS-3PB test at TU Delft: a) Geometrical parameters; b) Test setup with crack monitoring camera and DIC system.

5.4.5 Finite element model

The experimental results are compared to a numerical model of the welded joints using the built-in functionality of the Abaqus commercial finite element software. Finite element analysis are used instead of analytical solutions, because the test coupons are non-standard compared to the typical UD specimens with full-width interface. The welded interface of the full weld specimen as shown in Figure 5.3.2b has a partial weld width compared to weld center specimens and both specimens have a QI layup. The geometry, boundary conditions and loading of the models follows the dimension shown in Figure 5.4.1a (DCB), Figure 5.4.3a (ENF), Figure 5.4.5a (SLS tensile) and Figure 5.4.6 (SLS-3PB). The numerical models are discretised with through-thickness continuum shell elements (SC8R) and consider only linear-elastic material behavior. Composite layups are used to define the sections. For the Young's modulus E_{11} and E_{22}, the average of tension and compression from Table 5.3.1 are used. The welded interface is modelled through the surface based contact algorithm available in Abaqus, which accounts for the kinematics of surface contact, cohesive separations and friction [12]. The mesh size is adjusted to meet the requirements [99] for cohesive zones and is set to 0.5 mm. The mode I initiation strength is set equal to the matrix tensile strength Y_T of 87 MPa and the mode II initiation strength is set equal to the matrix 5% offset shear strength S_L of 90 MPa. Energy based linear softening in combination with the mixed-mode interaction (η = 2.9) according to the BK approach [57] is used. A penalty stiffness with a value of K = 200000 N/mm^3 is used for the welded interface. On the surfaces that are not welded, only contact and friction are taken into account.

5.5 EXPERIMENTAL RESULTS AND COMPARISON WITH FI-
NITE ELEMENT ANALYSIS

This section describes the experimental test results of the four different test configuration described in Figure 5.3.1 and section 5.4, comparing them to experimental results on UD specimens from the autoclave manufacturing process [21] and the finite element analysis. The testing campaign for the characterization tests consists of two phases. First, the feasibility of the specimen design is evaluated by comparing the two configurations (full weld versus weld center) and the best configuration is chosen. In the second testing phase, the influence of the manufacturing process conditions is investigated on the selected configuration. As a recall from section 5.3.2, the full weld specimen is a 25 mm wide specimen, but due to the welding process, the actual width of the welded interface is between 14 and 18 mm. The typical weld width of the first test phase was found to be 15 mm after measuring the fracture surface. The weld center specimens are only 12.7 mm wide, so there is no difference between the specimen and weld width.

5.5.1 WELDED DOUBLE CANTILEVER BEAM TESTS

EVALUATION OF THE TWO SPECIMEN CONFIGURATIONS

Initially three welds were performed, resulting in six DCB specimens after machining. The results of the tests is shown in Figure 5.5.1. Two full weld width specimens were performed (Figure 5.5.1a) and their load-displacement is compared to the FEM using a weld width of 15 mm and a mode I fracture toughness, G_{Ic}, of 2.1 kJ/m^2. This fracture toughness value is derived from one of the weld center tests and is used in the FEM of both configurations to compare their consistency as different vertical axis scale are used. One of the full weld tests shows a strong increase in fracture toughness after initiation, which is found to be related to excessive resin near the insert as shown on the fracture surface reported in Figure 5.5.2. Furthermore, both tests experience some unstable crack growth during propagation, which may be related to fiber bridging of the 0/0-interface or changes in weld quality.
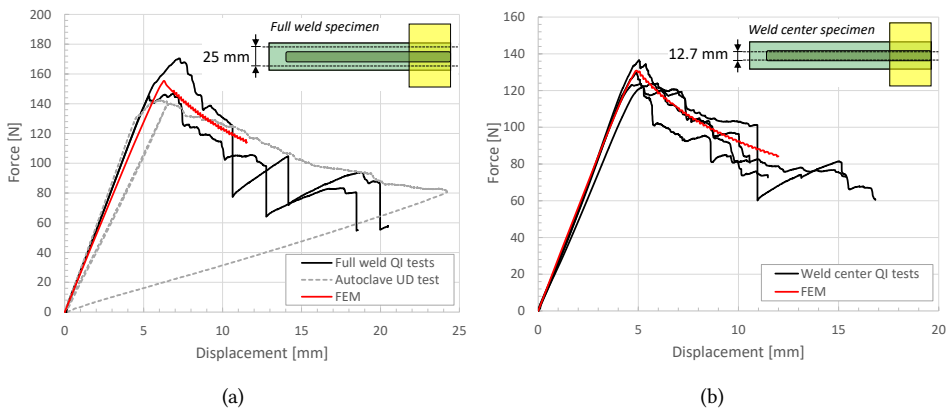

Figure 5.5.1: DCB test results for two configurations: a) full weld specimen; b) weld center specimen.

The experimental results of the full weld specimens are also compared to the autoclave consolidated test results reported in [21]. This comparison shows that the compliance calibration approach works well, as the initial compliance is nearly identical each even though a very different layup (UD vs QI) and initial crack length (a_0 = 48 mm vs 42 mm) is used. Interestingly, the load-displacement of full weld specimens reach the same load levels as the autoclave consolidated laminate, while the width of the weld is much lower (approx. 15 mm compared to 25 mm), and thus the welded fracture toughness is much higher compared to the 1.12 kJ/m^2 of the autoclave process. The fracture surface of the separated welded laminates also provide insight into the uniformity of the weld temperature along the 0.5 m. A variation in the order of 14 to 18 mm is observed, furthermore the higher temperature at the wider weld width could also be confirmed by the thermocouple data. Based on these observations it is concluded that the full weld specimen provides an excellent way to gain insight in the weld quality and to optimize the tooling, however for the determination of the weld material properties this would result in unwanted weld width effects and variation. The design of the weld center specimens prevents this.
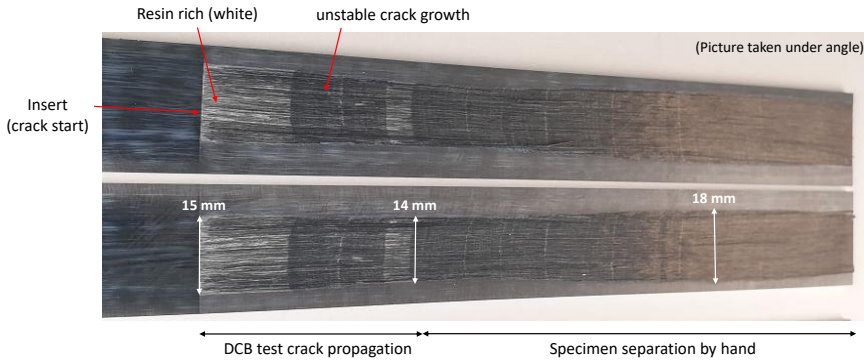
Figure 5.5.2: DCB fracture surface of full weld specimen with observed variation in weld width.

The experimental results of the first four tests of the weld center specimens is shown in Figure 5.5.1b. Again, comparison is made to the FEM using a mode I fracture toughness, G_{Ic}, of 2.1 kJ/m^2. The loads are lower compared to the full weld specimens because of the reduced width, but they are consistent in terms of fracture toughness. During testing of the weld center specimens it also became more clear that fiber bridging plays an important role. During one of the tests the crack fully arrested, which caused the load to increase, and finally caused the crack to propagate unstable. For the other tests, distinct variation in crack growth speed is observed when fiber bridging occurred and remains of broken fibers were found on the fracture surface.

INFLUENCE OF THE WELDING PROCESS PARAMETERS

The influence of the welding process parameters on the mode I fracture toughness is presented in Figure 5.5.3. Figure 5.5.3a shows the influence of the four different welding temperatures described in section 5.2. The parts of the load-displacement curves that indicate unstable crack growth, are removed to improve clarity for comparison. The FEM

results from Figure 5.5.1b are also presented in Figure 5.5.3. Furthermore, comparison is made to the FEM using the autoclave mode I fracture toughness, G_{Ic}, of 1.12 kJ/m². The results are found to be rather consistent between the different welding temperatures, exept for the very low temperature weld which created a kissing joint with almost no strength. Some of the lower temperature weld initiated early and represent the lower bound experimental results, while some of the high temperature welds show signs of fiber bridging and resin pockets that locally increase the fracture toughness towards the upper bound. The influence of cooldown is shown in Figure 5.5.3b. Again comparison

(a)   (b)
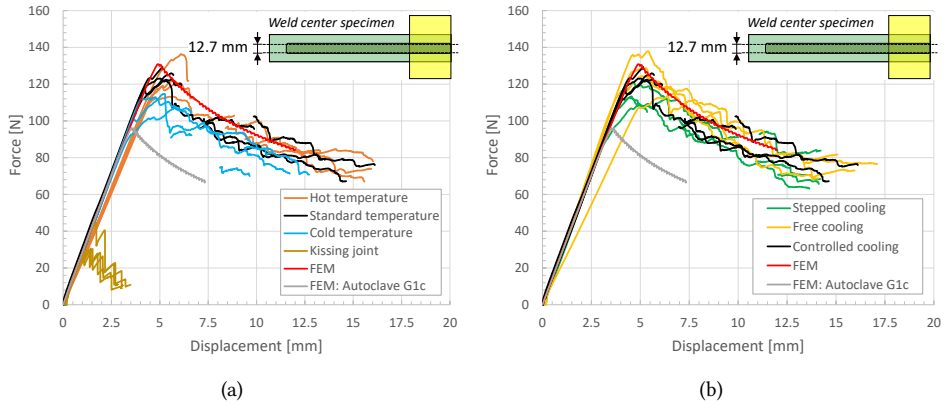
Figure 5.5.3: DCB test results, influence welding process: a) temperature; b) cooldown.

is made against FEM. The experimental results between stepped and controlled cooling were found to be similar, however all the free cooling curves tend towards the upper bound results. One of the possible explanations can be related to crystallization of the polymer matrix. Free cooldown allows for a rapid decrease in temperature, which may not allow the thermoplastic material to fully crystallize and this increases the ductility and fracture toughness of the material [108].

5.5.2 Welded end-notched flexure tests

Evaluation of the two specimen configurations

The ENF test results of the two different specimen configurations are shown in Figure 5.5.4. For the full weld specimens, two different test setups are used. Two tests are performed by using an initial crack length $a0 = 40$ mm and a span of $2L = 130$ mm. Another test is performed at an initial crack length $a0 = 33.5$ mm and a span of $2L = 115$ mm. Both configurations achieved stable crack growth. For each configuration a FEM study using a mode II fracture toughness, G_{IIc}, of 3.5 kJ/m² is performed to investigate the possible influence of the weld width (15 vs 18 mm as observed in Figure 5.5.2). The comparison of the test results for the two test setups of the full weld specimen configuration is shown in Figure 5.5.4a. It is found that the weld width may highly influence the results, therefore also for the ENF test, it is chosen to perform further testing on the weld center specimen configuration.
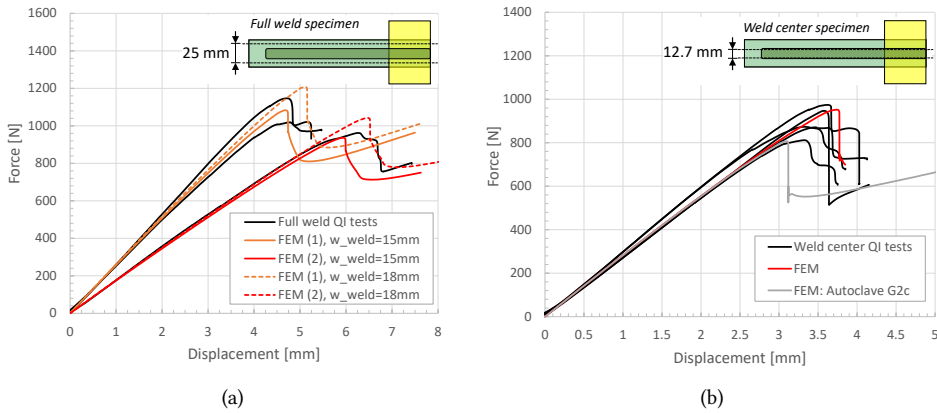
Figure 5.5.4: ENF test results for the two configurations: a) full weld specimen; b) weld center specimen.

Five tests were performed on the weld center specimen configuration using a test setup with an initial crack length $a0 = 25$ mm and a span of $2L = 90$ mm. The test results are presented in Figure 5.5.4b. Two of the tests showed unstable crack growth, which is likely caused by fiber bridging during the mode I as this made it difficult to create a pre-crack. The experimental results are compared to FEM using a mode II fracture toughness, G_{IIc}, of 3.5 kJ/m^2. FEM prediction were also made by using the G_{IIc} of 2.35 kJ/m^2 from the autoclave process. The main difference between the observed experimental response is the more gradual nonlinearity, which is related to the development of the fracture process zone, as also observed during the experiments on the autoclave consolidated material [21]. The fracture process zone is also observed visually as shown in Figure 5.5.5, which makes it difficult to identify the crack position. The FEM that uses linear softening seems to be unable to capture nonlinear effects on the load-displacement curve and it is expected that the full shape of the cohesive law may need to be used in the analysis to account for this [21].
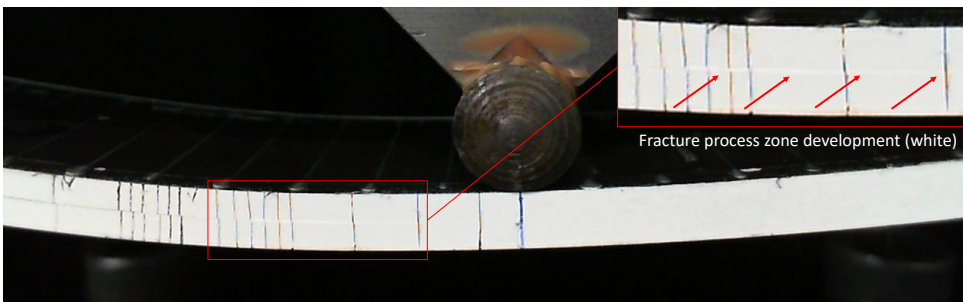
Figure 5.5.5: Visually observed fracture process zone during ENF test on full weld specimen.

INFLUENCE OF THE WELDING PROCESS PARAMETERS

The influence of the welding process parameters on the mode II fracture toughness is presented in Figure 5.5.6. The influence of the welding temperature on the ENF test by using the weld center specimens is shown in Figure 5.5.6a. One specimen is removed due to difficulties with the pre-crack. Again, the very low temperature weld created a kissing joint with almost no strength as shown by the lowest load-displacement curves is Figure 5.5.6a. The other mode II tests showed similar peak loads except for one of the cold temperature tests, which initiated near the fracture toughness according to the autoclave material [21] and can be observed by comparison to the FEM curve based on the autoclave G_{1c} in Figure 5.5.6. Although, some differences are observed between the tests. In some cases stable crack growth is achieved near the stability limit, which can be seen as an almost vertical drop in load, while in other cases crack growth appeared more gradual. Especially the hot temperature appeared more gradual, which suggests a stronger R-curve effect. The experimental results of different cooldown methods are shown in Figure
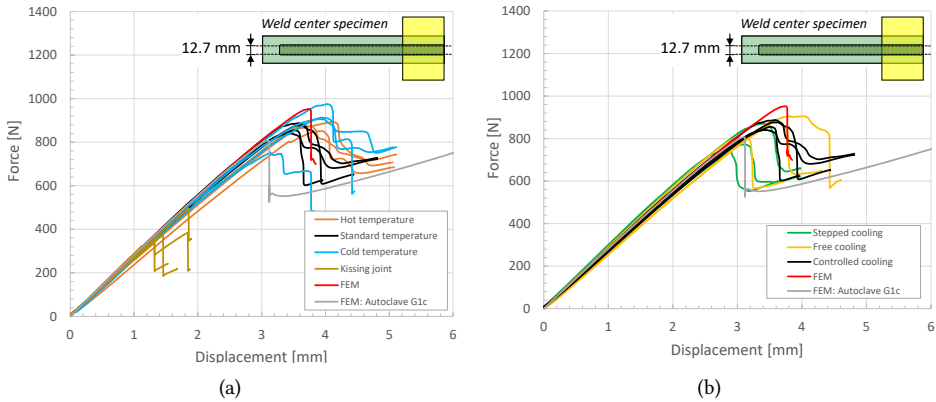
Figure 5.5.6: ENF test results, influence welding process: a) temperature; b) cooldown.

5.5.6b. Two specimens are removed due to difficulties with the pre-crack. Compared to the controlled cooling, both the stepped and free cooling showed a much larger variation in the load displacement curve. Interestingly, the lower bound experiment results approach the fracture toughness values from the autoclave consolidation process of G_{IIc} = 2.35 kJ/m^2, while the controlled cooldown results are near the G_{IIc} of 3.5 kJ/m^2 used in the FEM.

The exact location of the crack tip is difficult to determine visually as already shown in Figure 5.5.5, therefore the crack tip position is also evaluated using DIC. The color scaling in Figure 5.5.7 represents an equivalent strain value between 0-2.5% and the distance between the visually determined crack tip and the load introduction is 20 mm. The DIC results for 9 points along the load-displacement curve of a standard welding temperature sample are presented in Figure 5.5.7. The first point in the figure represents the start of the nonlinearity in the load-dispacement curve. During the development of this nonlineariy (point 1 to 4) it is difficult to determine the crack tip visually, but the DIC cleary shows high strains ahead of the crack tip. It is however still difficult to distinguish between a highly strained area or the actual crack and sliding of the top and bottom interfaces. The peak load is reached at

point 5, which is the start of stable crack propagation (point 5 to 8) and causes the load to drop. After the crack has propagated 20 mm, and it reaches the load-introduction point (point 9), which arrests the crack, resulting in an increase in load.

Figure 5.5.7: DIC measurement of ENF test: a) Load-displacement curve with nine measurement points; b) DIC results of measurements, equivalent strain 0-2.5%.

5.5.3 WELDED SINGLE LAP SHEAR TENSILE TESTS

Welded single lap shear tests are performed on a 250 kN Zwick tensile machine with hydraulic grips. The benefit of this machine is that gripping can be performed at an offset to prevent secondary bending. The results of the experiments, including the effect of the welding process temperature is shown in Figure 5.5.8. Initially, two tests (standard temperature) are performed using 50 bar of grip pressure. Some movements in the grips are observed which are also visible in the load-displacement curve as an increase in displacement in the linear part of the curve for one of the tests. However, the failure load is nearly identical. All other tests are performed by a gripping pressure of 100 bar and show consistent results. The cold temperature fail at approximately 14 kN, while the standard temperature samples fail slightly above 16 kN and hot specimens reach nearly 18 kN. The FEM that uses linear softening predicts a failure load of approximately 15 kN but is unable to predict the nonlinearity and shows some stiffening instead. The stiffening is likely due to the boundary conditions and is further evaluated in section 5.6.
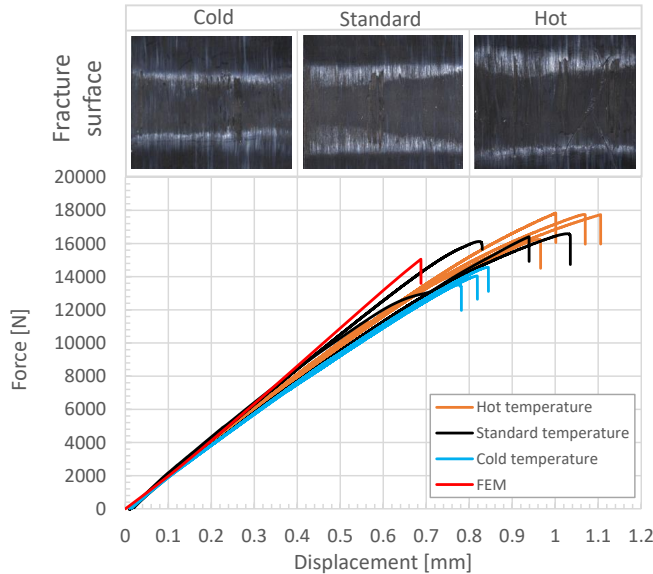
Figure 5.5.8: SLS tensile load-displacement curves: Weld size based on fracture surface for three weld temperatures.

Interestingly, when observing the fracture surface of the failed specimens, as shown in Figure 5.5.8, several effects become apparent: (1) The influence of weld temperature seems to highly influence the size/area of the weld, (2) The light colored area near the edge of the weld (top and bottom) contain large amounts of resin, (3) The edge of the weld shows signs of stable crack growth and/or development of a fracture process zone, and (4) through the thickness waviness/fiber nesting and signs of fiber failure is observed for the hot specimens. A close-up of the resin rich fracture process zone is shown in Figure 5.5.9a and fiber failure due to waviness/fiber nesting in Figure 5.5.9b. It is considered likely that the difference in weld area and influence of waviness/fiber nesting contributes to the main differences in strength observed in Figure 5.5.8. This will be further investigated by

analysis in section 5.6. The development of the fracture process zone in the SLS test can

(a)   (b)
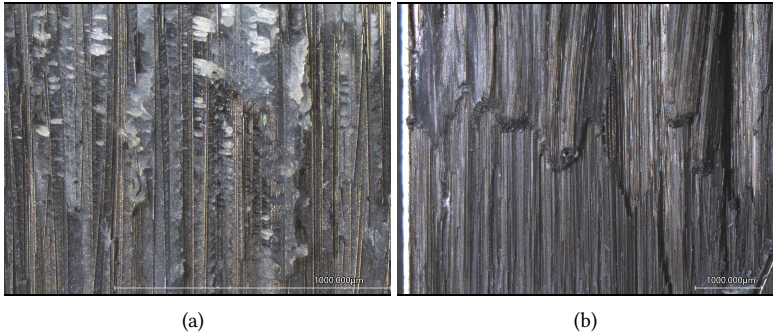
Figure 5.5.9: Close-up of fracture surface SLS of hot weld: a) Resin-rich area 10x; b) Fiber waviness/nesting and failure.

also be observed when use is made of DIC techniques [133]. The result of one of the hot specimens is shown in Figure 5.5.10. The edge of the SLS specimen is speckled with a fine spray and the equivalent strain is determined from the measured displacements. The color scale in Figure 5.5.10 is linear from 0 to 2.5% strain and pre-stresses from clamping are included in the DIC strain analysis. From the experimental load-displacement combined with the DIC results it becomes apparent that the nonlinearity in load-displacement is related to the development of the fracture process zone. At the start of the nonlinearity (1) the local strains in the welded interface gradually develop a fracture process zone (2). When this fracture process zone becomes large enough, and finally achieves high strains along the full weld, the peak load is reached (3) and the load drops, causing the specimen to fail.
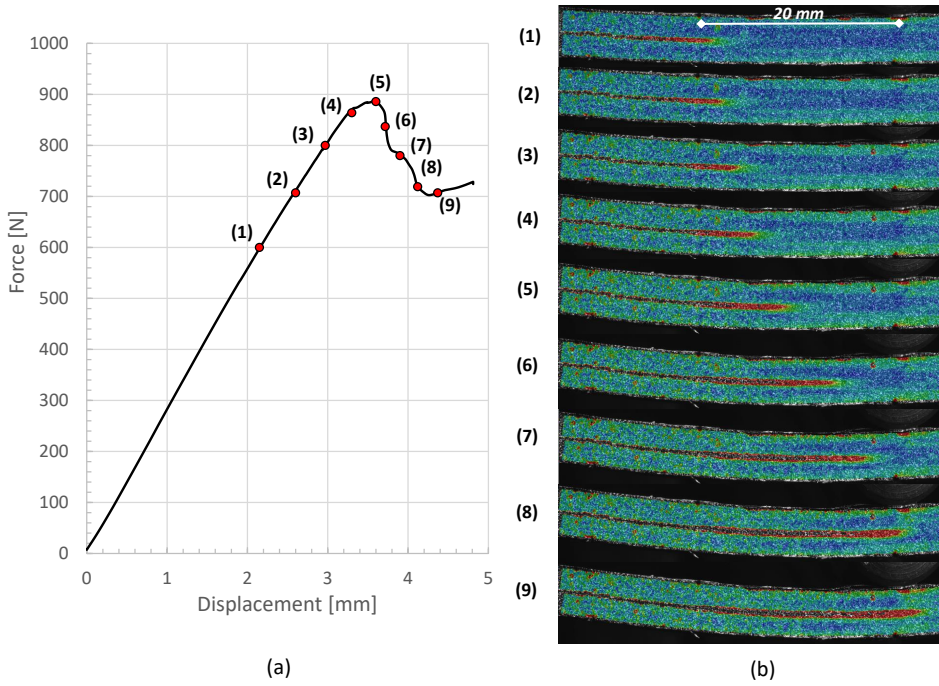

Figure 5.5.10: DIC measurement of SLS test: a) Load-displacement curve with three measurement points; b) DIC results of measurements, equivalent strain 0-2.5%.

5.5.4 Welded single lap shear 3-point bending tests

Welded single lap shear specimens are tested in 3-point bending for the three different welding temperatures. The experimental load-displacement curves are shown in Figure 5.5.11. Similar failure loads of approximately 1.2 kN are observed between the different specimens, except for one of the hot temperature samples that showed excessive fiber bridging and failed at approximately 1.4 kN. Figure 5.5.11 also presents the fracture surface of the different welding temperatures. This comparison shows a similar trend of the relation between welding temperature and weld size as the SLS tensile tests in Figure 5.5.8. The main difference is that in the SLS-3PB test, only one side of the fracture process zone shows a white marking. This is the side that opens in bending, which may suggest a more dominant mode I opening of the crack as the fracture surface of the DCB appears lighter compared to ENF. The different weld sizes also influence the bending stiffness of the SLS joint due to the larger joined surface. The FEM that uses linear softening predicts a failure load of approximately 1.1 kN but is unable to predict the nonlinearity.
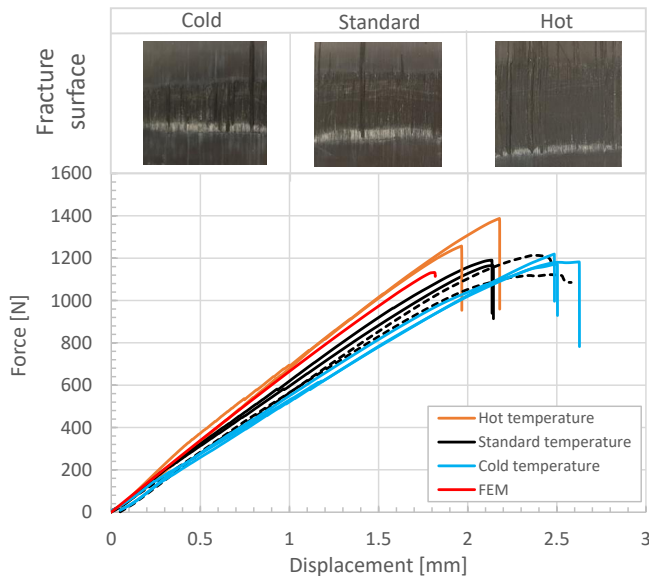
Figure 5.5.11: SLS-3PB load-displacement curves: Weld size based on fracture surface for three weld temperatures. Dashed line represents crack stop at load-introduction.

The failure process of the SLS-3PB test is investigated at five different points along the load-displacement curve by means of DIC. The results are shown in Figure 5.5.12. At the start of the nonlinearity (1) the crack opening is at the edge of the weld and gradually develops (2-4) until the remaining area becomes sufficiently small to cause unstable crack propagation and failure of the joint (5). It demonstrates that the nonlinearity in both the SLS tension and 3PB test is related to the development of the fracture process zone.
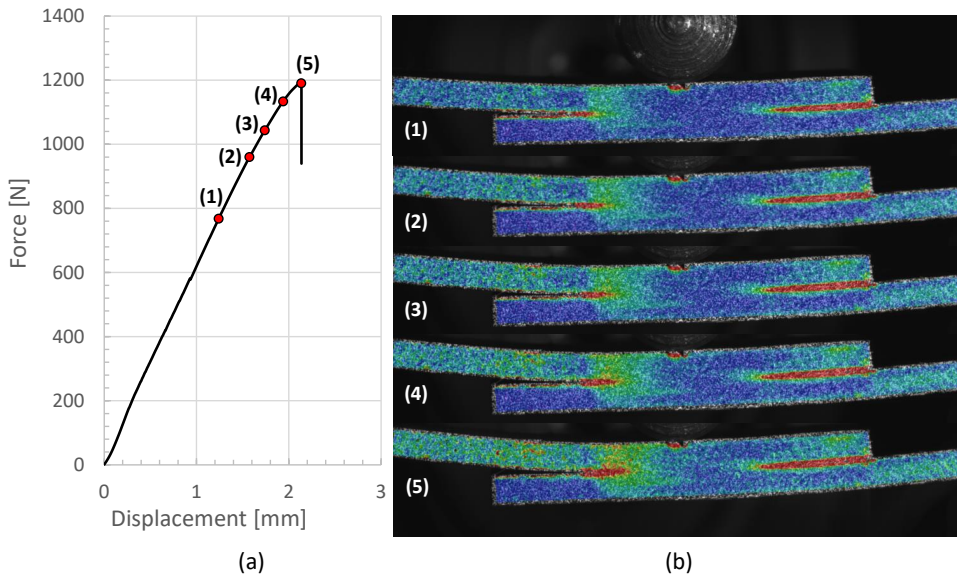
Figure 5.5.12: Load-displacement curve and failure process evaluation of SLS test by means of DIC, equivalent strain 0-2.5%.

Although failure loads were similar, the SLS-3PB test is found to be rather sensitive to the size and position of the weld. The weld size of 15 to 18 mm allows for only 7.5 to 9 mm of crack growth until the center roller is reached. If the weld is not perfectly centered, this may become even smaller or may force the crack to start from a specific direction. Compared to the ENF, which showed a much larger fracture process zone, the available short crack growth length means that the results are likely influenced by the load-introduction. This effect is observed in two of the standard temperature welds which are dashed in Figure 5.5.11. The crack grows up to the load-introduction of the 3PB test and laminate failure is observed without failure of the full joint. This is shown in the DIC image presented in Figure 5.5.13 where the red color indicates failure (2.5% equivalent strain) in both the weld and the laminate.
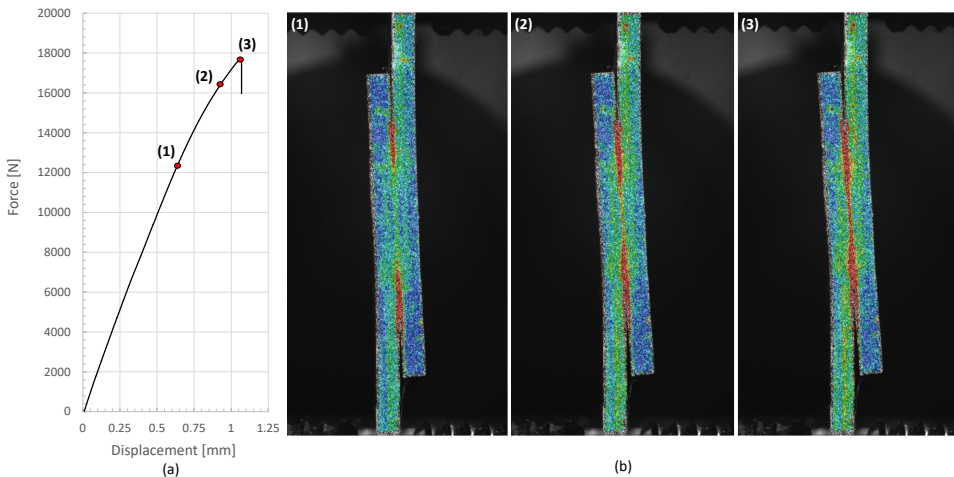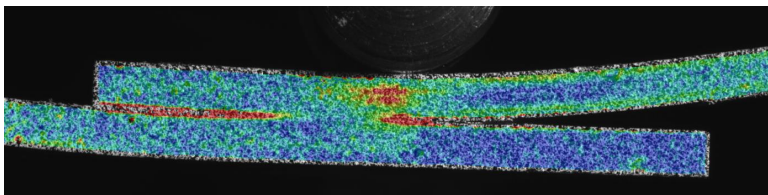

Figure 5.5.13: DIC measurement of SLS-3PB test: a) Load-displacement curve with five measurement points; b) DIC results of measurements, equivalent strain 0-2.5%.

5.5.5 FRACTOGRAPHIC INVESTIGATION

The fracture surface of the mode I and II tests is investigated by means of Scanning Electron Microscopy (SEM). This provides insight into the interlaminar damage mechanism so that a comparison can be made with autoclave consolidated fracture surfaces recently published by Tijs et al. [21] that were tested in the same loading modes. The main difference between the autoclave manufacturing process is the prolonged constant time and slow cooldown rate. Both the UD autoclave and welded QI specimens have a 0/0 degree interface angle, which is the fracture surface presented in this section.

SEM micrographs at different magnifications of fiber bridging during mode I are shown in Figure 5.5.14. Pull-out of large fiber bundles on the fracture surface were observed in the fracture surface of samples from the autoclave process as shown in Figure 5.5.14a [21]. The same phenomena is also observed for the welded specimens, as shown in Figure 5.5.14b. At 1000x magnification, as shown in the close-up of Figure 5.5.14c a significant difference is observed between the fracture surface of the autoclave and welded fracture surface. The fracture surface of the welding process shows more extensive polymer drawing out in the plane normal to the fiber direction and plastic deformation of the polymer. Furthermore, the fibers show even larger presence of polymer material on the fibers. This experimental evidence may explain the significant increase in fracture toughness measured during the welded DCB tests.

Figure 5.5.14: SEM micrographs of mode I fiber bridging fracture surface for different manufacturing processes: a) Autoclave, 300x; b) Welding, 250x; c) Close-up autoclave versus welding, 1000x.

The difference between the autoclave and welded fracture surface in mode I, and the presence of more plastic deformation, can also be observed in matrix rich locations. This

comparison for 1000x magnification is shown in Figure 5.5.15a and b, and with 3000x close-up in Figure 5.5.15c. Similar excessive polymer draw out is observed in the fiber beds. This plastic deformation of the polymer appears at fine offsets along the fiber direction for the welding process. The typical circular patterns that may suggest a relation with the crystallization kinetics of the thermoplastic polymer matrix [98] as shown in 5.5.15c [21] is not observed. This may suggest that crystallization during welding is different compared to autoclave consolidation, even though both processes allow for sufficient time for the fast-crystallizing PEKK polymer to crystallize [67].
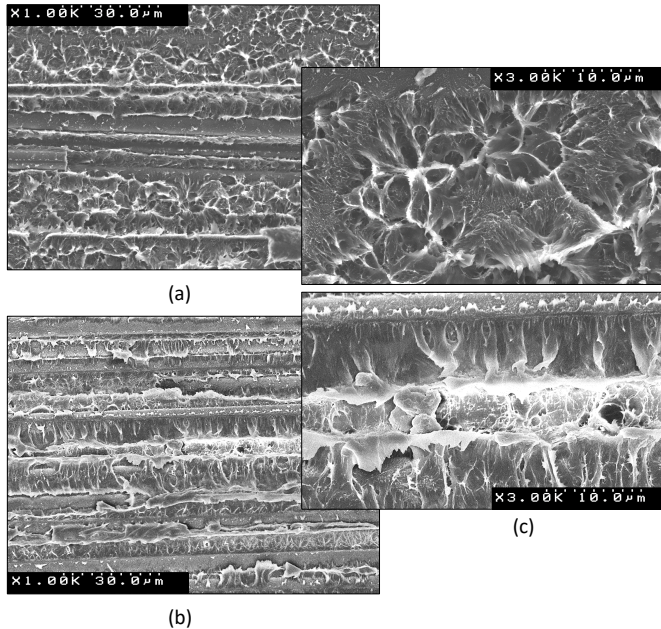
Figure 5.5.15: SEM micrographs of mode I fracture surface of matrix for different manufacturing processes: a) Autoclave, 1000x; b) Welding, 1000x; c) Close-up autoclave versus welding, 3000x.

SEM micrographs of the fracture surface of the mode II test are shown in Figure 5.5.16 and are again compared to micrographs from fracture surfaces of the autoclave process [21]. At 700x and 3000x magnification the failure mechanisms appear very similar, which feature extensive plastic deformation in the plane of the delamination, with some signs of broken fibers. This comparison is shown in 5.5.16a and b. Furthermore, some regions show resin rich areas with plastic deformation as shown in the close-up of Figure 5.5.16c, while other areas lack the presence of large amount of resin.

5

(a)

(b)

(c)
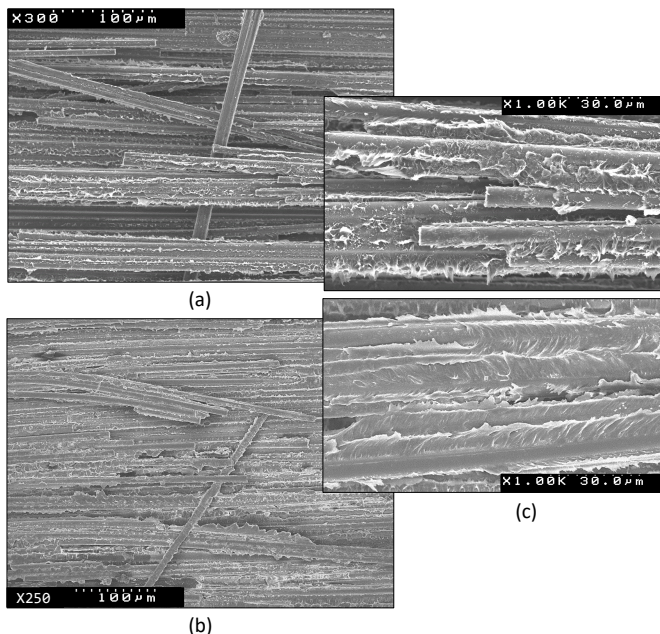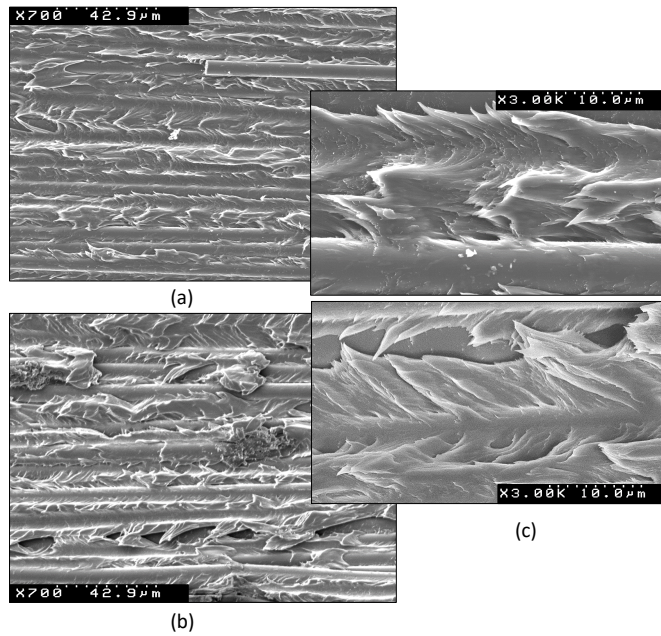
Figure 5.5.16: SEM micrographs of mode II fracture surface for different manufacturing processes: a) Autoclave, 700x; b) Welding, 700x; c) Close-up autoclave versus welding, 3000x.

5.6 ANALYSIS AND DISCUSSION

Some of the effects observed in the experimental results, such as the nonlinearity in the load-displacement curves, the development of the fracture process zones and the influence of the weld size on the failure loads are discussed in this section. First the mode I (DCB) and mode II (ENF) characterization data is evaluated and this is then used to study the SLS joint during tensile and 3PB loading in the numerical analysis. For each test, comparison is made to the 'default FEM' results presented in section 5.5.

5.6.1 WELDED DOUBLE CANTILEVER BEAM ANALYSIS

The load-displacement curve of one of the standard temperature welded DCB specimens is shown in Figure 5.6.1a and the data reduction methodology described in section 5.4.1 is used to determine the mode I fracture toughness. The mode I fracture toughness for each crack length is shown in the R-curve in Figure 5.6.1b. The R-curve shows a small increase in fracture energy at the start and reaches a plateau of approximately 1.95 kJ/m^2 shortly after, as identified with the dotted line in Figure 5.6.1b. Compared to Figure 5.5.1 and 5.5.3, this is towards the lower bound experimental results. However, for the numerical analysis it is chosen to be consistent, so all results are evaluated using the standard welding temperature results. Therefore, a G_{Ic} = 1.95 kJ/m^2 is selected for the following analyses and the mode I strength is set to 87 MPa. Due to the variation observed in the experimental results in Figure 5.5.3 the shape of the cohesive law is assumed to have a general exponential form and reaches fully damaged state at 0.15 mm opening displacement. Verification of the cohesive law is shown in Figure 5.6.1a by comparing the experimental load-displacement curve to the FEM.

(a)

(b)
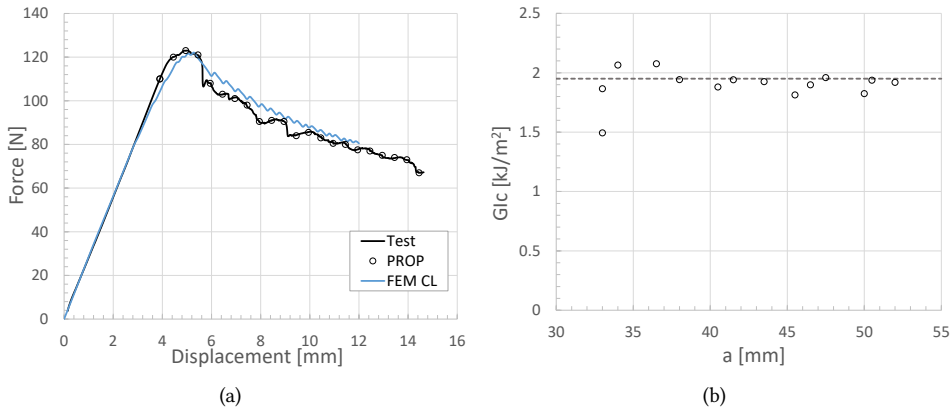
Figure 5.6.1: Analysis of standard temperature weld DCB test: a) Load-displacement curves with crack growth propagation (PROP) points and comparison with FEM; b) R-curve with selected mode I fracture toughness.

5.6.2 WELDED END-NOTCHED FLEXURE ANALYSIS

In the comparison of the FEM analysis with the experimental ENF test results presented in Figure 5.5.4 and 5.5.6 it is found that the default FEM analysis has difficulties in predicting the nonlinearity in the load-displacement curve. The FEM also predicts unstable crack propagation while the experiments show stable crack propagation. The analysis results are compared to a load-displacement curve of one ENF test in Figure 5.6.2a. By making use of the numerical methodology described by Tijs et al. [21], which allows for taking into account the shape of the Cohesive Law (CL), it can be demonstrated that a different shape of the CL is likely responsible for the different behavior. Figure 5.6.2b shows a comparison between the default linear softening and four different shapes of cohesive laws. During this comparison it is found that the mode II fracture toughness, G_{IIc}, had to be increased from 3.5 kJ/m^2 to 3.7 kJ/m^2. The difference between the four cohesive laws in Figure 5.6.2b is as follows: CL-1 and CL-2 are nearly identical except for the initiation strength. Since the mesh size is sufficiently small [99], this has no significant influence on the load-displacement curve. CL-3 and CL-4 dissipate more energy at the start of the cohesive law and cause the failure load to increase and reduce the nonlinearity. Therefore it is found that the tail of the cohesive law is responsible for most of the nonlinear behavior.

(a)   (b)
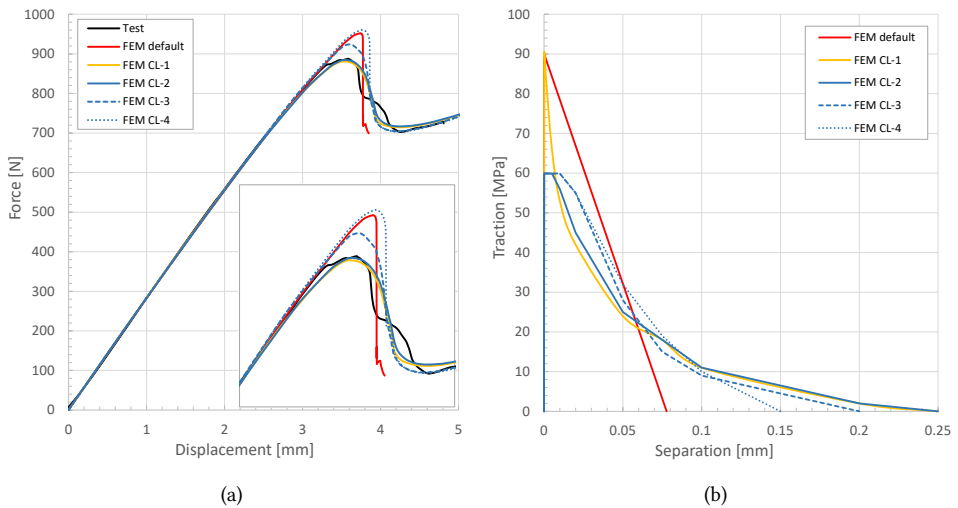
Figure 5.6.2: Influence cohesive law on the load-displacement curve of the ENF test: a) FEM load-displacement curves; b) Cohesive laws.

5.6.3 WELDED SINGLE LAP SHEAR TENSILE ANALYSIS

The numerical evaluation of the welded SLS tensile test considers two analyses: (1) The influence of the weld width on the failure loading, using the default FEM; (2) The influence of the cohesive law on the nonlinearity of the load-displacement curve. The difference between the FEM result presented in Figure 5.5.8 is the gripping length, which gives a stiffening effect in the load-displacement curve when applied at the full length of the specimen. On the imprints of the hydraulic grips it is found that the grips provide clamping over the first 30 mm of the specimen and that the grip center is near the end of the specimen. In the FEM model this is simplified to be fully constrained at 30 mm. The influence of the weld width on the failure load is studied between 10 mm and 20 mm and the results are presented in Figure 5.6.3a. It is found that the predictions are approximately 1 kN lower compared to the results presented in Figure 5.5.8, but the influence of the weld width is well predicted.
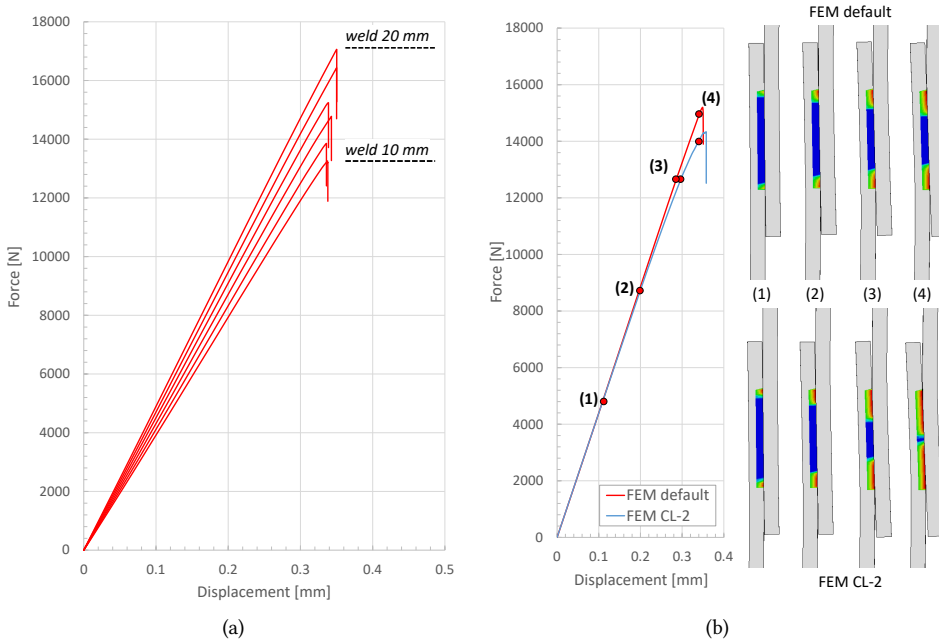
Figure 5.6.3: Numerical analysis of the SLS tensile test: a) Influence of weld width on failure load; b) Influence of cohesive law on load-displacement nonlinearity (cohesive damage field output).

The influence of the cohesive law on the nonlinearity of the load-displacement curve is shown in Figure 5.6.3b and is compared at four different points along the load-displacement curve. The size of the fracture process zone is identified with the cohesive damage field output variable, where red represents a fully damaged interface. The use of the cohesive law promotes the development of the fracture process zone and initiates the nonlinearity early at approximately half-way (2) of the load-displacement curve. Compared to the default FEM, the fracture process zone becomes significantly larger (3-4) resulting in a nonlinearity in the load-displacement curve and a reduced failure load. It is observed that this does

not significantly increase the total displacement as found in the experimental results. It
can not be predicted by the current simplified approach, which collapses all dissipating
fracture mechanisms into the cohesive surface and does not account for the nonlinearity
due to plasticity in both the interface and its surrounding. The fact that plasticity plays an
important role is already confirmed in the SEM micrographs.

5.6.4 WELDED SINGLE LAP SHEAR 3-POINT BENDING ANALYSIS

The results of the numerical analysis of the SLS-3PB test is presented in Figure 5.6.4. Similar
as for tensile loading, both the influence of weld width and cohesive law are investigated.
The influence of the weld width on the failure load is shown in Figure 5.6.4a. Six analyses are
performed covering 10 to 20 mm of weld width. It is shown that the weld width influences
both the failure load and the bending stiffness of the specimen. Also, the shorter weld
width allows for little crack propagation before reaching the load-introduction point, which
arrests the crack in the numerical analysis. This effect is also observed in some of the
experimental results presented in Figure 5.5.11. Furthermore, the numerical analysis shows
that crack propagation is close to the stability limit, which may explain why some joints
fail and others arrest in the experimental results.
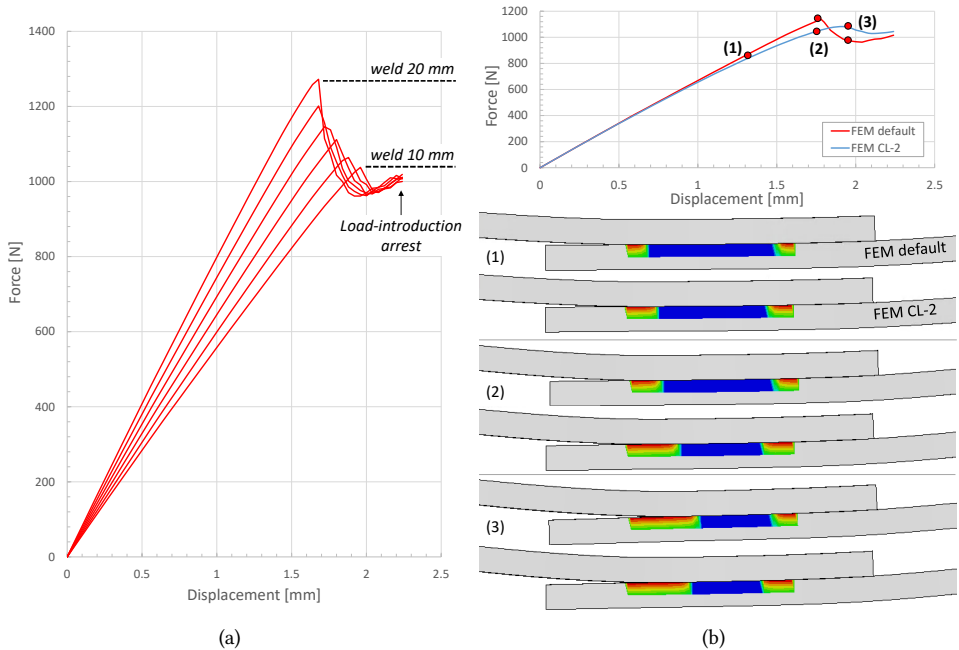
Figure 5.6.4: Numerical analysis of the SLS-3PB test: a) Influence of weld width on failure load; b) Influence of
cohesive law on load-displacement nonlinearity (cohesive damage field output).

The influence of the cohesive law on the nonlinearity of the load-displacement curve
at three points is shown in Figure 5.6.4b. The size of the fracture process zone is identified
with the cohesive damage field output variable, where red represents a fully damaged

interface. It is shown that the cohesive law has a pronounced influence on the nonlinearity of the load-displacement curve. This results in a more gradual drop in the maximum load before reaching arrest due to the load-introduction point. Considering these effects it is expected that the SLS-3PB test is rather sensitive to the weld size, to the position of the weld within the overlap and asymmetry due to the positioning of the specimen. It is also expected that the load-introduction influences the failure process as for the ENF test. Similarly, as observed during the SLS tensile test analysis, the size of the fracture process zone in the numerical analysis appears to be larger compared to the experimental results. This may suggest that more fidelity is required, for example modelling multiple layers or including a finite thickness interface. Furthermore, including effects such as plasticity as one of the dissipating failure mechanisms may be required.

5.7 Conclusions

Thermoplastic composite conduction welded joints are successfully characterized, tested and analyzed, while accounting for the influence of the manufacturing process. Welding recipes are designed to weld AS4D/PEKK-FC thermoplastic composites specimens using four different temperatures and three different cooldown methods on a half a meter long welding tool. The weldability of the specimens is ensured by making use of a quasi-isotropic layup. The laminates are welded with a 0-degree interface angle so that there are no secondary failure modes and crack propagation is only at the welded interface. Double Cantilever Beam and End-Notched Flexure specimens are successfully designed from the welded laminates to characterize the fracture toughness of the joint in both mode I and II loading condition. A compliance calibration strategy is used to test and easily compare the different configurations. During testing it was found that specimens cut from the center of the weld provided the most reliable results, as there is no influence of variation in weld width. Besides, the measured fracture toughness of the welded joint is significantly higher compared to autoclave consolidated thermoplastic material. A small effect on the fracture toughness is observed due to welding process conditions if the typical process window is respected. Similar to autoclave consolidated specimens, effects of fiber bridging on the fracture toughness are identified. Micrographs of the fracture surface revealed that the increase in fracture toughness may be explained by the difference in failure mechanisms and more excessive plastic deformation of the thermoplastic polymer matrix.

The welded joints were also tested in tension and in three-point-bending by making use of single lap-shear specimens. The influence of the manufacturing process showed a more pronounced effect on the strength of the welded joint during these tests. The experiments showed that the weld temperature highly influences the weld size, which can be directly related to a change in strength. For hot welding temperature, the influence of fiber bridging and nesting further increased the strength. Furthermore, DIC measurements during the SLS test revealed the gradual development of a fracture process zone, similar to the mode II characterization test, that can be related to the nonlinearity in the load-displacement curve in both the tensile and bending SLS test. It also appeared that testing in three-point-bending introduces difficulties related to the small weld width compared to the available crack growth length. This led to crack arrest in some samples, with laminate failure as a result.

The analysis showed that the numerical methods predicted unstable crack propagation in mode II, while the experiments showed nonlinear behavior and a more gradual fracture

process. It was found that the shape of the cohesive law is responsible for this effect in the numerical analysis. The measured fracture toughness is used in the numerical analysis to also predict the strength of the SLS joints in tensile and three-point-bending loading. Use of the FEM with linear softening showed that the effects of weld size on the joint strength can be predicted, but in a conservative manner. By accounting for the shape of the mode II cohesive law the nonlinearity of the load-displacement curve can be predicted, and the limitation of the cohesive zone approach, which collapses all dissipating fracture mechanisms to a single interface, may be responsible for the difference between the numerical and experimental fracture process zone, size as plasticity in the surrounding material is not accounted for.

Summarizing, new insights in the relation between the manufacturing process, the quality of the weld and the mechanical properties of the welded joints are provided, together with useful tools to support the design and analysis of thermoplastic conduction welded joints.

5

6

Conclusions and recommendations

6.1 Conclusions

The research presented in this thesis describes the analysis of matrix dominated failure of thermoplastic composites and conduction welded joints. Both experimental and numerical methodologies are developed to support the design of thermoplastic composites structures. The research addresses important linkages between the three main pillars of *Manufacturing*, *Experimental* and *Numerical* analysis and special attention is paid to the influence of the manufacturing process on the mechanical behavior by evaluating both the autoclave and conduction welding manufacturing process. The conclusions derived from the individual chapters can be summarized as follows:

- The importance of accounting for large deformation in predicting matrix failure, in particular ply splitting, by means of continuum damage models is demonstrated by studying two distinct approaches at the single element, ply and coupon level. The first approach is based on small-strain increments and the Cauchy stress. This approach runs into difficulties during large shear deformation as spurious stresses trigger incorrect failure modes. The incorrectly defined matrix crack orientation due to material axis rotation may cause load transfer across matrix cracks, where the strain and/or rotations due to softening and material nonlinearity may become large enough to invalidate the assumptions inherent to small strain theory. Analysis of the open-hole laminate also confirm that the first approach is unable to predict the correct failure mechanisms at the meso-scale. The present analysis also highlights that the inaccuracy in the analysis can be corrected by expressing the constitutive equations based on a Lagrangian kinematic measure. This is done through the use of the Green-Lagrange strain and the 2nd Piola-Kirchhoff stress and allows for prediction of fully developed ply splits. These ply splits show a strong interaction with delaminations and significantly improve the prediction of the failure mechanisms at the meso-scale for the open-hole coupon test. These improvements in the numerical methodology are successfully used in the thesis to predict the matrix-dominated failure modes of thermoplastic composites welded joints. This is found to be important,

as the increased toughness and nonlinear behavior of the thermoplastic polymer will promote larger deformations in the local failure mechanisms.

- The interlaminar behavior of autoclave consolidated AS4D/PEKK-FC thermoplastic composites is characterized and analyzed during quasi-static loading. During the analysis, special attention is paid to the influence of fiber bridging and R-curve effects. Both experimental and numerical analyses are performed on Double Cantilever Beam (Mode I), End-Notched Flexure (Mode II), Calibrated End Loaded Split (Mode II), and Mixed-Mode Bending (Mixed Mode I/II at 50:50) test configurations. Mode II in three-point-bending with the End-Notched Flexure test method appeared to be difficult due to the presence of a large fracture process zone and several recommendation were given to account for this issue. Fractographic analysis provided new insights into the interlaminar damage mechanisms present in the fracture surface and confirmed the presence of large scale fiber bridging and significant plastic deformation in the thermoplastic polymer matrix. The micrographs confirmed the absence of fiber bridging in Mixed Mode I/II at 50:50 and Mode II loading conditions. Furthermore, indications suggest that polymer crystallization may play an important role in the matrix-dominated behavior. The load-displacement curves of the experiments are evaluated using a recently developed data reduction methodology. This method is convenient for materials that experience large fracture process zones, as it does not require measuring the position of the crack tip, and the methods provide cohesive laws for the numerical analysis method as output. It is found that the cohesive laws of the Mode II tests were nearly identical, which confirms that the cohesive law is independent of the test configuration and reproducible results are obtained at two different labs. The new procedure that is developed to process the experimental cohesive laws allows for direct implementation in commercial finite element software, without user-defined subroutines. New insights into the role of fiber bridging on the mixed-mode interlaminar behavior are found and a rather low initiation fracture toughness is observed. Most of the scatter in fracture properties is observed during propagation, and likely attributed to fiber bridging. Fiber bridging is also found only to increase the fracture toughness when sufficient crack opening displacement is achieved, thus something to consider for small cracks that may not benefit from this increase in toughness. The tabular cohesive laws are implemented for the numerical analysis into a single material card and it is found that special considerations were required for the mixed-mode behavior due to fiber bridging. After considering the fiber-bridging and R-curve effects, good correlation for all the different experimental test configurations was achieved.

- The mixed-mode interlaminar properties and the new continuum damage model are use to analyse the strength and failure behavior of welded single lap-shear joints both numerically and experimentally. Test coupons are designed for welding by means of a robot and tested by Fokker/GKN aerospace. The experiments demonstrate that the complex failure behavior of the welded joints show a pronounced interaction with the failure modes of the surrounding plies. For the numerical analysis of the welded joint both a simplified and a high-fidelity approach is proposed. The simplified approach, which is based on the cohesive zone method, predicts conservative joint strength when unidirectional autoclave consolidated interlaminar fracture toughness

properties are used. Scaling the properties required an apparent fracture toughness that is approximately 2.5 times higher compared to measured from the autoclave material. The new high-fidelity modelling approach is used to investigate the influence of the complex failure behavior of the welded joint. It is demonstrated that the new continuum damage model is able to accurately predict the matrix failure and ply splitting failure modes of the welded joint. However, it was also found that predicting the upper bound experimental results is still difficult and some limitations to the numerical methodology such as, mode-mixity during crack propagation, non-zero matrix crack angles near the welded interface and not considering frictional effects on the fracture plane were identified. The analysis methodology is then used to explore the influence of possibly different inter- and intralaminar material properties. This appeared to have a strong effect on the joint strength and may significantly influence the failure modes. This study predicted that the most likely source of the mismatch in prediction may be related to changes in local material properties due to the welding manufacturing process.

- A methodology to characterize, test and analyse thermoplastic composite conduction welded joints is developed and validated. Welding recipes are designed to join AS4D/PEKK-FC thermoplastic composites specimens using various different manufacturing process parameters. The weldability of the laminates is ensured through the use of a quasi-isotropic layup, which is welded at a 0-degree interface angle. This was done based on experience of the single lap-shear joints to prevent secondary failure modes and to force the crack to propagate only at the welded interface. Characterization tests are performed by means of double cantilever beam and end-notched flexure tests on two different specimen configurations. The first configuration, identified as full weld specimen provided most insight in the manufacturing quality of the weld, however, the specimens cut from the center of the weld were found to be the most representative to characterize the material properties of the joint as there is no influence of variation in weld width. The measured fracture toughness values of the welded joints are found to be significantly higher compared to autoclave consolidated thermoplastic material. Furthermore, only little influence on the fracture toughness is measured if temperatures are within the typical manufacturing process window. The influence of fiber bridging on the fracture toughness is also observed during testing and on the fractures. The fractographic analysis also revealed that the increase in fracture toughness compared to the autoclave material may be explained by the difference in failure mechanisms. Also, more excessive plastic deformation of the thermoplastic polymer matrix was found. Experiments of the welded single lap-shear joints during tensile and three-point-bending showed that the influence of the manufacturing process had a more pronounced effect on the strength as the welding temperature highly influences the width of the welded interface. Furthermore, welding at hot temperatures further increased the strength due to excessive fiber bridging and nesting of the fibers. Digital image correlation on the single lap-shear joints identified that the nonlinearity in the load-displacement curve can be correlated to the development of a fracture process zone for both the tensile and three-point-bending test. Although, the three-point-bending test is not found to be reliable due to the small weld width compared to the available crack growth

length available. The analysis of the characterization tests showed that the default linear softening law is unable to predict the nonlinearity in the load-displacement curves observed experimentally. The linear softening laws also introduced unstable crack propagation, while the experiments showed a more gradual failure process. Introducing the correct shape of the cohesive law could improve the prediction of the nonlinearity, but the numerical analysis was unable to increase to total displacement compared to what is observed experimentally. The numerical fracture process zone size also appeared to be larger compared to the experiments. It is discussed that the limitation of the cohesive zone approach, which collapses all dissipating fracture mechanisms to a single interface, may be responsible for the difference between the numerical and experimental fracture process zone size as plasticity in the surrounding material is not accounted for.

In this research, the matrix dominated failure of thermoplastic composites and conduction welded joints has been studied in great detail and several experimental and numerical methodologies are developed to support the design of thermoplastic composites structures. The general conclusions in relation to the three main pillars are that for *Manufacturing* the developed welded joint specimens can be used to determine both to the manufacturing quality and material properties of the weld. The methodology can also be used to explore the boundaries of the manufacturing process window in relation to quality and performance of the welded joints. Furthermore, it is demonstrated that the material properties of the thermoplastic composite are highly influenced by the manufacturing process. The mechanical behavior of the welded joints is significantly different compared to material from the autoclave manufacturing process and needs to be considered in the design process. Furthermore, it is expected that the geometry, layup and thermal mass of the welded structure will influence the weld width and thus influences the joint strength. The developed *Experimental* methodologies provide insight into the failure mechanisms that determine the fracture toughness and joint strength of the thermoplastic composite and welded joints. The data reduction methodology based on only the load-displacement curve and compliance calibration approach allows for evaluation of the experimental data without the need to monitor the crack tip and can thus also be used in situations where placing a camera system is difficult, for example while testing environmental conditions in a climate chamber. The approach to represent the cohesive law in tabular format is developed and validated on interlaminar behavior, but the method is general applicable and may also be used to describe translaminar failure. Furthermore, the method is not limited to only interface elements or cohesive surfaces and it is demonstrated that the cohesive zone method can be used for the *Numerical* analysis of the welded joints. The use of the cohesive law in the numerical analysis allows for a detailed description of the failure behavior and can take into account both the initiation and propagation values. This means that the analysis methodology will provide an accurate prediction for both small at the coupon level but also for large cracks at the structural level. For the continuum damage model it is demonstrated that the improvements in general of high importance when large deformations are present in within the local failure mechanisms. It is also demonstrated that the methodology improves the high-fidelity analysis of both thermoset and thermoplastic composites.

6.2 Recommendations

The present work provides new insights into the matrix dominated failure of thermoplastic composites and conduction welded joints. From the research several recommendations can be made, which may also be used to define future research directions. The recommendations are summarized below for each of the three main pillars.

Manufacturing: The influence of the manufacturing process cycle on the mechanical behavior and failure mechanisms of thermoplastic composites is demonstrated, however, this could be further explored with the developed methodologies. It is recommended to studies a wider variation of temperatures, constant times and cooldown rates. The influence of high, above theoretical polymer degradation, temperature on the NDI quality and stamp surface may need to be investigated including the effect of thermal history and polymer degradation. Welding with excessively low temperatures resulted in a 'kissing weld' in the NDI results. It is recommended to always measure stamp and anvil laminate surface temperature to ensure a minimum temperature, quality and size of the welded interface. Ideally the reaction and uniformity of force/pressure on the stamp should also be measured. Also, welding is currently performed based on a recipe defined by generator power and time. This makes the process depending on the welding conditions such as environment, boundary conditions and thermal mass of the parts. It is recommended to develop a feedback loop based on measured temperatures on the part to control the process. The edge distance of the weld needs to be determined based on the thermal mass and required welding temperature of the configuration in order to prevent melting of the laminate edge and edge-delaminations. Finally, it is also recommended to further study the influence of the manufacturing process cycle on AS4D/PEKK-FC thermoplastic composites at the polymer level, however, the fibers may influence crystallization kinetics.

Experimental: The influence of fiber-bridging plays an important role in the measured fracture toughness. It is assumed that by using a small interface angle (for example 5°) instead of the typical 0-0 degree interface angle, this effect could be removed and may lower the fracture toughness values towards the initiation fracture toughness. Also, the initial conditions of the insert or length of the pre-crack may have a strong influence on the measured R-curve. This may be important for a large variety of materials with a large fracture process zone. The welded joint material properties are increased compared to the autoclave consolidated material, but the crack propagation appeared more unstable. This in combination with fiber bridging and secondary failure modes may increase the scatter and reduce the B-value design allowables. It is recommended to further investigate the sources of scatter. The experimental methodologies that are developed are general applicable and be used in climate chambers. Therefore, the performance and material behavior of the welded joints during environmental conditions can be used to determine the most critical material properties for the design of thermoplastic composite interfaces and welded joints.

Analysis: The design guidelines of thermoplastic composite structures may need to not only consider the welded interface but also the surrounding plies. Furthermore, the influence of the interface ply-angle may have a strong influence on the joint strength and requires further investigation. Virtual Testing may be used to explore the boundaries of the design space and could help to de-risk unexpected failure modes. Matrix damage due to large out-of-plane shear, interaction with cohesive surfaces and their corresponding failure criteria

6

needs to further explored in the modelling methodology. In particular, the influence of matrix damage, crack angle and local softening on delamination growth. In the continuum damage model, the crack angle after mode-mixity change or re-loading needs to be further explored and may require a energy-based mixed-mode definition. Finally, the cohesive zone analysis is able to predict a large process zone and corresponding nonlinearity in the load-displacement curve. However, the size of the process zone appears to be larger as observed experimentally. The influence of plasticity in the surrounding of the cohesive zone may need to be explored to explain this effect.

6

Bibliography

References

[1] A. Benatar and T. G. Gutowski. Method for fusion bonding thermoplastic composites. *SAMPE*, 18(1), 1986.

[2] M. M. Schwartz. *Joining of composite-matrix materials*. ASM International, 1994.

[3] A. P. da Costa, E. C. Botelho, M. L. Costa, N. E. Narita, and J. R. Tarpani. A Review of Welding Technologies for Thermoplastic Composites in Aerospace Applications. *Journal of Aerospace Technology and Management*, 4(3):255–265, 2012.

[4] H. Shi, I. F. Villegas, and H. E. N. Bersee. Strength and failure modes in resistance welded thermoplastic composite joints: Effect of fibre-matrix adhesion and fibre orientation. *Composites Part A: Applied Science and Manufacturing*, 55:1–10, 12 2013.

[5] G. Erb and G. Bernhart. Investigation of continuous induction welding of C/PAEK laminates. In *Proceedings of the 18th European Conference on Composite Materials*, Athens, Greece, 2018.

[6] T. J. Ahmed, D. Stavrov, H. E.N. Bersee, and A. Beukers. Induction welding of thermoplastic composites—an overview. *Composites Part A: Applied Science and Manufacturing*, 37(10):1638–1651, 10 2006.

[7] I. F. Villegas. Ultrasonic Welding of Thermoplastic Composites. *Frontiers in Materials*, 6:291, 11 2019.

[8] J. W. van Ingen. Thermoplastic orthogrid fuselage shell. *SAMPE*, 52(5):7–15, 2016.

[9] J. W. van Ingen, J. E. A. Waleson, A. Offringa, and M. Chapman. Double curved thermoplastic orthogrid rear fuselage shell. In *SAMPE Europe Conference*, pages 1–10, Nantes, France, 2019.

[10] M. H. J. Doldersum, J. Teunissen, A. Offringa, and J. W. Van Ingen. Conduction Welding. US Patent 20200276769 16/646219, 9 2020.

[11] B. H. A. H. Tijs, A. Turon, and C. Bisagni. Characterization and analysis of conduction welded thermoplastic composite joints considering the influence of manufacturing. *Manuscript prepared for submission to Elsevier*, 2023.

[12] B. H. A. H. Tijs, M. H. J. Doldersum, A. Turon, J. E. A. Waleson, and C. Bisagni. Experimental and numerical evaluation of conduction welded thermoplastic composite joints. *Composite Structures*, 281:114964, 2 2022.

[13] Morten G. Ostergaard, Andrew R. Ibbotson, Olivier Le Roux, and Alan M. Prior. Virtual testing of aircraft structures. *CEAS Aeronautical Journal*, 1(1-4):83–103, 9 2011.

[14] B. H. A. H. Tijs, C. S. Lopes, A. Turon, C. Bisagni, J. Waleson, J. W. Van Ingen, and S. L. Veldman. Virtual testing of thermoplastic composites: Towards a hybrid simulation-physical testing pyramid. In *Proceedings of the 18th European Conference on Composite Materials*, Athens, Greece, 6 2018.

[15] B. H. A. H. Tijs, K. S. van Dooren, and C. Bisagni. Development of a numerical framework for virtual testing to support design of a next generation thermoplastic multifunctional fuselage. In *European Conference On Multifunctional Structures (EMuS2020)*, pages 90–95, 2020.

[16] O. Falcó, R. L. Ávila, B. Tijs, and C. S. Lopes. Modelling and simulation methodology for unidirectional composite laminates in a Virtual Test Lab framework. *Composite Structures*, 190:137–159, 4 2018.

[17] A. H. Baluch, O. Falcó, J. L. Jiménez, B. H. A. H. Tijs, and C. S. Lopes. An efficient numerical approach to the prediction of laminate tolerance to Barely Visible Impact Damage. *Composite Structures*, 225, 2019.

[18] O. Falcó, C. S. Lopes, D. E. Sommer, D. Thomson, R. L. Ávila, and B. H. A. H. Tijs. Experimental analysis and simulation of low-velocity impact damage of composite laminates. *Composite Structures*, 287:115278, 5 2022.

[19] C. S Lopes, D. G. Gómez, O. Falcó, and B. H. A. H. Tijs. Stochastic virtual testing laboratory for unidirectional composite coupons: from conventional to dispersed-ply laminates. In *Multi-Scale Continuum Mechanics Modelling of Fibre-Reinforced Polymer Composites*, pages 579–607. Elsevier, 1 2021.

[20] B. H. A. H. Tijs, C. G. Dávila, A. Turon, and C. Bisagni. The importance of accounting for large deformation in continuum damage models in predicting matrix failure of composites. *Composites Part A: Applied Science and Manufacturing*, 164:107263, 1 2023.

[21] B. H. A. H. Tijs, S. Abdel-Monsef, J. Renart, A. Turon, and C. Bisagni. Characterization and analysis of the interlaminar behavior of thermoplastic composites considering fiber bridging and R-curve effects. *Composites Part A: Applied Science and Manufacturing*, 162:107101, 7 2022.

[22] M. R. Wisnom and F. Chang. Modelling of splitting and delamination in notched cross-ply laminates. *Composites Science and Technology*, 60(15):2849–2856, 11 2000.

[23] E. V. Iarve and D. H. Mollenhauer. Mesh-independent matrix cracking and delamination modeling in advanced composite materials. *Numerical Modelling of Failure in Advanced Composite Materials*, pages 227–264, 1 2015.

[24] M. Q. Le, H. Bainier, D. Néron, C. Ha-Minh, and P. Ladevèze. On matrix cracking and splits modeling in laminated composites. *Composites Part A: Applied Science and Manufacturing*, 115:294–301, 12 2018.

[25] T. R.C. Chuaqui, M. W.D. Nielsen, J. Colton, R. Butler, and A. T. Rhead. Effects of ply angle and blocking on open-hole tensile strength of composite laminates: A design and certification perspective. *Composites Part B: Engineering*, 207:108582, 2 2021.

[26] M. H. Nguyen and A. M. Waas. Modeling delamination migration in composite laminates using an enhanced semi-discrete damage model (eSD2M). *International Journal of Solids and Structures*, 236-237:111323, 2 2022.

[27] J. Huang, C. Zhang, J. Wang, and C. Zhang. On the applicability of rate-dependent cohesive zone models in low-velocity impact simulation. *Engineering Fracture Mechanics*, 271:108659, 8 2022.

[28] P. P. Camanho, M. A. Bessa, G. Catalanotti, M. Vogler, and R. Rolfes. Modeling the inelastic deformation and fracture of polymer composites-Part II: Smeared crack model. *Mechanics of Materials*, 59:36–49, 2013.

[29] F. P. Van der Meer, N. Moës, and L. J. Sluys. A level set model for delamination - Modeling crack growth without cohesive zone or stress singularity. *Engineering Fracture Mechanics*, 79:191–212, 1 2012.

[30] S. R. Hallett and P. W. Harper. Modelling delamination with cohesive interface elements. In *Numerical Modelling of Failure in Advanced Composite Materials*, pages 55–72. Elsevier Inc., 8 2015.

[31] B. Y. Chen, S. T. Pinho, N. V. De Carvalho, P. M. Baiz, and T. E. Tay. A floating node method for the modelling of discontinuities in composites. *Engineering Fracture Mechanics*, 127:104–134, 2014.

[32] P. Maimí, P. P. Camanho, J. A. Mayugo, and C. G. Dávila. A continuum damage model for composite laminates: Part II - Computational implementation and validation. *Mechanics of Materials*, 39(10):909–919, 10 2007.

[33] M. R. Wisnom, B. Khan, and S. R. Hallett. Size effects in unnotched tensile strength of unidirectional and quasi-isotropic carbon/epoxy composites. *Composite Structures*, 84(1):21–28, 6 2008.

[34] M. T. Kortschot and P. W. R. Beaumont. Damage mechanics of composite materials: I— Measurements of damage and strength. *Composites Science and Technology*, 39(4):289–301, 1 1990.

[35] E. V. Iarve, D. Mollenhauer, and R. Kim. Theoretical and experimental investigation of stress redistribution in open hole composite laminates due to damage accumulation. *Composites Part A: Applied Science and Manufacturing*, 36(2):163–171, 2 2005.

[36] D. Mollenhauer, E. V. Iarve, R. Kim, and B. Langley. Examination of ply cracking in composite laminates with open holes: A moiré interferometric and numerical study. *Composites Part A: Applied Science and Manufacturing*, 37(2):282–294, 2 2006.

[37] S. R. Hallett, B. G. Green, W. G. Jiang, and M. R. Wisnom. An experimental and numerical investigation into the damage mechanisms in notched composites. *Composites Part A: Applied Science and Manufacturing*, 40(5):613–624, 5 2009.

[38] Y. Nikishkov, A. Makeev, and G. Seon. Simulation of Damage in Composites Based on Solid Finite Elements. *Journal of the American Helicopter Society*, 55(4):042009, 2010.

[39] J. Llobet, P. Maimí, A. Turon, B. L.V. Bak, E. Lindgaard, L. Carreras, Y. Essa, and F. Martin de la Escalera. A continuum damage model for composite laminates: Part IV- Experimental and numerical tests. *Mechanics of Materials*, 154:103686, 3 2021.

[40] F. A. Leone. Deformation gradient tensor decomposition for representing matrix cracks in fiber-reinforced materials. *Composites Part A: Applied Science and Manufacturing*, 76:334–341, 7 2015.

[41] H. Fallahi, F. Taheri-Behrooz, and A. Asadi. Nonlinear Mechanical Response of Polymer Matrix Composites: A Review. *Polymer Reviews*, 60(1):42–85, 1 2020.

[42] M.C. Lafarie-Frenot and F. Touchard. Comparative in-plane shear behaviour of long-carbon-fibre composites with thermoset or thermoplastic matrix. *Composites Science and Technology*, 52(3):417–425, 1 1994.

[43] L. A. Carlsson, J. W. Gillespie, and B. R. Trethewey. Mode II Interlaminar Fracture of Graphite/Epoxy and Graphite/PEEK:. *Journal of Reinforced Plastics and Composites*, 5(3):170–187, 8 1986.

[44] F. A. Leone, A. C. Bergan, and C. G. Dávila. CompDam - Deformation Gradient Decomposition (DGD), 2019.

[45] SIMULIA Dassault Systemes. ABAQUS User's Manual, version 2019, 2019.

[46] G. Catalanotti, P. P. Camanho, and A. T. Marques. Three-dimensional failure criteria for fiber-reinforced laminates. *Composite Structures*, 95:63–79, 1 2013.

[47] P. Maimí, P. P. Camanho, J. A. Mayugo, and C. G. Dávila. A continuum damage model for composite laminates: Part I - Constitutive model. *Mechanics of Materials*, 39(10):897–908, 10 2007.

[48] C. G Dávila, C. A Rose, and P. P Camanho. A procedure for superposing linear cohesive laws to represent multiple damage mechanisms in the fracture of composites. *International Journal of Fracture 2009 158:2*, 158(2):211–223, 6 2009.

[49] A. Puck and H. Schürmann. Failure analysis of FRP laminates by means of physically based phenomenological models. *Composites Science and Technology*, 58(7):1045–1067, 7 1998.

[50] A. Puck, J. Kopp, and M. Knops. Guidelines for the determination of the parameters in Puck's action plane strength criterion. *Composites Science and Technology*, 62(3):371–378, 2002.

[51] M. Knops. *Analysis of failure in fiber polymer laminates: The theory of Alfred Puck*. Springer Berlin Heidelberg, 2008.

[52] VDI-2014 Blatt 3: Entwicklung von Bauteilen aus Faser-Kunststoff-Verbund - Berechnungen, 2006.

[53] Z. P. Bažant and B. H. Oh. Crack band theory for fracture of concrete. *Matériaux et Constructions*, 16(3):155–177, 5 1983.

[54] W. Tan, B. G. Falzon, and M. Price. Predicting the crushing behaviour of composite material using high-fidelity finite element modelling. *International Journal of Crashworthiness*, 20(1):60–77, 1 2015.

[55] R. C. Batra. *Elements of Continuum Mechanics*. American Institute of Aeronautics and Astronautics, Reston ,VA, 1 2006.

[56] G. A. Holzapfel. *Nonlinear Solid Mechanics: A Continuum Approach for Engineering*. John Wiley & Sons Lt., West Sussex, England, 2000.

[57] M. L. Benzeggagh and M. Kenane. Measurement of mixed-mode delamination fracture toughness of unidirectional glass/epoxy composites with mixed-mode bending apparatus. *Composites Science and Technology*, 56(4):439–449, 1 1996.

[58] A. Turon, P. P. Camanho, J. Costa, and J. Renart. Accurate simulation of delamination growth under mixed-mode loading using cohesive elements: Definition of interlaminar strengths and elastic stiffness. *Composite Structures*, 92(8):1857–1864, 7 2010.

[59] M. R. Wisnom. The role of delamination in failure of fibre-reinforced composites. *Philosophical Transactions of the Royal Society A: Mathematical, Physical and Engineering Sciences*, 370(1965):1850–1870, 4 2012.

[60] P. P. Camanho, P. Maimí, and C. G. Dávila. Prediction of size effects in notched laminates using continuum damage mechanics. *Composites Science and Technology*, 67(13):2715–2727, 10 2007.

[61] Solvay. Technical data sheet: APC (PEKK-FC) PEKK-FC thermoplastic polymer prepreg, 2017.

[62] D. R. Moore. Toughness characterization of carbon fibre/polyether ether ketone (CF/PEEK) laminates. *Pure and Applied Chemistry*, 63(11):1609–1625, 1 1991.

[63] H. Wang and T. Vu-Khanh. Use of end-loaded-split (ELS) test to study stable fracture behaviour of composites under mode II loading. *Composite Structures*, 36(1-2):71–79, 9 1996.

[64] A. Turon, P. P. Camanho, J. Costa, and C. G. Dávila. A damage model for the simulation of delamination in advanced composites under variable-mode loading. *Mechanics of Materials*, 38(11):1072–1089, 11 2006.

[65] J. R. Reeder and J. H. Crews. Mixed-mode bending method for delamination testing. *AIAA Journal*, 28(7):1270–1276, 5 2012.

[66] F. Sacchetti, W. J.B. Grouve, L. L. Warnet, and I. F. Villegas. Effect of resin-rich bond line thickness and fibre migration on the toughness of unidirectional carbon/PEEK joints. *Composites Part A: Applied Science and Manufacturing*, 109:197–206, 6 2018.

[67] M. Hojjati, J. Chen, A. Yousefpour, and J. Pratte. Crystallization kinetics of cypek™ poly ether ketone ketone. *International SAMPE Symposium and Exhibition (Proceedings)*, 52, 10 2008.

[68] K. C. H. Gardner, B. S. Hsiao, R. R. Matheson, and B. A. Wood. Structure, crystallization and morphology of poly (aryl ether ketone ketone). *Polymer*, 33(12):2483–2495, 1 1992.

[69] W. Tan, B. G. Falzon, and M. Price. Predicting the crushing behaviour of composite material using high-fidelity finite element modelling. *International Journal of Crashworthiness*, 20(1):60–77, 1 2015.

[70] W. J. Vankan, B. H. A. H. Tijs, G. J. De Jong, H. C. De Frel, and N. K. Singh. Strength of notched and un-notched thermoplastic composite laminate in biaxial tension and compression. *Journal of Composite Materials*, 50(25), 2016.

[71] I. Baran, L. L. Warnet, and R. Akkerman. Assessment of failure and cohesive zone length in co-consolidated hybrid C/PEKK butt joint. *Engineering Structures*, 168:420–430, 8 2018.

[72] V. Tvergaard and J. W. Hutchinson. The relation between crack growth resistance and fracture process parameters in elastic-plastic solids. *Journal of the Mechanics and Physics of Solids*, 40(6):1377–1397, 8 1992.

[73] B. F. Sørensen and T. K. Jacobsen. Large-scale bridging in composites: R-curves and bridging laws. *Composites Part A: Applied Science and Manufacturing*, 29(11):1443–1451, 11 1998.

[74] C. Sarrado, A. Turon, J. Costa, and J. Renart. An experimental analysis of the fracture behavior of composite bonded joints in terms of cohesive laws. *Composites Part A: Applied Science and Manufacturing*, 90:234–242, 11 2016.

[75] M. F. S. F. de Moura and A. B. de Morais. Equivalent crack based analyses of ENF and ELS tests. *Engineering Fracture Mechanics*, 75(9):2584–2596, 6 2008.

[76] A. Turon, E. V. González, C. Sarrado, G. Guillamet, and P. Maimí. Accurate simulation of delamination under mixed-mode loading using a cohesive model with a mode-dependent penalty stiffness. *Composite Structures*, 184:506–511, 1 2018.

[77] R. D. S. G. Campilho, M. D. Banea, J. A. B. P. Neto, and L. F. M. Da Silva. Modelling adhesive joints with cohesive zone models: effect of the cohesive law shape of the adhesive layer. *International Journal of Adhesion and Adhesives*, 44:48–56, 7 2013.

[78] S. M. Jensen, M. J. Martos, B. L.V. Bak, and E. Lindgaard. Formulation of a mixed-mode multilinear cohesive zone law in an interface finite element for modelling delamination with R-curve effects. *Composite Structures*, 216:477–486, 5 2019.

[79] V. Tamuzs, S. Tarasovs, and U. Vilks. Progressive delamination and fiber bridging modeling in double cantilever beam composite specimens. *Engineering Fracture Mechanics*, 68(5):513–525, 3 2001.

[80] S. Yin, Y. Gong, W. Li, L. Zhao, J. Zhang, and N. Hu. A novel four-linear cohesive law for the delamination simulation in composite DCB laminates. *Composites Part B: Engineering*, 180:107526, 1 2020.

[81] A. Raimondo, I. Urcelay Oca, and C. Bisagni. Influence of interface ply orientation on delamination growth in composite laminates:. *Journal of Composite Materials*, 55(27):3955–3972, 7 2021.

[82] B. F. Sørensen and T. K. Jacobsen. Characterizing delamination of fibre composites by mixed mode cohesive laws. *Composites Science and Technology*, 69(3-4):445–456, 3 2009.

[83] ASTM D5528-13, Standard Test Method for Mode I Interlaminar Fracture Toughness of Unidirectional Fiber-Reinforced Polymer Matrix Composites, ASTM International, West Conshohocken, PA, 2013.

[84] ASTM D7905 / D7905M-19e1, Standard Test Method for Determination of the Mode II Interlaminar Fracture Toughness of Unidirectional Fiber-Reinforced Polymer Matrix Composites, ASTM International, West Conshohocken, PA, 2019.

[85] ISO 15114:2014 Fibre-reinforced plastic composites — Determination of the mode II fracture resistance for unidirectionally reinforced materials using the calibrated end-loaded split (C-ELS) test and an effective crack length approach, 2014.

[86] ASTM D6671 / D6671M-19, Standard Test Method for Mixed Mode I-Mode II Interlaminar Fracture Toughness of Unidirectional Fiber Reinforced Polymer Matrix Composites, ASTM International, West Conshohocken, PA, 2019.

[87] S. Abdel Monsef, A. Ortega, A. Turon, P. Maimí, and J. Renart. An efficient method to extract a mode I cohesive law for bonded joints using the double cantilever beam test. *Composites Part B: Engineering*, 178:107424, 12 2019.

[88] S. Abdel Monsef, M. Pérez-Galmés, J. Renart, A. Turon, and P. Maimí. The influence of mode II test configuration on the cohesive law of bonded joints. *Composite Structures*, 234:111689, 2 2020.

[89] ISO 15024:2001 Fibre-reinforced plastic composites — Determination of mode I interlaminar fracture toughness, GIC, for unidirectionally reinforced materials, 2001.

[90] J. Renart, N. Blanco, E. Pajares, J. Costa, S. Lazcano, and G. Santacruz. Side Clamped Beam (SCB) hinge system for delamination tests in beam-type composite specimens. *Composites Science and Technology*, 71(8), 5 2011.

[91] S. Hashemi, A. J. Kinloch, and J. G. Williams. The analysis of interlaminar fracture in uniaxial fibre-polymer composites. *Proceedings of the Royal Society of London. A. Mathematical and Physical Sciences*, 427(1872):173–199, 1 1990.

[92] J. D. Barrett and R. O. Foschi. Mode II stress-intensity factors for cracked wood beams. *Engineering Fracture Mechanics*, 9(2):371–378, 1 1977.

[93] Y. Wang and J. G. Williams. Corrections for mode II fracture toughness specimens of composites materials. *Composites Science and Technology*, 43(3):251–256, 1 1992.

[94] V. Tvergaard and J. W. Hutchinson. The influence of plasticity on mixed mode interface toughness. *Journal of the Mechanics and Physics of Solids*, 41(6):1119–1135, 1993.

[95] A. Ortega, P. Maimí, E. V. González, and D. Trias. Characterization of the translaminar fracture Cohesive Law. *Composites Part A: Applied Science and Manufacturing*, 91:501–509, 12 2016.

[96] S. Abdel-Monsef, J. Renart, L. Carreras, P. Maimí, and A. Turon. Environmental effects on the cohesive laws of the composite bonded joints. *Composites Part A: Applied Science and Manufacturing*, 155:106798, 4 2022.

[97] C. Bouvet, J. Serra, and P. Garcia Perez. Strain rate effect of mode II interlaminar fracture toughness on the impact response of a thermoplastic PEEK composite. *Composites Part C: Open Access*, 2:100031, 10 2020.

[98] H. Pérez-Martín, P. Mackenzie, A. Baidak, C. M. Ó Brádaigh, and D. Ray. Crystallinity studies of PEKK and carbon fibre/PEKK composites: A review. *Composites Part B: Engineering*, 223:109127, 10 2021.

[99] A. Turon, C. G. Dávila, P. P. Camanho, and J. Costa. An engineering solution for mesh size effects in the simulation of delamination using cohesive zone models. *Engineering Fracture Mechanics*, 74(10):1665–1682, 7 2007.

[100] W. Van Paepegem, I. De Baere, and J. Degrieck. Modelling the nonlinear shear stress–strain response of glass fibre-reinforced composites. Part I: Experimental results. *Composites Science and Technology*, 66(10):1455–1464, 8 2006.

[101] M. S. Kafkalidis and M. D. Thouless. The effects of geometry and material properties on the fracture of single lap-shear joints. *International Journal of Solids and Structures*, 39(17):4367–4383, 8 2002.

[102] C. Sarrado, F. A. Leone, and A. Turon. Finite-thickness cohesive elements for modeling thick adhesives. *Engineering Fracture Mechanics*, 168:105–113, 12 2016.

[103] R. D. S. G. Campilho, M. D. Banea, A. M.G. Pinto, L. F. M. Da Silva, and A. M. P. De Jesus. Strength prediction of single- and double-lap joints by standard and extended finite element modelling. *International Journal of Adhesion and Adhesives*, 31(5):363–372, 7 2011.

[104] T. Zhao, G. Palardy, I. F. Villegas, C. Rans, M. Martinez, and R. Benedictus. Mechanical behaviour of thermoplastic composites spot-welded and mechanically fastened joints: A preliminary comparison. *Composites Part B: Engineering*, 112:224–234, 3 2017.

[105] J. Kupski, S. Teixeira de Freitas, D. Zarouchas, P. P. Camanho, and R. Benedictus. Composite layup effect on the failure mechanism of single lap bonded joints. *Composite Structures*, 217:14–26, 6 2019.

[106] A. P. K. Joseph, P. Davidson, and A. M. Waas. Progressive damage and failure analysis of single lap shear and double lap shear bolted joints. *Composites Part A: Applied Science and Manufacturing*, 113:264–274, 10 2018.

[107] O. Ishida, J. Kitada, K. Nunotani, and K. Uzawa. Impregnation and resin flow analysis during compression process for thermoplastic composite production. *https://doi.org/10.1080/09243046.2020.1752964*, 2020.

[108] F. Sacchetti, W. J. B. Grouve, L. L. Warnet, and I. F. Villegas. Effect of cooling rate on the interlaminar fracture toughness of unidirectional carbon/PPS laminates. *Engineering Fracture Mechanics*, 203:126–136, 11 2018.

[109] W. J. B. Grouve, F. Sacchetti, E. J. Vruggink, and R. Akkerman. Simulating the induction heating of cross-ply C/PEKK laminates – sensitivity and effect of material variability. *https://doi.org/10.1080/09243046.2020.1783078*, pages 1–22, 2020.

[110] ASTM D3165-07(2014), Standard Test Method for Strength Properties of Adhesives in Shear by Tension Loading of Single-Lap-Joint Laminated Assemblies, ASTM International, West Conshohocken, PA, 2014.

[111] B. H. A. H. Tijs, A. Turon, and C. Bisagni. The importance of accounting for large shear deformation on modelling matrix failure of thermoplastic and thermoset composites. In *Proceedings of the 7th ECCOMAS Thematic Conference on the Mechanical Response of Composites: COMPOSITES 2019, Girona, Spain, 18-20 Sept.*, pages 94–94, 2019.

[112] N. Laws and G. J. Dvorak. Progressive transverse cracking In composite laminates. *Journal of Composite Materials*, 22(10):900–916, 10 1988.

[113] K. S. Van Dooren, E. Labans, B. H. A. H. Tijs, C. Bisagni, and J. Waleson. Analysis and testing of a thermoplastic composite stiffened panel under compression. In *Proceedings of 22nd International Conference on Composite Materials (ICCM22), Melbourne, AU, August 11-16*. APA, 2019.

[114] Clean Sky 2 and Clean Aviation. *Multi Functional Fuselage Demonstrator*. URL: https://clean-aviation.eu/clean-sky-2/key-demonstrators/multi-functional-fuselage-demonstrator [date accessed: 07/10/2022].

[115] K. S. van Dooren and C. Bisagni. Design and analysis of thermoplastic welded stiffened panels in post-buckling. In *ASC 36TH Annual Technical VIRTUAL Conference: Composites Ingenuity Taking on Challenges in Environment-Energy-Economy*, pages 406–417, 2021.

[116] S. L. Omairey, S. Sampethai, L. Hans, C. Worrall, S. Lewis, D. Negro, T. Sattar, E. Ferrera, E. Blanco, J. Wighton, L. Muijs, S. L. Veldman, M. Doldersum, R. Tonnaer, N. Jayasree, and M. Kazilas. Development of innovative automated solutions for the assembly of multifunctional thermoplastic composite fuselage. *International Journal of Advanced Manufacturing Technology*, 117(5-6):1721–1738, 11 2021.

[117] A. C. Orifici, R. S. Thomson, I. Herszberg, T. Weller, R. Degenhardt, and J. Bayandor. An analysis methodology for failure in postbuckling skin–stiffener interfaces. *Composite Structures*, 86(1-3):186–193, 11 2008.

[118] C. Bisagni and C. G. Dávila. Experimental investigation of the postbuckling response and collapse of a single-stringer specimen. *Composite Structures*, 108(1):493–503, 2 2014.

[119] L. Kootte and C. Bisagni. A Methodology to Investigate Skin-Stringer Separation in Postbuckled Composite Stiffened Panels. In *AIAA Scitech 2020 Forum*, pages 1–14, Reston, Virginia, 1 2020. American Institute of Aeronautics and Astronautics.

[120] K. S. van Dooren, B. H. A. H. Tijs, J. E. A. Waleson, and C. Bisagni. Skin-stringer separation in post-buckling of butt-joint stiffened thermoplastic composite panels. *Composite Structures*, 304:116294, 1 2023.

[121] I. F. Villegas and C. Rans. The dangers of single-lap shear testing in understanding polymer composite welded joints. *Philosophical Transactions of the Royal Society A: Mathematical, Physical and Engineering Sciences*, 379(2203):20200296, 8 2021.

[122] K. Goto, K. Imai, M. Arai, and T. Ishikawa. Shear and tensile joint strengths of carbon fiber-reinforced thermoplastics using ultrasonic welding. *Composites Part A: Applied Science and Manufacturing*, 116:126–137, 1 2019.

[123] ASTM D1002-10(2019), Standard Test Method for Apparent Shear Strength of Single-Lap-Joint Adhesively Bonded Metal Specimens by Tension Loading (Metal-to-Metal), ASTM International, West Conshohocken, PA, 2019.

[124] ASTM D5868-01(2014), Standard Test Method for Lap Shear Adhesion for Fiber Reinforced Plastic (FRP) Bonding, ASTM International, West Conshohocken, PA, 2016.

[125] J. F. Reis, A. B. M. Abrahao, M. L. Costa, and E. C. Botelho. Assessment of the interlaminar strength of resistance-welded PEI/carbon fibre composite. *Welding International*, 32(2):149–160, 2 2018.

[126] M. Dubé, P. Hubert, A. Yousefpour, and J. Denault. Resistance welding of thermoplastic composites skin/stringer joints. *Composites Part A: Applied Science and Manufacturing*, 38(12):2541–2552, 12 2007.

[127] T. R. Guess, R. E. Allred, and F. P. Gerstle Jr. Comparison of lap shear test specimens. *ASTM Journal of Testing and Evaluation*, 5(2), 3 1977.

[128] L. F. M. da Silva, T. N. S. S. Rodrigues, M. A. V. Figueiredo, M. F. S. F. de Moura, and J. A. G. Chousal. Effect of Adhesive Type and Thickness on the Lap Shear Strength. *The Journal of Adhesion*, 82(11):1091–1115, 11 2006.

[129] B. Harras, K. C. Cole, and T. Vu-Khanh. Optimization of the Ultrasonic Welding of PEEK-Carbon Composites. *Journal of Reinforced Plastics and Composites*, 15(2):174–182, 2 1996.

[130] Min-Chung Li and Alfred C. Loos. The effects of processing on interply bond strength of thermoplastic composites. *Journal of Reinforced Plastics and Composites*, 11(10):1142–1162, 10 1992.

[131] R. Krueger. Virtual crack closure technique: History, approach, and applications. *Applied Mechanics Reviews*, 57(2):109–143, 3 2004.

[132] ASTM D7264 / D7264M-21, Standard Test Method for Flexural Properties of Polymer Matrix Composite Materials, ASTM International, West Conshohocken, PA, 2021.

[133] T. Thäsler, J. Holtmannspötter, and H.-J. Gudladt. Monitoring the fatigue crack growth behavior of composite joints using in situ 2D-digital image correlation. *The Journal of Adhesion*, 95(5-7):595–613, 6 2019.

[134] I. Leciñana, J. Renart, A. Turon, J. Zurbitu, and B. H. A. H. Tijs. Characterization and analysis of the mode I interlaminar fatigue behaviour of thermoplastic composites considering R-curve effects. *Engineering Fracture Mechanics*, page 109273, 4 2023.

[135] S. Abdel-Monsef, B.H.A.H. Tijs, J. Renart, and A. Turon. Accurate simulation of delamination under mixed-mode loading using a multilinear cohesive law. *Engineering Fracture Mechanics*, 284:109233, 5 2023.

[136] B. H. A. H. Tijs, A. Turon, and C. Bisagni. Failure of Thermoplastic Composite Welded Joints. In *Proceedings of the 8th ECCOMAS Thematic Conference on the Mechanical Response of Composites: COMPOSITES 2021*, 9 2021.

[137] O. Falcó, B. Tijs, B. Romano, and C. S. Lopes. A virtual test lab for unidirectional composite coupons. In *Proceedings of the 18th European Conference on Composite Materials*, Athens, Greece, 6 2018.

List of Publications

Journal publications

1. B. H. A. H. Tijs, A. Turon, and C. Bisagni. Characterization and analysis of conduction welded thermoplastic composite joints considering the influence of manufacturing. *Manuscript prepared for submission to Elsevier*, 2023

2. I. Leciñana, J. Renart, A. Turon, J. Zurbitu, and B. H. A. H. Tijs. Characterization and analysis of the mode I interlaminar fatigue behaviour of thermoplastic composites considering R-curve effects. *Engineering Fracture Mechanics*, page 109273, 4 2023

3. S. Abdel-Monsef, B.H.A.H. Tijs, J. Renart, and A. Turon. Accurate simulation of delamination under mixed-mode loading using a multilinear cohesive law. *Engineering Fracture Mechanics*, 284:109233, 5 2023

4. B. H. A. H. Tijs, C. G. Dávila, A. Turon, and C. Bisagni. The importance of accounting for large deformation in continuum damage models in predicting matrix failure of composites. *Composites Part A: Applied Science and Manufacturing*, 164:107263, 1 2023

5. K. S. van Dooren, B. H. A. H. Tijs, J. E. A. Waleson, and C. Bisagni. Skin-stringer separation in post-buckling of butt-joint stiffened thermoplastic composite panels. *Composite Structures*, 304:116294, 1 2023

6. B. H. A. H. Tijs, S. Abdel-Monsef, J. Renart, A. Turon, and C. Bisagni. Characterization and analysis of the interlaminar behavior of thermoplastic composites considering fiber bridging and R-curve effects. *Composites Part A: Applied Science and Manufacturing*, 162:107101, 7 2022

7. O. Falcó, C. S. Lopes, D. E. Sommer, D. Thomson, R. L. Ávila, and B. H. A. H. Tijs. Experimental analysis and simulation of low-velocity impact damage of composite laminates. *Composite Structures*, 287:115278, 5 2022

8. B. H. A. H. Tijs, M. H. J. Doldersum, A. Turon, J. E. A. Waleson, and C. Bisagni. Experimental and numerical evaluation of conduction welded thermoplastic composite joints. *Composite Structures*, 281:114964, 2 2022

9. A. H. Baluch, O. Falcó, J. L. Jiménez, B. H. A. H. Tijs, and C. S. Lopes. An efficient numerical approach to the prediction of laminate tolerance to Barely Visible Impact Damage. *Composite Structures*, 225, 2019

10. O. Falcó, R. L. Ávila, B. Tijs, and C. S. Lopes. Modelling and simulation methodology for unidirectional composite laminates in a Virtual Test Lab framework. *Composite Structures*, 190:137–159, 4 2018
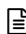
Book chapter

1. C. S Lopes, D. G. Gómez, O. Falcó, and B. H. A. H. Tijs. Stochastic virtual testing laboratory for unidirectional composite coupons: from conventional to dispersed-ply laminates. In *Multi-Scale Continuum Mechanics Modelling of Fibre-Reinforced Polymer Composites*, pages 579–607. Elsevier, 1 2021

Conference proceedings

1. B. H. A. H. Tijs, A. Turon, and C. Bisagni. Failure of Thermoplastic Composite Welded Joints. In *Proceedings of the 8th ECCOMAS Thematic Conference on the Mechanical Response of Composites: COMPOSITES 2021*, 9 2021

2. J. Renart, B. H. A. H. Tijs, A. Turon. Characterization of delamination onset and propagation under fatigue loading of AS4D/PEKK-FC thermoplastic composites. 10th International Conference on Composites Testing and Model Identification (CompTest 2021), online, May 2021.

3. B. H. A. H. Tijs, K. S. van Dooren, and C. Bisagni. Development of a numerical framework for virtual testing to support design of a next generation thermoplastic multifunctional fuselage. In *European Conference On Multifunctional Structures (EMuS2020)*, pages 90–95, 2020

4. B. H. A. H. Tijs, A. Turon, and C. Bisagni. The importance of accounting for large shear deformation on modelling matrix failure of thermoplastic and thermoset composites. In *Proceedings of the 7th ECCOMAS Thematic Conference on the Mechanical Response of Composites: COMPOSITES 2019, Girona, Spain, 18-20 Sept.*, pages 94–94, 2019

5. K. S. Van Dooren, E. Labans, B. H. A. H. Tijs, C. Bisagni, and J. Waleson. Analysis and testing of a thermoplastic composite stiffened panel under compression. In *Proceedings of 22nd International Conference on Composite Materials (ICCM22), Melbourne, AU, August 11-16*. APA, 2019

6. O. Falcó, B. Tijs, B. Romano, and C. S. Lopes. A virtual test lab for unidirectional composite coupons. In *Proceedings of the 18th European Conference on Composite Materials*, Athens, Greece, 6 2018

7. C. S. Lopes, O. Falcó, B. Tijs, S. Sádaba, M. Herráez, C. González. Advanced virtual characterization of UD composite laminates. Society of Engineering Science (SES 2018), 55th Annual Technical Meeting, Madrid, Spain, October 2018.

8. A. H. Baluch, O. Falcó, C. S. Lopes, B. Tijs. Development of efficient approaches to simulate Compression After Impact strength of composite laminates", 4th International Conference on Mechanics of Composites (MECHCOPMP 2018), Madrid, Spain, July 2018.

9. B. H. A. H. Tijs, C. S. Lopes, A. Turon, C. Bisagni, J. Waleson, J. W. Van Ingen, and S. L. Veldman. Virtual testing of thermoplastic composites: Towards a hybrid simulation-physical testing pyramid. In *Proceedings of the 18th European Conference on Composite Materials*, Athens, Greece, 6 2018

Special sessions

1. Keynote speaker in session in memory of Cláudio Lopes: B. H. A. H. Tijs, A. Turon, and C. Bisagni. Failure of Thermoplastic Composite Welded Joints. In *Proceedings of the 8th ECCOMAS Thematic Conference on the Mechanical Response of Composites: COMPOSITES 2021*, 9 2021

2. Invited speaker: NASA Polymer Matrix Composite Community of Practice. A. Offringa and B. H. A. H. Tijs. Thermoplastic composites in aerospace, technologies, applications and current developments. online, 2021

3. Invited speaker: Industrial workshop on new trends in composite materials. B. H. A. H. Tijs. Thermoplastic composites for primary aircraft structures. University of Girona, Girona, Spain, Sept. 17 (2019).

4. Invited speaker: ICONIC Summer School - Virtual testing and design of composite structures. B. H. A. H. Tijs. Virtual Testing of Composites: Adding value in the Aerospace industry. Queen's University Belfast, Belfast, UK. Aug. 27-29 (2018).

🗎 Included in this thesis.

Acknowledgments

Just as in building houses, there are different kinds of foundations. My foundation, as detailed in the biographical note, is somewhat non-standard. For me, this foundation has allowed me to perform this PhD research project in an ideal situation, by combining technology development for the company while at the same time advancing scientific knowledge on thermoplastic composites and analysis methods. This dissertation is the result of this experience and would not exist without the support of countless people. Thus, I would like to take this opportunity to thank everyone who contributed to make this happen. First and foremost, I express my gratitude to my promotors prof. dr. Chiara Bisagni and dr. Albert Turon, but also Rienk Timmerman and Peter Kortbeek from Fokker/GKN Aerospace for supporting me at the start of the PhD project. Furthermore, I thank Claudio Lopes and Wouter Wilson, who sparked my interest in research. My deepest gratitude goes to my promotors, between many other things, for their guidance and mentorship, allowing for independence in my research, and to transform this engineer into an independent researcher and specialist in the field of composite analysis. Thank you for mentoring me throughout the entire PhD program, but also on the process of writing and critically reflecting on my research. I consider this one of the most important parts of my personal development. This research work is co-funded by the STUNNING project and Fokker/GKN Aerospace. I gratefully acknowledge their support, especially the welding team in Hoogeveen, Marco, Salvador, JaapWillem, Luuk and Dennis, who supported me during manufacturing. I wish to convey my thanks to many colleagues, in particular our Analysis Specialist group at Fokker/GKN Aerospace who were part of the journey during our monday-morning team sessions. I also acknowledge the support of the technicians/researchers at both TU Delft and University of Girona. Special thanks to my PhD office mates, Kevin, Luc, Jens, Arne, Andrés, and sometimes special guest Niels for the great environment. I also really enjoyed the lunches with the professors at TU Delft. Particularly the discussions with Saullo and the advise of Sergio on both my PhD and home-automation were highly appreciated. Furthermore, I am grateful for the keen involvement of my co-authors Carlos Dávila, Jordi Renart, Said Abdel-Monsef and Jan Waleson. I really enjoyed our interesting technical discussions. Besides doing the PhD, my other hobby project, namely the design and construction of our new house also took place. I would like to acknowledge Allurebouw for dealing with me during the design process and for constructing the new house, which has now become the home of my familiy. I am also grateful for joining the welcoming community in Vroondaal, the Hague. Finally, I want to thank my parents, Hennie and Cyntha, my brother Frank and my other family and friends. Special thanks to my wife Nadia for her affection and for being a very caring mother of our boys. Tobias and Rovan, you are the sunshine of my life and always will be.

Bas H.A.H. Tijs
Delft, December 2022

Biographical note

Bas Henricus Antonius Hermanus Tɪᴊs

Date of birth: 17-08-1983
Nationality: Dutch
Email: bastijs@bastijs.nl
bas.tijs@fokker.com
Linkedin: `https://www.linkedin.com/in/`
`bas-tijs-57467812/`
Google scholar: `https://scholar.google.com/`
`citations?user=smtxYSkAAAAJ&hl=en`
OrcID: 0000-0002-5506-1180

Bas Tijs was born on the 17th of August 1983 in Zwolle, the Netherlands and was raised in Luttenberg, Overijssel. He followed a somewhat non-standard track towards obtaining his PhD degree. After secondary school, he decided to study aeronautical engineering at bachelor of engineering level (BEng) in Haarlem. As he was still rather young and also wanted some practical experience, he first started a study a bit closer to home at Deltion College Zwolle 'luchtvaarttechniek' to train as aircraft mechanic. At this college he practiced on the Northrop F-5 Freedom Fighter, which was the predecessor of the F-16 fighter jet for the Dutch Airforce. During his first internship in 2001 he worked at the (now former) Airforce base in Enschede, the Netherlands. He was part of a 'dock' that performed the D-check of the F-16 jet, which is the largest and most comprehensive inspections and repairs of the entire aircraft. During the internship he also worked on modernizing the Pratt & Whitney F100 engine by digital-electronic control in the engines dock. At this place he witnessed the news of the sad 9/11 happenings, which made a big impact to the operations on the airbase and aeronautical industry. During his second internship he worked the KLM OMRA department at 'Hangaar 14' in Schiphol on the maintenance of Boeing 737/747 parts. Shortly after this, he moved to the west of the Netherlands to continue his study on aeronautical engineering at INHOLLAND Delft. Both his internship and graduation were performed at Urenco Aerospace (now Aeronamic) at Almelo, the Netherlands. Although his internship was on researching the upcoming all-electric aircraft and specifications on generator design, Bas found more interest in supporting a study on vibration issues on an auxiliary-power-unit (APU) compressor turbine, where he made his first experience on using finite-element software to improve the eigenfrequencies of the turbine during operation. His graduation, also at Urenco, was to investigate fatigue cracks

in the APU compressor casing where he got his first experience in studying material failure behavior and using microscopy. During his studies he met Nadia Haider in Enschede, who decided to pursue a master and PhD degree in electrical engineering (Radar Technology) at the Delft University of Technology, so Bas searched for a job near Delft. Bas joined Fokker Aerostructures BV (now part of GKN Aerospace) in Papendrecht in August 2007 as part of a 'master traineeship', which was designed to get BEng students up to speed as stress-engineers. He started his career on the fatigue & damage tolerance certification and full-scale testing of the NH90 helicopter. During his career he developed a strong interest in the development of Tools & Methods and joined the Stress Methodology group in 2012 where he has supported the development of several projects such as the Gulfstream G650, Dassault F5x and Airbus A350. During this career he kept improving his knowledge through courses and supervision of both bachelor and master level students. In 2014 he was the first industrial student to receive a certificate of the new TU Delft online master courses. Since 2015 he is leading the development of advanced simulation techniques such as Virtual Testing in collaboration with academia (TU Delft, TU/e, UTwente, University of Girona) and research institutes (IMDEA Materials, NLR). These collaborations sparked his interest in performing his own research in the field of Virtual Testing. In 2017 he was involved in defining part of the technology development of the STUNNING project where he proposed several PhD topics to further develop the Virtual Testing capabilities and got the opportunity to perform his own (part-time) PhD research program as part of this collaboration with Delft University of Technology in 2018. He was admitted to the PhD program without a master-degree. While his PhD ends as planned in 2023, he is still eager to continue the collaboration between industry and academia and take part in research himself.